

NASA/TM-2002-211857  
AFDD/TR-02-A-009



# **A Study of Dynamic Stall Vortex Development Using Two-Dimensional Data from the AFDD Oscillating Wing Experiment**

*Myung J. Rhee*

**DISTRIBUTION STATEMENT A**  
Approved for Public Release  
Distribution Unlimited

20030529 145

---

December 2002

## The NASA STI Program Office . . . in Profile

Since its founding, NASA has been dedicated to the advancement of aeronautics and space science. The NASA Scientific and Technical Information (STI) Program Office plays a key part in helping NASA maintain this important role.

The NASA STI Program Office is operated by Langley Research Center, the Lead Center for NASA's scientific and technical information. The NASA STI Program Office provides access to the NASA STI Database, the largest collection of aeronautical and space science STI in the world. The Program Office is also NASA's institutional mechanism for disseminating the results of its research and development activities. These results are published by NASA in the NASA STI Report Series, which includes the following report types:

- **TECHNICAL PUBLICATION.** Reports of completed research or a major significant phase of research that present the results of NASA programs and include extensive data or theoretical analysis. Includes compilations of significant scientific and technical data and information deemed to be of continuing reference value. NASA's counterpart of peer-reviewed formal professional papers but has less stringent limitations on manuscript length and extent of graphic presentations.
- **TECHNICAL MEMORANDUM.** Scientific and technical findings that are preliminary or of specialized interest, e.g., quick release reports, working papers, and bibliographies that contain minimal annotation. Does not contain extensive analysis.
- **CONTRACTOR REPORT.** Scientific and technical findings by NASA-sponsored contractors and grantees.

- **CONFERENCE PUBLICATION.** Collected papers from scientific and technical conferences, symposia, seminars, or other meetings sponsored or cosponsored by NASA.
- **SPECIAL PUBLICATION.** Scientific, technical, or historical information from NASA programs, projects, and missions, often concerned with subjects having substantial public interest.
- **TECHNICAL TRANSLATION.** English-language translations of foreign scientific and technical material pertinent to NASA's mission.

Specialized services that complement the STI Program Office's diverse offerings include creating custom thesauri, building customized databases, organizing and publishing research results . . . even providing videos.

For more information about the NASA STI Program Office, see the following:

- Access the NASA STI Program Home Page at <http://www.sti.nasa.gov>
- E-mail your question via the Internet to [help@sti.nasa.gov](mailto:help@sti.nasa.gov)
- Fax your question to the NASA Access Help Desk at (301) 621-0134
- Telephone the NASA Access Help Desk at (301) 621-0390
- Write to:  
NASA Access Help Desk  
NASA Center for AeroSpace Information  
7121 Standard Drive  
Hanover, MD 21076-1320



## **A Study of Dynamic Stall Vortex Development Using Two-Dimensional Data from the AFDD Oscillating Wing Experiment**

*Myung J. Rhee*  
*Aeroflightdynamics Directorate*  
*U.S. Army Aviation and Missile Command*  
*Ames Research Center, Moffett Field, California*

National Aeronautics and  
Space Administration

Ames Research Center  
Moffett Field, California 94035-1000

## **Acknowledgments**

The author would like to express sincere thanks and regards to Dr. Larry Carr for his guidance and technical advice. The author also would like to express special thanks to Mrs. Laura Galvas in the Automation Team at AFDD for her continuous assistance in preparing various plots for the experimental data, and to Ms. Shelley Scarich for her effort to edit the manuscript.

### **Available from:**

NASA Center for AeroSpace Information  
7121 Standard Drive  
Hanover, MD 21076-1320  
(301) 621-0390

National Technical Information Service  
5285 Port Royal Road  
Springfield, VA 22161  
(703) 487-4650

## TABLE OF CONTENTS

	Page
SUMMARY.....	1
INTRODUCTION .....	2
RESULTS AND DISCUSSION .....	4
Analysis and Classification of the 2-D Force and Moment Data .....	5
Examination of Instantaneous Pressure Data.....	10
Reduced Frequency Effect.....	15
CONCLUSION.....	24
REFERENCES .....	26
TABLES .....	29
FIGURES .....	31

## SUMMARY

The purpose of this study was to examine the previously unpublished instantaneous pressure data of the Aeroflightdynamics Directorate Two-Dimensional (2-D) and Three-Dimensional (3-D) Oscillating Wing Experiment in order to better understand the process of dynamic stall vortex development on the NACA 0015 airfoil.

The lift, drag, and pitching moment data of various testing conditions were reviewed and analyzed in order to classify the data both with and without a boundary layer trip, into "no stall," "moderate stall," and "deep stall" data. These trends of data with and without a boundary layer trip are generally discussed. Instantaneous pressure distributions on the upper surface of the airfoil are plotted and examined to study vortex development. The 2-D pressure data analysis is based on the mid-span of the NACA 0015 wing. Close examination of the instantaneous pressure distributions on the NACA 0015 airfoil reveals that the vortex development imprint is not easily seen in the pressure data. However, further examination of the pressure data indicates that the NACA 0015 airfoil exhibits trailing edge separation, which will be explained later.

The lift and pitching moment data are analyzed to document the dynamic overshoot which delays the development of stall on the airfoil. This dynamic overshoot is a result of the dynamic motion of an airfoil. The unsteady flow data are then compared with the quasi-steady data to examine the nature of the dynamic overshooting occurring during dynamic stall of the NACA 0015 airfoil. The range of angles of attack is selected where the lift and pitching moment data show significant changes from unsteady flow behavior during oscillation cycles. The instantaneous pressure distributions are closely examined at these angles of attack to capture any development that is not easily seen on the instantaneous pressure distributions based on the complete cycle. This refined study of the pressure distributions indicates that even though there are no apparent vortex imprints in the pressure distributions, even for the case of a severe deep stall, there is a clear tendency for the suction pressure on the aft section of the airfoil increasing with an increase in the angle of attack. This increase may occur because a vortex is developed *mildly* on the NACA0015 airfoil, moves along the airfoil, leaves the airfoil, and consequently causes an increase in lift, drag, and negative pitching moment.

Furthermore, based on the unsteady flow characteristics found in each classification of dynamic stall, the analysis is continued to identify the conditions under which the reduced frequency clearly affects the unsteady flow behavior of the airfoil during the oscillation. This can result in a change of the dynamic stall classification of the airfoil response under various unsteady flow conditions. These conditions are discussed in detail in the comparative studies for determining the reduced frequency effect on the dynamic stall response. Noting that the overall trends of the data with and without a boundary layer trip are equally covered in the discussion of the classification of dynamic stall, the analysis of the reduced frequency effect is focused mainly on the data with a boundary layer trip. Even though there are some distinct differences in the trends between the data

with and without a boundary layer trip, the most of general trend of the unsteady flow behavior of the data with a boundary layer trip is close to the unsteady flow behavior of the data without a boundary layer trip, without the complications caused by the variation of the transition point on the airfoil during oscillation. Therefore, this report puts more emphasis on the data with a boundary layer trip in the detailed analysis, although the overall trend of the data without a boundary layer is generally discussed.

## INTRODUCTION

The Aeroflightdynamics Directorate (AFDD) 2-D and 3-D Oscillating Wing Experiment (OWE) was previously conducted in the 7 x10 Foot Wind Tunnel at AFDD, using a wing with a NACA0015 airfoil section as a test model (ref. 1). The objective of this experiment was to establish a high - quality data set to be used for the validation of computational tools which numerically simulate the phenomenon of dynamic stall of oscillating airfoils and wings. The test data included two-dimensional (2-D) and three-dimensional (3-D) unsteady lift, drag, and pitching moment variations at various ranges of angles of attack including stall, as well as instantaneous pressure distributions taken at intervals throughout the oscillating cycle. One of the unique features of this test was the 3-D data set which extensively documented the flow along the span of a 3-D wing at the same conditions as recorded for 2-D in the same test environment. The lift, drag, and pitching moment data containing the 2-D and 3-D data were previously published in reference 1; the instantaneous pressure distributions for the 2-D test conditions are presented in this report for the first time.

A vortex usually forms near the leading edge and is shed along the chord of the airfoil during the dynamic stall process, as shown in the plots of lift, drag, and pitching moment versus angle of attack (fig.1)(ref. 2). However, analysis of the airfoil stall process leading to dynamic stall requires an in-depth analysis of the instantaneous pressure data in addition to the lift, drag, and pitching moment data, since information about dynamic stall vortex development cannot be fully obtained from the lift, drag, and pitching moment data.

The performance of rotorcraft is critically limited by dynamic stall, which generally occurs on the retreating side of the rotor blade, as a result of a rapid increase of the angle of attack of the blade (ref. 3). Recent examination of flight loads data (ref. 4) has revealed that rotor blades exhibit the dynamic stall phenomenon not only on the retreating side of the rotor disk but also on the advancing side during maneuvering flight conditions. And modern rotorcraft will be required to perform even more demanding missions, which will force the rotorcraft to work to the limit of the flight envelope.

The phenomenon of dynamic stall occurs when a rotor blade, airfoil, or wing undergoing dynamic motion, tends to gain additional lift with a rapid increase of the angle of attack past the static stall angle of attack, but experiences an undesirable negative pitching

moment when this additional lift is lost during dynamic stall. This negative pitching moment is caused by a vortex which is developed and shed along the chord of the oscillating airfoil and produces the pitching moment on the airfoil (ref. 5). Several studies of dynamic stall have been performed in efforts to properly understand the physics and characteristics of the complex unsteady flow of oscillating airfoils undergoing dynamic motion (refs. 6-13). Theoretical aspects of the dynamic stall phenomenon were well explored in previous analyses (refs. 14-18). Detailed events of the dynamic stall process were generally well defined in previous extensive experimental analyses. Note that the dynamic stall process, in the case of the NACA 0012 airfoil, is composed of flow reversal, the appearance of large eddies in the boundary layer, the formation of the dynamic stall vortex, a lift slope increase, the occurrence of maximum negative pitching moment, and boundary layer reattachment (fig. 1) (ref. 2). The dynamic stall events are also shown in figure 2 (ref. 15). In a separate study of separation and transition, the boundary layer on an oscillating airfoil was examined in terms of the skin friction coefficient, and by means of vorticity and velocity distribution (ref. 19).

The basic differences in the flow characteristics between the steady separation on an airfoil and unsteady flow on an oscillating airfoil are diagrammed in figures 3 and 4 (ref. 2). These diagrams show that the unsteady flow tends to be attached on the aft section of the airfoil during the dynamic stall process, and that the airfoil in steady flow shows separation on the aft section of the airfoil. The various parameters affecting dynamic stall include reduced frequency, mean angle, oscillation amplitude, Reynolds number, Mach number, and sweep angle. Some effects of these parameters on the dynamic stall process have been studied in detail (refs. 13-16 and 18). A discussion of the importance of dynamic stall parameters is shown in table 1 (ref. 14). Airfoil stall in steady flow is classified into three types: thin airfoil, leading edge, and trailing edge (ref. 4). In a steady flow environment, the airfoil thickness affects the type of stall process. In an unsteady flow environment, airfoil thickness (and leading edge radius) continues to be significant; when combined with the various parameters mentioned above, they significantly affect the dynamic stall process individually or interactively.

In the case of the NACA 0012 oscillating airfoil, a major study of dynamic stall vortex development was performed at AFDD (refs. 7, 11 and 13). Carr, et. al., described in great detail the unsteady flow behavior and characteristics of the NACA0012 airfoil undergoing the dynamic motion leading to dynamic stall. In the case of the NACA 0015 airfoil, the AFDD 2-D and 3-D Oscillating Wing Experiment (ref. 1) was the first experimental study of the NACA 0015 airfoil/wing dynamic stall at AFDD. This experiment established an extensive database over a NACA 0015 oscillating wing in various testing conditions over a wide range of angles of attack, simulating flow conditions similar to those in the rotor blade flow environment. The instantaneous lift, drag, and pitching moment coefficient data of the NACA 0015 oscillating wing computed from the pressure data measured in the experiment were documented by Piziali (ref.1). That report completely covered the 2-D and 3-D force and moment data cases at all conditions tested in the experiment. However, the report did not include the instantaneous pressure data obtained from the experiment.



The present report begins with an analysis of the 2-D data sets of lift, drag, and pitching moment coefficients and presents the instantaneous pressure data and then an analysis of these pressure data, in order to accurately understand the vortex development process of the NACA 0015 airfoil occurring during dynamic stall. This report is focused on the 2-D data, since the 3-D data consist of the extensive cases of spanwise variations along the wing and require more complex in-depth analysis, including the identification of 3-D effects. The previous AFDD NACA0012 airfoil test cases included only 2-D data, but the AFDD OWE NACA 0015 wing test included both 2-D and 3-D data. There were a limited number of 3-D experiments conducted in past dynamic stall studies (refs. 1, 20, and 21). However, the present set of 2-D data is one of the few test cases of a 3-D experiment in which 2-D data were additionally tested in a dynamic stall study.

## RESULTS AND DISCUSSION

In this section, the force and moment data are analyzed to globally establish the trend and characteristics of the unsteady flow response of the NACA 0015 airfoil during dynamic stall. Then the instantaneous pressure data are further examined in order to understand the unsteady flow behavior and vortex development phenomenon of the NACA 0015 airfoil during dynamic stall. The data originally obtained from the experiment were unaveraged pressure data including the cycle-to-cycle variation during the test, measured using absolute and differential pressure transducers at the various span locations of the wing. These unaveraged data were *ensemble averaged* over 20 cycles to form the basis of the present analysis. The ensemble-averaged pressure data were numerically integrated using a special function (ref. 22) to calculate the lift, drag, and pitching moment data. The complete data sets of lift, drag, and pitching moment versus angles-of-attack for the 2-D and 3-D tests were then published in reference 1, which also describes the test method and procedures. The testing conditions for the 2-D unsteady flow simulation conducted in the experiment were as follows:

- The mean angles selected in the test were  $1^\circ$ ,  $4^\circ$ ,  $9^\circ$ ,  $11^\circ$ ,  $13^\circ$ ,  $15^\circ$ , and  $17^\circ$
- The amplitudes were set to  $2^\circ$ ,  $4^\circ$  and  $5^\circ$
- The reduced frequencies tested were 0.04, 0.1, 0.14, and 0.19

This dynamic stall test focused primarily on the effect of change of the mean angle, change of amplitude, and change of the reduced frequency. Parameters such as Mach number and Reynolds number were not changed (approximately, Mach number= 0.3 and Reynolds number =1.9-2.0 million). Measurements were performed with and without a boundary layer trip. The boundary layer trip was installed on the upper surface of the airfoil to simulate the transition of the flow over the airfoil surface. All tests were done with and without the trip except for the case of  $\alpha=1.0^\circ \pm 4.0^\circ$ , where only no-boundary

layer trip data were obtained. A complete summary of the 2-D data test matrix is shown in table 2. In the experiment, a number of quasi-steady testing conditions were chosen to provide basic information about the steady behavior of the NACA 0015 wing/airfoil. Typical data of the quasi-steady case are presented in figure. 5.

### **Analysis and Classification of the 2-D Force and Moment Data**

The 2-D test cases shown in reference 1 are selectively reviewed and analyzed to understand and characterize the unsteady flow behavior of the NACA 0015 airfoil during the dynamic stall process. Based on the unsteady flow response to different conditions of testing parameters, 2-D data files are classified in three categories of dynamic stall behavior: *no-stall*, *moderate stall (light stall)*, and *deep stall*. The general classification is discussed in reference 14. The classification of the unsteady flow characteristics in this analysis was made based on examination of the pitching moment data. The classification of moderate stall or deep stall is subjective, based on the severity of the response of the pitching moment. However, in this analysis, the classification is made based on the following criteria, which are similar to definitions given in reference 14:

No stall: Linear responses noticed in the lift, drag, and pitching moment data, slight hysteresis observed, no negative pitching moment generated

Moderate stall: Mild hysteresis observed in the lift, drag, and pitching moment, increases in drag and mild excursion of the pitching moment and negative pitching moment generated.

Deep stall: Highly nonlinear responses observed, severe hysteresis, large excursion of the pitching moment. Specifically, data with an abrupt change that is clearly noticeable in the hysteresis of the pitching moment with a significant amplitude of the maximum pitching moment are considered to constitute a deep stall case. In this analysis, the definition is supported in that the magnitude of the maximum pitching moment is as much as  $-0.15$  or beyond is classified as deep stall, recalling that the maximum pitching moment in a complete range of the 2-D data case occurs approximately at the magnitude of  $-0.32$ . It is noted that the maximum positive pitching moment coefficient is approximately  $0.062$ .

Examples that show the classification presented in reference 14 are shown in figure 6. Specific examples of each classification for the AFDD OWE 2-D data for the study of the dynamic stall vortex will be given in the section, Analysis of Instantaneous Pressure Distributions. A summary of the 2-D test matrix with the above-described stall classification is shown in table 3, which gives an indication of how different parameters such as mean angle, amplitude, and reduced frequency affect airfoil response to the unsteady flow.

From table 3, the following observations are made.

2° Amplitude: For this case, attention is on the data with a boundary layer trip on the airfoil. The response of the airfoil to the various combinations of reduced frequencies and mean angles of 4°, 9°, and 11° are classified as the condition of the no stall case. Typical selected examples are shown in figure 7. Figure 7(a) shows the lift, drag, and pitching moment coefficient of the testing condition with the mean angle of 4° and the reduced frequency of 0.19; figure 7(b) contains the lift, drag, and pitching moment coefficients for the mean angle of 8° and the reduced frequency of 0.1. Figure 7(c) shows that the lift, drag, and pitching moment curve for the mean angle of 11° has characteristics of the no stall response.

The case of a mean angle of 13° shows no stall behavior at the higher reduced frequencies; the airfoil data show moderate dynamic stall at the lower frequency of 0.04. As selected examples, cases of the reduced frequencies of 0.04 and 0.14 for the mean angle of 13° are presented in figure 8. Figure 8(a) shows that the airfoil experiences moderate stall represented by a large increase in drag and a significant pitching moment. However, it is evident that the airfoil experiences no stall in the case shown in figure 8(b). In fact, this latter case can be a good candidate for the numerical simulation to determine that this phenomenon can be captured accurately, even in the computational analysis.

Cases of a mean angle of 15° have a moderate stall response in a wide range. A higher reduced frequency increases the severity of the moderate stall, represented by additional increments of the lift and drag and abruptness in pitching moment (fig. 9). This case is in contrast to the change seen in figure 8. This can be another good candidate for the numerical simulation.

In the case of a mean angle of 17°, the airfoil exhibits moderate stall at reduced frequencies of 0.04, 0.1, and 0.14. However, the increase of the frequency to 0.19 changes the airfoil's behavior from moderate stall to deep stall, since high reduced frequency delays the dynamic stall. Selected examples are shown in figures 10(a) and 10(b), where the moderate stall and deep stall data cases for the case of the mean angle of 17° are illustrated. In figure 10(a), the lift and drag increase moderately with angle of attack change, and a negative pitching moment has been generated. Figure 10(b) shows the deep stall case for a reduced frequency of 0.19, accompanied by the highly nonlinear response of a large magnitude of lift and drag and a factor-of-3 greater negative pitching moment.

Additionally, the trends observed in the boundary layer trip data mentioned above can be found in the case of no-boundary layer trip data. Typical examples for these cases with no-boundary layer trip are shown in figures 11-13. Figure 11 shows the lift, drag, and pitching moments for the selected case of no stall data with the no boundary layer trip data with mean angles of 3°, 8°, and 11°. The testing parameters are very similar to cases with boundary layer trip data, as shown in figure 7. The increase of the reduced frequency changes the dynamic stall process from moderate stall to no stall in the case of a mean angle of 13° with the amplitude of 2° (fig.12). This is close to the trend observed

in the case of the boundary layer trip data tested in very similar testing conditions (fig. 8). Figure 13 shows that the airfoil exhibits a wide range of moderate stall response at selected reduced frequencies for the case of a mean angle of  $15^\circ$ . The severity of the stall is changed owing to an increase in the reduced frequency. This trend is very close to the data case with a boundary layer trip, as previously shown in figure 9. Figure 14 shows a moderate stall response of a mean angle of  $17^\circ$  at selected reduced frequencies. At the same high reduced frequency of 0.19, the response of the airfoil with a boundary layer trip, where a mild deep stall phenomenon is observed (fig. 10(b)), is different from the case of no-boundary layer trip data, where the response is characterized as moderate stall.

A direct comparison is made between the airfoil with boundary layer trip and the airfoil with no-boundary layer trip in the case of the same testing conditions. A few examples are discussed here. The first example is shown in figures 15(a) and 15(b). Figure 15(a), which was discussed above (fig. 8(a)), shows the airfoil response with the boundary layer trip in the case of the reduced frequency of 0.04 for the mean angle of  $13^\circ$ . In figure 15(b), the response of the airfoil without the boundary layer trip is presented, as previously shown in figure 12(a). Both cases indicate that the airfoil experiences moderate stall and that the trends of the responses are very similar to each other. However, differences between two cases are seen in the severity of the response. The airfoil with boundary layer trip shows a more severe response of the moderate stall phenomenon, which is accompanied by larger drag and negative pitching moment. The boundary layer trip is used to cause the flow to change artificially from laminar to turbulent. It is viewed that the airfoil without boundary layer trip has a wide natural transition from laminar to turbulent taking place along the chord of the airfoil. As a result, the response of the airfoil with boundary layer trip tends to be more severe than the response of the airfoil without boundary layer trip.

The second example is shown in figures 16(a) and (b). In this case, the responses of the airfoil with boundary layer trip and without boundary layer trip, for the testing condition of a mean angle of  $15^\circ$  with reduced frequency of 0.14, are discussed. In figure 16(a), the response of boundary layer trip data is shown. The airfoil exhibits the moderate stall phenomenon, as indicated by a slight increase of lift, a drag rise, and a gradual increase of the negative pitching moment. Figure 16(b) shows a moderate stall response of the airfoil without boundary layer trip. The response is quite similar in both cases. In this case, the maximum drag of the airfoil with boundary layer trip generated during the dynamic stall process is larger than the drag of no-boundary layer data. The maximum negative pitching moment generated is slightly larger in the boundary layer trip data case.

The third case is presented in figure 17. The airfoil with and without boundary layer trip is tested at the condition of the mean angle of  $17^\circ$  and reduced frequency of 0.19. Figure 17(a) shows the case of boundary layer trip data. As briefly mentioned above (fig. 10(b)), the airfoil experiences mild deep stall, since a very large drag rise is seen and a large negative pitching moment (above - 0.15) is generated despite the lack of abruptness in the response. In Figure 17(b), as previously shown in figure 14(b), the airfoil without boundary layer trip has a moderate stall response, accompanied by a linear

drag rise and a gradual increase of the negative pitching moment. In this case, the boundary layer trip causes the severity of the dynamic stall process.

4° Amplitude (boundary layer trip data): For mean angles of 4° and 9°, the airfoil has no stall phenomena; selected of which examples are shown in figure 18. For a mean angle of 11 degrees, (fig. 19(a)), at the reduced frequency of 0.04, the airfoil exhibits the moderate stall phenomenon. However, the case at the higher reduced frequency of 0.1 shows no stall (fig.19(b)). It is worth noting that at this flow condition a higher reduced frequency eliminates dynamic stall.

In figure 20, the airfoil with mean angles of 13° shows generally a moderate stall phenomenon. In the case of the lower reduced frequency of 0.038 (figure 20(a)), the moderate stall becomes severe, accompanied by a tendency of a rapid decrease in the lift and an abruptness in the pitching moment. In the case of the data with reduced frequency of 0.14, where the dynamic stall has been reduced to mild moderate stall, figure 20(b) shows this difference in data between the severe moderate stall and mild moderate stall at different reduced frequencies with this mean angle.

In the case of a mean angle of 15, figure 21 shows that the airfoil undergoes a generally deep stall process at higher reduced frequencies. At a low reduced frequency of 0.038 (fig. 21(a)), the airfoil response is characterized as a severe moderate stall, represented by a relatively sharp decrease in lift and a large increase in drag and an abrupt change in pitching moment. It can be seen that as the reduced frequency increases, the airfoil response changes to a deep stall, since a high reduced frequency intensifies the severity of dynamic stall (fig. 21(b)).

The airfoil response of the mean angle of 17° has reduced frequency. At a lower reduced frequency (fig. 22(a)), the airfoil response is a moderate stall; while a deep stall is noted in the case of high reduced frequency (fig. 22(b)). An increase in reduced frequency causes the airfoil to change the response from moderate stall to deep stall.

4° Amplitude (no-boundary layer trip): The airfoil with no-boundary layer trip generally behaves similarly to that observed in the boundary layer trip data cases. Selected examples of these trends are shown in figures 23 – 27. Figure 23 shows that data for the mean angles of 4° and 8° with no-boundary layer trip at selected reduced frequencies show no stall at given unsteady conditions. This compares with similar test cases of boundary layer-tip data, as previously shown in figure 18. In figure 24, where selected examples of the mean angle of 11° are presented, the unsteady flow behavior of the airfoil changes from moderate stall to no stall with an increase in reduced frequency. In the case of the mean angle of 13°, the airfoil shows generally moderate stall, changing from mild to severe as the frequency increases (fig. 25). In general, this trend is in contrast to the data case with a boundary layer trip, previously shown in figure 20. In fig. 20, it can be seen that the airfoil response changes from severe moderate stall to mild moderate stall. The response of the airfoil tested with a mean angle of 15° with no boundary layer trip indicates that the reduced frequency causes the airfoil to change from moderate stall to deep stall with an increase in frequency (fig. 26). This is very similar to

the data case with a boundary layer trip, as presented earlier in Fig. 21. In the case of the mean angle of  $17^\circ$  a comparison is made between the data with the reduced frequencies 0.04 and 0.1 (fig. 27). The airfoil reacts moderately to the unsteady flow condition at the lower frequency of 0.04; the data show the deep stall phenomenon at the frequency of 0.1. A similar trend is observed for the same testing conditions for the data with a boundary layer trip, as observed in figure 22.

In the case of the direct comparison between boundary layer trip data and no-boundary layer trip data, the following cases are reviewed. In figures 28(a) and 28(b), the comparison case of the mean angle of  $11^\circ$  and reduced frequency of 0.04 is presented. Figure 28(a) shows the response of the airfoil with boundary layer trip, as previously cited in figure 19(a). The response indicates that the airfoil experiences mild moderate stall, as characterized by a slight increase in lift, a small magnitude increase in drag, and a small increase in the negative pitching moment generated during dynamic stall. Similarly, the no-boundary layer trip case shows moderate stall phenomenon (fig. 28(b)), but this response is slightly milder than the response of the boundary layer trip data. Figures 29(a) and 29(b) show the unsteady flow response of the airfoil with and without boundary layer trip for the case of a mean angle of  $13^\circ$  and a reduced frequency of 0.04. In figure 29(a), the case of the data with boundary layer trip is presented, as previously shown in figure 29(b). The response of the airfoil is classified as moderate stall based on the criterion that the maximum negative pitching moment coefficient is less than  $-0.15$ , even though the lift response is characterized by an abrupt loss and the generation of a sharp drag rise. It is considered as a severe case of moderate stall. In the case of no-boundary layer trip, also shown before in figure 25(a), the airfoil exhibits similar but less severe moderate stall responses, when compared with the boundary layer trip case (fig. 29(b)).

**$5^\circ$  Amplitude:** The review of the lift, drag, and pitching moment of the airfoil subjected to motion of amplitude of  $5^\circ$  at the mean angles of  $13^\circ$  and  $17^\circ$  indicates that both the boundary layer trip data and no-boundary layer trip data show a deep stall phenomenon.

As an example, the case of a boundary layer trip with a mean angle of  $17^\circ$  is shown in figure 30, where a deep stall is seen at both reduced frequencies. The increase of reduced frequency puts the response of the airfoil into a deeper stall during the dynamic stall process. Figure 31 shows the case of the no-boundary layer trip data with the mean angle of  $17^\circ$ . The increase of the reduced frequency from 0.038 to 0.1 causes the change of response from moderate stall to deep stall. This pattern is different from that of data with a boundary layer trip, shown in figure 30(a), where the airfoil response is defined as deep stall even at the lower reduced frequency of 0.038.

When figures 30 and 31 are reviewed for direct comparisons of the boundary layer trip data (fig. 30) and no-boundary layer trip data (fig. 31) in very similar flow conditions, it is seen that the airfoil with boundary layer trip experiences more severe dynamic stall than the airfoil without boundary layer trip. The boundary layer trip contributes to the severity of the response. This trend is similar to that of the previous direct comparison cases discussed above.

In addition to the above trends, the analysis of the data based on parametric changes reveals that the amplitude plays a major role in producing the dynamic stall in a high amplitude case. Two examples are presented in figures 32 and 33. As in the first example, cases of the mean angle of  $13^\circ$  with different amplitudes of  $2^\circ$  and  $4^\circ$  are shown in figure 32. From this comparison, it is seen that at the given reduced frequency, an increase of the amplitude contributes to the severity of stall during the moderate stall process, as characterized by a sharp decrease in lift, additional increase of drag, and generation of a larger magnitude of negative pitching moment (note the changed scale for the pitching moment). In the second example of the mean angle of  $15^\circ$ , a similar trend to the first case is found (fig. 33). The increase in reduced frequency usually causes much more severe dynamic stall in the case of higher amplitude angles of  $2^\circ$ ,  $4^\circ$  and  $5^\circ$ . Examples with and without a boundary layer trip include various previous examples, such as those shown in figures 9, 10, 13, 14, 21, 22, 25 – 27, 30, and 31. However, for some cases, this trend does not hold true, so that the airfoil experiences less separation at the higher reduced frequency. Examples that support these findings have already been shown in figures 8, 12, 20, and 24 for both the boundary layer trip and no boundary layer trip data case. The contribution of the reduced frequency is less significant for the case of the data for lower mean angles with small amplitudes. A typical example is shown in figure 34, which shows that reduced frequency makes no major contribution to unsteady flow behavior at these low angle unsteady flow conditions and, consequently, does not cause the airfoil to exhibit dynamic stall during dynamic motion.

### **Examination of Instantaneous Pressure Data**

A review and analysis of the lift, drag, and pitching moment data gives a global view of the unsteady flow response of an airfoil undergoing dynamic motion in the dynamic stall process. However, local flow behavior, such as flow separation, cannot be extracted from the force and moment data and cannot be properly understood by examining force and moment loops alone. Analyses of these data do not provide sufficient information about the development of the dynamic stall vortex on the airfoil, since only the global response of an airfoil undergoing a dynamic motion during dynamic stall can be basically established in the force and moment data. (as shown in the previous section) Therefore, instantaneous pressure data should be examined and analyzed. From an examination of instantaneous pressure distributions, the flow separation characteristics of the airfoil can be deduced, such as leading edge separation or trailing edge separation, and vortex formation phenomena can be examined.

**Behavior of the NACA 0012 Airfoil:** To illustrate this view, an example of lift, drag, and pitching moment data for the NACA 0012 airfoil is shown in figure 35 (ref. 12). From these plots, we can see that the airfoil experiences the deep stall phenomenon, as defined earlier. However, by examining these data alone, it is not feasible to determine that a vortex has developed or what kinds of flow separation have occurred during dynamic stall on the airfoil. The instantaneous pressure data should be examined in to find these kinds of information.

As will be seen later, the NACA 0015 airfoil dynamic stall vortex does not leave a strong imprint on the instantaneous pressure distributions. Therefore, a brief review of the effect of the dynamic stall vortex on the instantaneous pressure distributions of the NACA 0012 airfoil, where the imprint of the dynamic stall vortex is much more dramatic, is now presented so that the reader can better understand the unsteady effects that occur during dynamic stall. It is hoped that this preview will make analyses of the NACA 0015, with its weaker vortex structure, clearer. It should be noted that the instantaneous pressure being analyzed is measured on the upper surface, where the suction pressure occurs. The upper surface pressure plays a prominent role in the stall process. Therefore, the lower surface pressure is not plotted on the graphs of instantaneous pressure distribution used for examining the presence of any dynamic stall vortex. A typical graph of instantaneous pressure distributions is shown in figure 36(a) (ref. 12).

The presence of the dynamic stall vortex development on the airfoil is usually determined from a sharp or abrupt increase of pressure that is very noticeable in the instantaneous pressure distribution plot constructed in a complete oscillating cycle. Figure 36(a) (ref. 12) shows the  $C_p$  variation which occurs on the NACA 0012 airfoil when no stall is present. Note that these plots all show negative pressure values, so that an abrupt increase in pressure appears as a drop in the  $C_p$  shown in the graph. An example showing a vortex development occurring during dynamic stall is presented in figure 36(b) (ref. 12). This is the case of the NACA 0012 airfoil with  $\alpha = 15^\circ \pm 10^\circ$ , with a reduced frequency of 0.15.

Figure 36(b) clearly shows that suction pressure on the NACA 0012 airfoil suddenly decreases at the angle of  $20.8^\circ$ . The suction decrease is followed by an increase in suction which moves progressively along the chord as the angle increases to  $24.8^\circ$ . This shows that a vortex has developed and has moved along the airfoil during the dynamic stall process. This is dramatically different from the case of the instantaneous pressure distribution with no vortex development of the no-stall data, where there exists no abrupt decrease in suction with the increase in angle of attack, as shown in figure 36(a). Additionally, figure 36(b) shows that the NACA 0012 airfoil loses suction pressure dramatically in the vicinity of the leading edge as the angle changes from  $20.8^\circ$  to  $23.1^\circ$ . The suction pressure remains low as the angle of attack increases during oscillation. This indicates that the airfoil experiences leading edge separation during dynamic stall.

**Behavior of the NACA 0015 Airfoil:** Two different graphs of the instantaneous pressure data originally obtained from the measurements in the experiment will be presented here. First, all of the instantaneous pressure data measured in the experiment are plotted in terms of the chordwise location at a specific angle of attack to accurately evaluate the flow condition at the given time. Second, the instantaneous pressure data measured at various intervals in the oscillation cycle are presented for a complete oscillation cycle to properly characterize the unsteady flow behaviors developed during the testing condition.

**Deep stall case:** In studying the dynamic stall behavior of the NACA 0015 airfoil in the deep stall case, an extreme case is chosen in order to clearly capture the flow separation



characteristics and any vortex development behavior of the NACA 0015 airfoil occurring during the deep dynamic stall process. The following deep stall case is selected:  $\alpha = 17.08 \pm 5.18 \sin(\omega t)$  (degrees); and reduced frequency =  $k = 0.095$ .

The lift, drag, and pitching moment plots for these data at the mid-span location of the NACA 0015 airfoil are from reference 1 (fig. 37). It is clear that the response of the airfoil is very severe during the dynamic stall process, as indicated by the maximum gain of lift, the extreme drag increase, and the large excursion of the pitching moment.

In figure 38, the plot of the instantaneous pressure distributions is presented. The angle of attack varies from  $12.09^\circ$  to  $22.27^\circ$  and back to  $12.27^\circ$  in a complete oscillating cycle. These instantaneous pressure distributions show that there is a significant change of the suction peak pressure as the airfoil angle of attack increases from  $19.49^\circ$  to  $21.40^\circ$ . Furthermore, it is found that as the angle increases from  $19.49^\circ$  to  $21.40^\circ$ , there is a surge in suction that progresses down the airfoil – the imprint of the dynamic stall vortex (refer to fig. 39 for a detailed view). Thus a vortex has developed and has moved along the chord.

If the lift and pitching moment are expressed in terms of the phase angle (fig. 40), then the lift coefficient shows an abrupt change in the lift curve in the range of  $50^\circ < \text{phase angle} < 100^\circ$ , while the pitching moment changes in the range of the  $0^\circ < \text{phase angle} < 50^\circ$ , suggesting that the center of pressure on the airfoil has moved significantly long before the lift reaches a maximum. Since the unsteadiness is caused by the dynamic motion of the airfoil as a result of the change in angle of attack, the effects of the dynamic motion should be qualitatively examined by comparing the unsteady data with the steady data. However, in this experiment, there were no steady data available from the test. Instead, there were quasi-steady data available. The quasi-steady data measured in this experiment were obtained by varying the airfoil from the angle of  $0^\circ$  to  $21^\circ$  at a frequency from 0 to 0.04 cycle-per-second (cps). The quasi-steady data to be used in this analysis were previously shown in figure 5. The quasi-steady data show a minor oscillation; this can be attributed to the fact that the quasi-steady data are the unaveraged single cycle data.

Plots of the lift and pitching moment data for the above unsteady data and this quasi-steady data are shown in figure 41. A large dynamic overshoot is observed in the comparison of the lift and pitching moment data. The dynamic overshoot is defined as the momentary increase of lift or pitching moment with an increase in the angle of attack as a result of rapid motion of the airfoil. A vortex that developed during oscillation may be a major contributor to the phenomenon of dynamic overshoot. The pitching moment is closely examined to focus the investigation of the pressure analysis on angles of attack where the pitching moment is greatly increased during the stall process. The typical dynamic stall process shows that a vortex is developed at the leading edge, moves along to the trailing edge, and consequently results in an increase of lift and negative pitching moment. Generally, this increase of the pitching moment is technically viewed as an indication that a vortex may have developed and contributed to this increase of the

pitching moment. The graph of  $C_m$  (fig. 41(b)) shows that the pitching moment is significantly changed at the angles of attack from approximately  $19^\circ$  to  $21^\circ$ .

Plots of instantaneous pressure distributions for a complete cycle (fig. 38) were constructed to show representative pressure distributions at every  $13^{\text{th}}$  angle of attack in the total of 256 data samples of angles of attack in each cycle. They do not show all of the pressure measurements obtained from the experiment for every time step (or angle of attack). Therefore, a new plot has been made using all data samples in a selected range (referred to as refined pressure distributions plot). This plot has been constructed to show the instantaneous pressure distributions for every other time step. The maximum pressure obtained at every time step during the experiment is presented on each graph to give an accurate reading. This reading will be used to accurately assess any abrupt change in the peak pressure occurring during the oscillating cycle. The refined pressure distributions for  $\alpha=19.16^\circ$  to  $\alpha=21.90^\circ$  (fig. 42) show that the pressure gradually increases on the aft section of the airfoil, and that the drop in leading edge suction occurs as angles of attack increase. This increase of the pressure on the aft section of the airfoil is considered to be a result of the dynamic stall vortex generated in the dynamic stall process.

These particular testing conditions represent some of the most severe testing conditions of the NACA 0015 airfoil, as shown in the previous test matrix combined with the mean angle, amplitude, and reduced frequency. The plots of the lift, drag, and pitching moment versus angle of attack show that the airfoil experiences the most severe deep stall during the dynamic motion of this testing condition. However, the instantaneous pressure distributions reveal that the vortex formation occurring on the airfoil during the dynamic stall process does not leave a strong imprint on the graph of instantaneous pressure distributions. Therefore, the dynamic stall vortex development of the NACA 0015 airfoil in even the most severe case of the deep stall testing condition is relatively mild. It should be noted that there is no case in this study where the suction peak at the leading edge is ever fully lost. This is in strong contrast to the flow on sharper leading edge airfoils.

**Moderate stall case:** For a typical moderate stall case, the following flow conditions are selected for analysis:  $\alpha = 15.03 \pm 1.95 \sin(\omega t)$  (degrees); and reduced frequency =  $k = 0.038$ .

The complete plots of the lift, drag, and pitching moment of these data are shown in figure 43. It is evident from the hysteresis of the pitching moment that the airfoil has experienced a moderate stall condition during the oscillating motion, since the pitching moment changes gradually and its magnitude is not severe. The corresponding graph of the instantaneous pressure distribution (fig. 44) shows that the suction peak pressure at the leading edge has no major abrupt change during the dynamic motion of the airfoil, as the angles of attack change from  $13.09^\circ$  to  $16.95^\circ$  and back to  $13.10^\circ$  in a complete cycle of the oscillation. Consequently, it is seen that there is no clear vortex formation imprint

in the instantaneous pressure distribution. The instantaneous pressure distributions show that the airfoil undergoes trailing edge separation without a major drop in leading edge suction, since the suction pressure is reduced mostly at the back side of the airfoil chord as the angles changes during oscillation, as indicated by the flattening of the pressure curve at  $\alpha = 16.75^\circ$ . The corresponding detailed plot of surface plot versus chord position at this angle is shown in figure 45. It is seen that the flattening of the pressure occurs at the vicinity of the chordwise position  $x/c = 0.3$ . The additional plot for the case of an angle of  $16.92^\circ$  shows the flow characteristics of trailing edge separation during oscillation, as the flattening occurs at a similar chordwise position.

Plots of the lift and pitching moment versus phase angle are shown in Figure 46. From the curve of the lift, it is seen that the lift reaches a maximum and starts to decrease as the phase angle varies from  $0^\circ$  to  $50^\circ$ , whereas the magnitude of the pitching moment starts to change from  $-50^\circ$  to  $0^\circ$  and changes significantly in the range of the phase angle of  $0^\circ$  to  $50^\circ$ .

Figure 47 compares the moderate stall unsteady data and the quasi- steady data. From this comparison, the dynamic overshoot can be quantitatively assessed. The dynamic overshoot of the pitching moment owing to the unsteady motion of the airfoil is not significant; the graph of lift shows a gain of incremental lift. This finding is consistent with the fact that the dynamic stall vortex imprint is not apparently visible in the instantaneous pressure distributions of the unsteady data. Even though there is no obvious dynamic- stall- vortex imprint directly found in the instantaneous pressure distributions of the unsteady flow for a complete cycle, the presence of the vortex was further studied by examining any major change in the pitching moment data, based on the rationale that the vortex presence would eventually contribute to the increase of the negative pitching moment as the vortex leaves the trailing edge on the airfoil.

The plot of the pitching moment data (fig. 47(b)) indicates that the pitching moment changes considerably as the angle of attack varies from approximately  $15^\circ$  to  $16.5^\circ$ . To capture any major development that may not directly appear in the instantaneous pressure distributions for a complete oscillation cycle, the plot of refined instantaneous pressure distributions is further studied. Figure 48 shows the refined instantaneous pressure distributions for the given data generated for the range of angle of attack from  $15.08^\circ$  to  $16.70^\circ$ .

Close examination of the plot of refined instantaneous pressure distribution for these data shows that the suction peak pressures change gradually during oscillation. Also there are no major abrupt changes of the pressure and no clear dynamic stall vortex imprint found in the selected range of angles of attack where the pitching moment significantly changes. Therefore, it is concluded that during this moderate dynamic stall process, the NACA 0015 airfoil exhibits trailing edge separation and that there is no clear indication of a vortex development occurring on the NACA 0015 airfoil in the plot of instantaneous pressure distributions.

**No stall case:** The data selected for this case are as follows:  $\alpha = 8.97 \pm 2.04 \sin(\omega t)$  (degrees); and reduced frequency =  $k = 0.094$ .

The review of the lift, drag, and pitching moment data shows that at this condition the airfoil experiences no stall during the oscillating motion, since linear responses are seen with slight hysteresis and no negative pitching moment is generated in an oscillation of the airfoil (fig. 49). The corresponding instantaneous pressure distributions are generated for selected phases throughout the complete oscillating cycle (fig. 50). The angle of attack varies from a minimum of  $6.96^\circ$  to a maximum of  $11.01^\circ$  and back to  $6.98^\circ$  in a complete oscillating cycle. The maximum suction pressure coefficient generated during this cycle is  $-4.98$  at the angle of attack of  $11.00^\circ$ . It is clear from the pressure distributions that the flow at these conditions is fully attached throughout the testing condition during oscillation with no excursion present in the pitching moment. Obviously, the dynamic stall vortex has not formed under these conditions.

### Reduced Frequency Effect

In this report, the analysis of dynamic stall has been focused on the establishment of unique unsteady flow characteristics of the NACA 0015 airfoil based on three categories defined in the dynamic stall classification: no-stall, moderate stall, and deep stall. By using various approaches defined previously in this classification, the airfoil response of the NACA 0015 airfoil can be studied in terms of parameter change, such as mean angle, oscillating amplitude, and reduced frequency, in a wide range of testing parameters. Several of the data in table 3 are selected for a parametric study in order to examine effects of reduced frequency on the airfoil response. This approach is made to understand how the reduced frequency affects the dynamic stall behavior of the airfoil with the same mean angle and amplitude undergoing dynamic motion. table 3 contains both data with a boundary layer trip and data without a boundary layer trip. There are slight variations between the data with a boundary layer trip and data without a boundary layer trip. The effects of the reduced frequency found in the data with a boundary layer trip are similar to trends of the data without a boundary layer trip. This analysis focuses on the data with boundary layer trip.

The following data are selected for comparative studies of the dynamic stall process:

Angle of attack, degrees	Reduced Frequency
$13.0 \pm 2.0$	$k = 0.04 / k = 0.14$
$15.0 \pm 2.0$	$k = 0.04 / k = 0.14$
$17.2 \pm 2.0$	$k = 0.04 / k = 0.1$
$11.0 \pm 4.0$	$k = 0.04 / k = 0.1$
$17.0 \pm 4.0$	$k = 0.04 / k = 0.1$

These files are noted as either “No stall” or “Moderate stall”, or “Deep stall” in table 3.

**$\alpha = 13.0^\circ \pm 2.0^\circ$ , reduced frequency =  $k = 0.04 / k = 0.14$ :** This is a case where the airfoil exhibits moderate stall at a lower frequency, while the airfoil eliminates dynamic

stall at a higher reduced frequency. The corresponding data are as follows:  $k = 0.04$ ,  $\alpha = 13.07 + 1.97 \sin(\omega t)$  (degrees); and  $k = 0.14$ ,  $\alpha = 13.08 + 2.13 \sin(\omega t)$  (degrees). Lift, drag, and pitching moment plots (ref. 1) are shown in figure 51. In the case of  $k = 0.04$  (fig. 51(a)), the flow shows moderate stall: a nonlinear response accompanied by an increase in lift and drag, an abrupt pitching moment drop, and a slight increase in negative pitching moment is observed during oscillation of the airfoil. However, the response of the airfoil tested at  $k = 0.14$  in figure 51(b) shows that the airfoil has no dynamic stall flow response at this unsteady flow condition, where the no-stall condition is indicated by a slight hysteresis in lift, drag, and pitching moment data, with no negative pitching moment value generated.

In figure 52(a), the graph of instantaneous pressure distributions for the case of  $k = 0.04$  is presented at angles of attack ranging from  $11.03^\circ$  to  $15.04^\circ$  and back to  $11.05^\circ$ . The  $-C_p$  maximum of 7.35 is obtained at the angle of  $14.77^\circ$  (note that this angle is not on the curve, since the maximum angle is selected from 256 data samples in the complete oscillating cycle). Figure 52(b) shows the plot of instantaneous pressure distributions for the case of  $k = 0.14$ , which has a  $-C_p$  maximum of 7.61 at the angle of  $15.12^\circ$  (note that this angle is not on the curve, since the maximum angle is selected from 256 data samples in the complete oscillating cycle). An examination of both plots indicates that the suction peak pressure at the leading edge has no sudden drop throughout the oscillating cycle as the angle increases and decreases. Additionally, it is found that there is a mild flattening in the graph of the instantaneous pressure distributions for the case of  $k = 0.04$ , as the angle changes from approximately  $14.97^\circ$  back to  $14.17^\circ$  during oscillation. This indicates mild flow separation. However, the graph of the instantaneous pressure distributions for the case of  $k = 0.14$  shows no flattening trends along the chord throughout the cycle, which indicates that the airfoil has no separation during dynamic motion.

In the case of  $k = 0.04$ , there is a tendency for the pressure on the upper surface to increase slightly on the aft section of the chord, especially in the vicinity of the trailing edge area, as the angle increases during oscillation. An example for comparison from the oscillating cycle is  $14.81^\circ$  and  $14.97^\circ$  in the case of  $k = 0.04$  (fig. 54), which shows that the suction pressure peak slightly decreases with an increase in the angle of attack in this flow condition, and the negative  $C_p$  increases slightly beyond the location of  $x/c = 0.85$  in both angles.

Similarly, the plot of the upper surface pressure of the  $k = 0.14$  case at angles of  $14.55^\circ$  and  $14.89^\circ$  is examined (fig. 55). The suction peak pressure increases slightly at a higher angle of attack. But there is no change of the suction pressure generated along on the airfoil chord in both cases. The pressure at the trailing edge continues to decrease for the given angle. This is different from the development observed in the case of  $k = 0.04$ .

Figures 56 (a) and 56 (b) show that both the lift and the pitching moment of the unsteady flow condition for the case of  $k = 0.04$  have changed because of oscillation. However, in the case of  $k = 0.14$ , no significant change in the pitching moment is generated (fig. 57(b)). The pitching moment curve for the case of  $k = 0.04$ , shown in the previous plot

of figure 56(b), shows that a sudden drop of the pitching moment occurs approximately from  $14.49^\circ$  to  $14.98^\circ$ . However, there is no major change of pitching moment in the case of  $k = 0.14$  (as presented in fig. 57(b)). So only the case of  $k = 0.04$  is examined. Figure 58 is a graph of refined instantaneous pressure distributions for the case of  $k = 0.04$  generated for angles of attack from  $14.49^\circ$  to  $14.95^\circ$ . The graph shows that there is no major vortex development. However, the pressure increases slightly at the trailing edge area during the oscillation. This implies that the airfoil experiences trailing edge separation during dynamic motion.

**$\alpha = 15.0^\circ \pm 2.0^\circ$ , reduced frequency =  $k = 0.04 / k = 0.14$ :** In this case, the airfoil exhibits moderate stall at two different reduced frequencies. At a higher reduced frequency, the airfoil responds to the unsteady flow more severely than the response of a lower reduced frequency. The corresponding data are:  $k = 0.04$ ,  $\alpha = 15.03 + 1.95 \sin(\omega t)$  (degrees); and  $k = 0.14$ ,  $\alpha = 15.04 + 2.11 \sin(\omega t)$  (degrees).

The curves of lift, drag, and pitching moment for both cases of  $k = 0.04$  and  $k = 0.14$  are presented in figure 59. The data for  $k = 0.04$  (fig. 59(a)) show that the lift is slightly increased above the maximum of the static lift, the drag is similarly increased, and the negative pitching moment is gradually generated during oscillation of the airfoil. So, this nonlinear response is classified as moderate stall. In the case of  $k = 0.14$  data (fig. 59(b)), it is observed that the airfoil experiences a more severe moderate dynamic stall, when compared with the case of  $k = 0.04$ , accompanied by a larger increase in lift, a large and abrupt increase in drag, and generation of a significant amount of negative pitching moment with an abrupt drop at the maximum angle of  $17^\circ$ .

Figure 60 shows the instantaneous pressure distributions for the case of  $k = 0.04$ , where the angle of attack changes from  $13.09^\circ$  to  $16.95^\circ$  and back to  $13.10^\circ$  in a complete cycle. This plot indicates that the pressure distributions over the rear part of the airfoil tend to flatten starting from approximately  $16.41^\circ$ , when compared with the pressure at the angle of  $15.96^\circ$ . Figure 61 shows instantaneous pressure at the selected angles of  $16.47^\circ$ ,  $16.70^\circ$ , and, particularly, at  $16.95^\circ$ . The pressure continues to fully flatten at an angle of  $16.10^\circ$  in the downstroke cycle (fig. 62): this flattening trend indicates that the airfoil experiences trailing edge separation, as the airfoil oscillates during dynamic motion. The graph of instantaneous pressure distributions for the case of  $k = 0.14$  is illustrated in Figure 63. An initial examination of the instantaneous pressure distributions shows weak development of a mild vortex generated during oscillating motion, represented by the increase of pressure near the aft section and trailing edge of the airfoil at the maximum angle. However, it does not show the flattening trend of pressure in the upstroke cycle. Pressures at selected angles of  $16.87^\circ$ ,  $16.97^\circ$  and  $17.04^\circ$  (upstroke) are compared for illustration (fig. 64). It is found that no abrupt loss of suction peak pressure is seen but is gradually decreased at leading edge. Also, the pressure does not show flattening along the chord of the airfoil.

To determine the effects of the dynamic motion on the airfoil flow, a comparison is made between the unsteady data with quasi-steady data. In the case of  $k = 0.04$  (figs. 65 (a),

65(b)), the additional gain of the lift is minimal, and the pitching moment is not much increased as a result of dynamic motion of the airfoil. However, in the case of  $k = 0.14$ , both lift and pitching moment of the  $k = 0.14$  case increase significantly because of oscillation throughout the complete cycle (figs. 66(a) and 66(b)). It should be noted that the trend of pitching moments of these cases will be further examined in the discussion below. It is noted that the pitching moment is substantially changed with a sudden drop from the angle of approximately  $15^\circ$  to  $16.5^\circ$  in figure 66(b). The corresponding graphs of refined instantaneous pressure distributions specifically covering these angles are presented in figure 67. From this instantaneous pressure distribution, it is found that there is no indication of any dynamic stall vortex development that occurred during the unsteady motion of the airfoil. However, there is generally a flattening of the pressure occurring from the mid-chord of the airfoil, as the angle changes from about  $16.41^\circ$  to  $16.81^\circ$ , as discussed previously. The dramatic change of pitching moment occurs approximately at the angles of  $16.0^\circ$  to  $17.1^\circ$  in figure 66(b). Note that the pitching moment follows the stalled quasi-steady data rather than the attached quasi-steady data. From the previous plot of instantaneous pressure distributions (fig. 63), a light imprint of a mild vortex generated during unsteady motion of the airfoil is present, when the data are examined closely at the range of angle of attack from  $16.03^\circ$  to  $17.07^\circ$ . This finding is based on the observation that the pressure increases aft section of the airfoil when it reaches to the maximum oscillating angle and that the airfoil exhibits quite a severe moderate stall phenomenon in the lift, drag, and pitching moment data in this unsteady flow condition. To support these findings, the pressure data at selected angles such as  $16.53^\circ$ ,  $16.87^\circ$ ,  $17.04^\circ$ , and  $17.07^\circ$  are presented in figure 68. It is seen that the suction pressure tends to gradually increase from mid-chord to the trailing edge of the airfoil chord, as the angle increases. This may imply that a very mild vortex is generated and moves along the airfoil chord.

**$\alpha = 17.0^\circ \pm 2.0^\circ$ , reduced frequency =  $k = 0.04$  /  $k = 0.19$ :** In this comparison, the airfoil experiences a change in the unsteady response from moderate stall to mild deep stall with the reduced frequency. The corresponding data are as follows:  
 $k = 0.04$ ,  $\alpha = 17.09 + 1.97 \sin(\omega t)$  (degrees); and  $k = 0.19$ ,  $\alpha = 17.09 + 2.26 \sin(\omega t)$  (degrees).

In figure 69, the graphs of the lift, drag, and pitching moment versus angle of attack for these cases are provided. As seen in figure 69(a), the response of the airfoil for  $k = 0.04$  is considered as moderate stall, as characterized by a considerable increase in drag and a gradual increase in negative pitching moment (note that the maximum negative pitching moment generated is much less than  $-0.15$  of the maximum negative pitching moment that was defined earlier for the deep stall classification), as the airfoil oscillates during dynamic motion. As for the  $k = 0.19$  case, Figure 69(b) shows that the response is accompanied by a large increase in drag and a large negative pitching moment. Therefore, it is still classified as deep stall because of the large magnitude of the pitching moment (greater than  $-0.15$ ), even though the response has no abrupt drop.

The graph of instantaneous pressure distributions for a complete cycle for the case of  $k = 0.04$  is shown in figure 70. This plot of instantaneous pressure distributions shows that the airfoil undergoes extensive pressure flattening with an increase in angle of attack during oscillation. Figure 71 shows the instantaneous pressure distributions at selected angles of attack of  $16.34^\circ$ ,  $18.82^\circ$ , and  $19.03^\circ$ . In this comparison, the following is observed: (1) the suction peak pressure decreases as the angle increases; (2) the pressures at the mid chord  $x/c = 0.55$  and  $0.850$  have slight increases; and (3) the flattening of pressure is widely seen at the higher angle.

Additionally, the pressure distributions at the angle of attack in the downstroke cycle are reviewed. Selected angles are  $18.16^\circ$ ,  $17.05^\circ$  and  $15.56^\circ$ . The pressure data at these angles are shown in figure 72. From these distributions, this flattening trend is continued in the downstroke during oscillation. Therefore, it is concluded that the flattening occurs extensively in the complete oscillating cycle. This flattening trend indicates that the airfoil undergoes trailing edge separation, as the airfoil oscillates with the change of angle of attack in this unsteady flow condition.

Figure 73 shows the instantaneous pressure distributions for a full oscillating cycle of the  $k = 0.19$  data case. An examination of this plot shows that the pressure has a slight increase at the mid-chord approximately at the angles of  $18.58^\circ$  to  $19.29^\circ$  in the upstroke of the oscillating cycle. The instantaneous pressure at selected angles of  $18.58^\circ$ ,  $19.01^\circ$ , and  $19.29^\circ$  in the upstroke are reviewed (fig. 74). From this comparison, it is found that (1) the suction peak pressure decreases as the angle of attack increases; and (2) the pressure at the mid-chord increases with a change of angle of attack. A slight increase in the pressure at the mid-chord may result from a mild vortex generated during the dynamic stall process, as the angle of attack of the airfoil varies.

The dynamic effects of the airfoil motion are further examined by comparing the unsteady data with the quasi-steady data (figs. 75 and 76). Figure 75 shows the comparison of lift coefficient and pitching moment versus angle of attack for the case of  $k = 0.04$  data. The graph of lift shows no dynamic overshoot, and the pitching moment shows little significance of the overshoot. However, the case of  $k = 0.19$  data, in figure 76, presents a significant dynamic overshoot in the pitching moment data, even though the lift overshoot is less significant when compared with the overshoot of the pitching moment. Note that the stalled lift curve has the same slope as the unstalled lift curve, but is shifted to higher angle.

The graphs of instantaneous pressure distributions at the range of  $\alpha$  where the pitching moment is significantly affected are generated. The pitching moment for the  $k = 0.04$  case, seen previously in figure 75b, shows no major abrupt change of the magnitude except for the range of  $\alpha$  from  $15.14^\circ$  to  $15.84^\circ$ . To further examine the pressure distributions for the range of these angles, the plot of the refined instantaneous pressure distributions is presented in figure 77. This plot shows that there is a gradual decrease in the suction peak pressure with an increase of angle of attack and flattening of the pressure at higher angles. In the case of  $k = 0.19$ , the pitching moment is changed greatly from the angle of approximately  $17^\circ$  to  $19.30^\circ$ . The corresponding plot of the instantaneous



pressure distributions from  $17.10^\circ$  to  $19.30^\circ$  is shown in figure 78. The suction peak pressure increases from the angle of  $17.10^\circ$  and reaches a maximum at  $17.92^\circ$  or  $17.97^\circ$  and then decreases gradually with an increase in angle of attack. Additionally, the suction pressure increases in the vicinity of the mid-chord approximately starting from an angle of  $18.00^\circ$ . This may indicate that a mild vortex has developed and moved along with the chord during oscillation of the airfoil in this unsteady flow condition.

**$\alpha = 11.0^\circ \pm 4.0^\circ$ , reduced frequency =  $k = 0.04$  /  $k = 0.1$ :** In this case, the behavior of the unsteady response changes from no stall to moderate stall with an increase of the reduced frequency. The corresponding data are  $k = 0.04$ ,  $\alpha = 10.88 + 4.07 \sin(\omega t)$  (degrees); and  $k = 0.1$ ,  $\alpha = 10.88 + 4.22 \sin(\omega t)$  (degrees).

The corresponding plots of the lift, drag, and pitching moment versus angle of attack for this case are shown in figure 79. The  $k = 0.04$  data (fig. 79(a)) indicate that the airfoil experiences moderate dynamic stall, since the lift is slightly increased, the drag is increased quite sharply at the maximum angle, and the negative pitching moment is abruptly generated. In contrast, in the case of the  $k = 0.1$  data (fig. 79(b)), it is clearly observed that the airfoil has no dynamic stall response, since the lift and drag have a very slight hysteresis and no negative pitching moment is generated.

The graphs of instantaneous pressure distributions for a complete cycle are presented. Figure 80 shows the plot of instantaneous pressure distributions for the case of  $k = 0.04$ . In this case, the oscillating angle of attack ranges from  $6.90^\circ$  to  $14.90^\circ$  and back to  $6.99^\circ$  in a complete cycle. There is an increase of the suction pressure at the trailing edge as the angle changes, especially in the range from  $12.15^\circ$  to  $14.84^\circ$ , and back to  $12.75^\circ$  during oscillation. Selected angles of  $9.78^\circ$ ,  $13.23^\circ$ ,  $14.06^\circ$ , and  $14.90^\circ$  of the upstroke cycle are plotted (fig. 81). From this plot, the following is observed: (1) the suction peak pressure increases with the increase of angle of attack; and (2) the pressure ( $-C_p$ ) at the aft section of the chord increases with the change of angle of attack. This latter increase in the pressure may relate to a very weak formation of the vortex development, since a sudden drop in  $-C_p$  max at the leading edge combined with a sudden drop in the pitching moment is generated at the maximum angle, even though maximum magnitude of the pitching moment generated during the oscillation is not quite large.

For the  $k = 0.1$  data shown in figure 82, the instantaneous pressure distributions shows that the unsteady flow in this condition has no characteristics to represent any typical dynamic stall phenomenon, such as a vortex imprint or flattening of the pressure at the mid-chord. Selected angles of  $9.61^\circ$ ,  $13.14^\circ$ ,  $14.06^\circ$  and  $15.07^\circ$  in the upstroke of the complete cycle are compared (fig. 83). From figure 83, it is seen that the suction peak pressure increases with an increase in angle of attack and this suction pressure decreases gradually along the chord. So there is no indication of flow separation.

A comparison with the quasi-steady data is made in figures 84 and 85. In figure 84, the lift and pitching moment of the unsteady data are compared with the quasi-steady data

for the case of  $k = 0.04$ . It is observed that additional incremental lift is gained owing to oscillation. The negative pitching moment increases because of dynamic motion. However, in the case of  $k = 0.1$  (fig. 85), the additional lift is obtained as a result of dynamic motion, but an increase in pitching moment makes less significant contributions, since no negative pitching moment is generated.

The pressure distributions will now be further evaluated for the range of angles of attack where the pitching moment is significantly changed. The graph of pitching moment for the case of  $k = 0.04$ , presented in the previous plot of figure 84(b), shows that there is a significant drop in the pitching moment from the angle of approximately  $14.90^\circ$  to  $14.00^\circ$ . The graphs of refined instantaneous pressure distributions for this case in this range of angle of attack is seen in figure 86. Note that the suction peak pressure is gradually decreased as the angle of attack changes from  $14.90^\circ$  to  $13.26^\circ$ . The pressure tends to slightly increase at the trailing edge, as the angle of attack changes in this range. The case of  $k = 0.1$  does not require a further review of the selected angles of attack, since the airfoil has no dynamic stall process in this unsteady condition.

**$\alpha = 17.0^\circ \pm 4.0^\circ$ , reduced frequency =  $k = 0.04 / k = 0.14$ :** In this comparison, an increase in reduced frequency changes the unsteady behavior of the airfoil response from moderate stall to deep stall. The corresponding data are  $k = 0.04$ ,  $\alpha = 17.05 + 4.03 \sin(\omega t)$  (degrees); and  $k = 0.14$ ,  $\alpha = 17.04 + 4.27 \sin(\omega t)$  (degrees).

Figure 87 shows the graphs of lift and pitching moment versus angle of attack for  $k = 0.04$  and  $k = 0.14$ . In the case of  $k = 0.04$ , the airfoil gains additional lift, a large drag increase and a gradual negative pitching moment because of the unsteady motion of the airfoil. This is a typical moderate dynamic stall phenomenon of the airfoil response owing to the oscillation. In contrast, the airfoil responds differently to the unsteady flow conditions of the  $k = 0.14$  data (fig. 87(b)). The response of the airfoil shows that an additional large amount of lift is gained and that an abrupt drop in lift follows, that a very large amount of drag is produced, and that a significant negative pitching moment is generated quite abruptly. The response of the airfoil in this unsteady flow condition is classified as a deep stall.

The corresponding plot of the instantaneous pressure distributions for the case of  $k = 0.04$  is shown in figure 88. It shows that the maximum suction peak pressure occurs at the angle of  $15.98^\circ$  and decreases gradually as the angle increases. This can be checked in detail by comparing several angles as shown in figure 89. In addition, it is found that there is a flattening trend of the pressure, as the angle approaches the maximum angle in the upstroke cycle and continues in the downstroke cycle. The pressure at selected angles of  $19.38^\circ$ ,  $20.19^\circ$ ,  $20.79^\circ$ , and  $21.02^\circ$  in the upstroke are compared in figure 90. This plot shows the flattening effect. Also, the pressure at selected downstroke angles is to show the continuation of this trend even in the downstroke cycle (fig. 91).

In the case of  $k = 0.14$  (fig. 92), the instantaneous pressure distributions shows that the angle changes from  $13.04^\circ$  to  $20.97^\circ$  and back to  $13.14^\circ$  in the complete cycle. It should

be noted that the maximum suction peak pressure ( $-C_p \max$ ) is defined to be selected at the angle in the data sample of the complete oscillating angles. In this case, it is seen that maximum suction peak pressure occurs at the angle of  $19.37^\circ$  in the upstroke cycle, even though the corresponding instantaneous pressure distributions at this angle are not shown in this plot, since this angle occurred between  $18.40^\circ$  and  $19.54^\circ$  in the plot. The suction peak pressure starts to decrease gradually from the angle of  $20.35^\circ$ . Note that the abrupt loss of the suction peak pressure occurs from approximately  $20.35^\circ$  through  $20.84^\circ$  to  $20.97^\circ$ . This loss is considered equivalently as the abrupt loss of lift at the maximum angle, as clearly seen in the plot of the lift versus angle of attack, as previously shown in figure 87(b). In the downstroke cycle, the suction peak pressure starts to slightly increase from an about angle of  $20.74^\circ$ . Furthermore, in this case, the additional important phenomenon is discovered: in the angle of attack range of approximately  $19.54^\circ$  and  $20.97^\circ$ , the pressure increases significantly in the aft section of the airfoil with an increase of the angle, especially at the angles of  $20.84^\circ$  and  $20.97^\circ$ . The instantaneous pressure distributions for the selected angles of  $19.54^\circ$ ,  $20.35^\circ$ ,  $20.84^\circ$ , and  $20.97^\circ$  are presented in figure 93. This increase in the pressure over the rear section of the airfoil is considered to be an indication of the physical phenomenon that a vortex has developed over the airfoil and traveled toward the trailing edge of the airfoil during oscillation of the airfoil in this unsteady flow condition. In fact, this particular case is one of few cases in the NACA 0015 airfoil data cases that really show the strong and clear imprint of the formation of the dynamic stall vortex occurring during the unsteady motion. This formation of the vortex is largely as a result of the large mean angle with large amplitude excited by a high reduced frequency.

Comparisons of the unsteady data and quasi-steady data are made (figs. 94 and 95). In the case of  $k = 0.04$  (fig. 94), the slight dynamic overshoots of the pitching moment curve are noticeable, while the lift plot shows no major gain. Figure 95 shows comparisons of the lift and pitching moment for the case of  $k = 0.14$ . In this case, it is noted that the stalled lift data have the same slope as the unstalled lift data but is shifted to high angle. The maximum lift coefficient at the maximum angle is approximately 1.7, which is much greater than the maximum static lift coefficient of 1.23. The maximum excursion value of the pitching moment coefficient is approximately 0.30 at the maximum angle of the oscillation. These dynamic overshoots observed in both lift and pitching moment comparisons are very significant. So, this large dynamic overshoot is another indication of a vortex development occurring during the dynamic motion of the airfoil. In fact, this indication supports the early claim that a clear imprint of the dynamic stall vortex is observed in the unsteady flow, based on the examination of the instantaneous pressure distributions discussed above.

The refined instantaneous pressure distributions are to be more closely examined, especially in the range of angles of attack where the pitching moment is significantly changed in the plot of the pitching moment versus angle of attack. In figure 94(b), the pitching moment is quite significantly changed from the angle of about  $14.0^\circ$  to  $17.08^\circ$ . In this range of angles of attack, the plot of the refined pressure distributions is generated (fig. 96). From these plot, it is observed that suction peak pressure gradually increases with the angle of attack, reaches the maximum at the angle of  $15.98^\circ$  and gradually

decreases with the angle of attack. Additionally, the suction pressures tend to gradually increase on the aft section of the airfoil as the angle increases in this range. It is concluded that no major imprint of a dynamic stall vortex is found in this unsteady flow condition.

In the case of  $k = 0.14$  data, the graph of the pitching moment (fig.94(b)) shows the abrupt change of the pitching moment from approximately the angle of  $18.0^\circ$  to the maximum angle of  $21.0^\circ$ . The corresponding plot of refined instantaneous pressure distributions for this range of the angle is shown in figure 97. The suction peak pressure reaches a maximum at the angles of  $19.37^\circ$  and  $19.47^\circ$  and decreases gradually as the angle increases. It is noted that the maximum suction peak pressure ( $-C_p \text{ max}$ ) at the maximum oscillation angle of  $20.90^\circ$  decreases to 4.40. Additionally, it is found that the significant pressure increases noticeably on the aft section, especially from an angle of about  $20^\circ$ . This indicates that a vortex has developed and is moved along the airfoil during the dynamic stall process. Therefore, this finding is in agreement with the early claims that a vortex has developed in this unsteady flow condition, which was discussed above.

## CONCLUSION

In the present study, the complete 2-D instantaneous pressure data of NACA 0015 airfoil test in addition to the lift, drag, and pitching moment data, have been examined to establish the unsteady flow characteristics of the airfoil and to study the vortex development occurring during the dynamic stall process. From this analysis, the following observations are made.

1. From an examination of suction peak pressure change in the instantaneous pressure distributions, it is concluded that the NACA 0015 airfoil does not exhibit leading edge separation. Instead, it exhibits trailing edge separation during dynamic stall for all the conditions studied.
2. Under very same testing conditions, the airfoil with boundary layer trip generally experiences more severe dynamic stall than the airfoil with no boundary layer trip. Based on the classification trend, the airfoil with no boundary layer trip generally behaves similarly to boundary layer trip data cases. In some cases, however, the effect of the reduced frequency on the airfoil response is different for the boundary layer trip data case and no- boundary layer trip data case.
3. Except in the very severe deep stall cases, the imprint of the dynamic stall vortex is not clearly evident in many of the instantaneous pressure distributions.
4. Significant dynamic overshoot is mainly noticed in the deep stall data, when the unsteady data are compared with the quasi-steady data. The dynamic overshoot is apparently caused by the boundary layer separation delay and a vortex developed on the airfoil. The vortex development contributes to gain of this additional lift and pitching moment.
5. Even though there is no distinctive dynamic stall vortex imprint on most of the instantaneous pressure distributions, analysis of instantaneous pressure distributions indicate that the pressures tend to show the flattening effect over the rear of the airfoil, which is an indication of trailing edge separation. The pressure noticeably increases on the aft section of the airfoil chord as the angle increases during the dynamic motion. This increase is caused by the dynamic stall vortex generated from the dynamic motion.
6. From various comparative studies, it can be seen that under different unsteady flow conditions, reduced frequency becomes a major parameter to change the unsteady flow behaviors and eventually the dynamic stall classification of the airfoil, such as from *moderate stall* to *no stall*, and from *moderate stall* to *deep stall*. These cases are recommended candidates for validation of computer models of dynamic stall.

7. NACA 0015 airfoil generally produces a mild vortex during the dynamic stall process in the most of deep stall cases, which is characterized by a mild increase of the pressure increase over the airfoil. This is significantly different from the NACA 0012 airfoil, which tends to generate a strong vortex during dynamic stall.

## REFERENCES

1. Piziali, R.: An Experimental Investigation of 2-D and 3-D Oscillating Wing Aerodynamics for a Range of Angles of Attack Including Stall. NASA TM - 4632, Sept. 1994.
2. Carr, L. W.; McAlister, K. W.; and McCroskey, W. J.: Analysis of the Development of Dynamic Stall Based on Oscillating Airfoil Experiments. NASA TN-D-8382, 1977.
3. Johnson, W.: Helicopter Theory. Princeton University Press, Princeton, N.J. 1980.
4. Bousman, W. G.: A Qualitative Examination Dynamic Stall from Flight Test Data. Presented at AHS Forum, Virginia Beach, Va., Apr. 29-May 1, 1997.
5. Prouty, R.: Helicopter Performance Stability and Control. 1986.
6. Ham, N. D.; and Garelick, M. S.: Dynamic Stall Considerations in Helicopter Rotors. J. of the American Helicopter Soc., vol. 13, no. 2, Apr. 1968, pp. 49-55.
7. McCroskey, W. J.; McAlister, K. W.; and Carr, L. W.: Dynamic Stall Experiments on Oscillating Airfoils. AIAA J., vol. 14, Jan. 1976, pp. 57-63.
8. McAlister, K. W.; Carr, L. W.; and McCroskey, W. J.: Dynamic Stall Experiments on the NACA 0012 Airfoils. NASA TP-1100, Jan. 1978.
9. Carta, F.: A Comparison of Pitching and Plunging Response of an Oscillating Airfoil. NASA CR-3172, 1977.
10. St. Hillaire, A. O.; Carta, F. O.: Analysis of Unswept and Swept Wing Chordwise Pressure Data from an Oscillating NACA 0012 Airfoil Experiment. NACA CR-3567, 1983.
11. Chandrasekhara, M. S.; Carr, L. W.: Compressibility Effects on Dynamic Stall of Oscillating Airfoils. AGARD CP-522, Feb. 1993, pp 3.1-3.15.
12. McCroskey, W. J.; McAlister, K. W.; Carr, L. W.; and Pucci, S. L.: An Experimental Study of Dynamic Stall on Advanced Airfoil Sections. vol. 1, Summary of the Experiment; vol. 2, Pressure and Force Data, vol. 3, Hot-Wire and Hot-Film Measurements, NASA TM-84245, Jul. 1982.
13. McAlister, K. W.; and Carr, L. W.: Water-Tunnel Visualization of Dynamic Stall. Nonsteady Fluid Dynamics, Proceedings of the Annual Winter Meeting, ASME, San Francisco, CA, Dec. 1978, pp. 103-11.

14. McCroskey, W. J.: The Phenomenon of Dynamic Stall. NASA TM-81264, 1981.
15. Beddoes, T. S.: A Qualitative Discussion of Dynamic Stall. AGARD Special Course on Unsteady Aerodynamics. AGARD Report 679, 1979.
16. Carr, L. W.: Progress in Analysis and Prediction of Dynamic Stall. J. Aircraft vol. 25, no.1, Jan. 1988, pp. 6-17.
17. Gangwani, S. T.: Synthesized Airfoil Data Method for Prediction of the Dynamic Stall and Unsteady Airloads. AHS 39<sup>th</sup> Annual Forum, St. Louis, Mo, 1984.
18. Leishman, J. G.; and Beddoes, T. S.: A Semi-Empirical Model for Dynamic Stall. J. of the American Helicopter Soc., vol. 24, no.3, Jul. 1989.
19. DeRuyck, J.; Hazarika, B.; and Hirsch, C.: Transition and Turbulence Structure in the Boundary layers of an Oscillating Airfoil. VUB-STR-16, Dept. of Fluid Mechanics, Vrije Universiteit Brussel, Belgium, 1989.
20. Lorber, P. F.; Covino, A. F., Jr.; and Carta, F. O.: Dynamic Stall Experiments on a Swept Three Dimensional Wing in Compressible Flow. AIAA paper 91, 1975.
21. Berton, E.; Favier, D.; and Maresca, C.: Experimental and Numerical Investigations of Dynamic Stall at IRPHE/ASI Laboratory. 24<sup>th</sup> European Rotorcraft Forum, Marseilles, France, Sept. 1998.
22. Rosko, Anatol: Pressure Distribution at the Nose of a Thin Airfoil. Douglas Aircraft Co. Report No. SM-23368, 1958.





Table 1. Importance of Dynamic Stall Parameters

Stall parameter	Effect
Airfoil shape	Large in some cases
Mach number	Small below $M_\infty \sim 0.2$ Large above $M_\infty \sim 0.2$
Reynolds number	Small (?) at low Mach number Unknown at high Mach number
Reduced frequency	Large
Mean angle, amplitude	Large
Type of motion	Virtually unknown
Three-dimensional effects	Virtually unknown
Tunnel effects	Virtually unknown

(Ref. 14)

Table 2. 2-D Test Matrix for the NACA 0015 Wing

	Reduced Frequency			
	0.04	0.1	0.14	0.19
<b>With BL trip:</b>				
Alpha = $4.0 \pm 2.0$ deg	x	x	x	x
Alpha = $9.0 \pm 2.0$ deg	x	x	x	x
Alpha = $11.0 \pm 2.0$ deg	x	x	x	x
Alpha = $13.0 \pm 2.0$ deg	x	x	x	x
Alpha = $15.0 \pm 2.0$ deg	x	x	x	x
Alpha = $17.0 \pm 2.0$ deg	x	x	x	x
Alpha = $4.0 \pm 4.0$ deg	x	x	x	
Alpha = $9.0 \pm 4.0$ deg	x	x	x	
Alpha = $11.0 \pm 4.0$ deg	x	x	x	
Alpha = $13.0 \pm 4.0$ deg	x	x	x	
Alpha = $15.0 \pm 4.0$ deg	x	x	x	
Alpha = $17.0 \pm 4.0$ deg	x	x	x	
Alpha = $13.0 \pm 5.0$ deg	x	x		
Alpha = $17.0 \pm 5.0$ deg	x	x		
<b>Without BL trip:</b>				
Alpha = $4.0 \pm 2.0$ deg	x	x	x	x
Alpha = $9.0 \pm 2.0$ deg	x	x	x	x
Alpha = $11.0 \pm 2.0$ deg	x	x	x	x
Alpha = $13.0 \pm 2.0$ deg	x	x	x	x
Alpha = $15.0 \pm 2.0$ deg	x	x	x	x
Alpha = $17.0 \pm 2.0$ deg	x	x	x	x
Alpha = $1.0 \pm 4.0$ deg	x	x	x	
Alpha = $4.0 \pm 4.0$ deg	x	x	x	
Alpha = $9.0 \pm 4.0$ deg	x	x	x	
Alpha = $11.0 \pm 4.0$ deg	x	x	x	
Alpha = $13.0 \pm 4.0$ deg	x	x	x	
Alpha = $15.0 \pm 4.0$ deg	x	x	x	
Alpha = $17.0 \pm 4.0$ deg	x	x	x	
Alpha = $13.0 \pm 5.0$ deg	x	x		
Alpha = $17.0 \pm 5.0$ deg	x	x		

**Table 3. Classification of 2-D Test Matrix for the NACA 0015 Wing**

	Reduced Frequency			
	0.04	0.1	0.14	0.19
<b>With BL trip:</b>				
Alpha = 4.0 ± 2.0 deg	N	N	N	N
Alpha = 9.0 ± 2.0 deg	N	N	N	N
Alpha = 11.0 ± 2.0 deg	N	N	N	N
Alpha = 13.0 ± 2.0 deg	M	N	N	N
Alpha = 15.0 ± 2.0 deg	M	M	M	M
Alpha = 17.0 ± 2.0 deg	M	M	M	D
Alpha = 4.0 ± 4.0 deg	N	N	N	
Alpha = 9.0 ± 4.0 deg	N	N	N	
Alpha = 11.0 ± 4.0 deg	M	N	N	
Alpha = 13.0 ± 4.0 deg	M	M	M	
Alpha = 15.0 ± 4.0 deg	M	D	D	
Alpha = 17.0 ± 4.0 deg	M	D	D	
Alpha = 13.0 ± 5.0 deg	D	D		
Alpha = 17.0 ± 5.0 deg	D	D		
<b>Without BL trip:</b>				
Alpha = 4.0 ± 2.0 deg	N	N	N	N
Alpha = 9.0 ± 2.0 deg	N	N	N	N
Alpha = 11.0 ± 2.0 deg	N	N	N	N
Alpha = 13.0 ± 2.0 deg	M	M	N	N
Alpha = 15.0 ± 2.0 deg	M	M	M	M
Alpha = 17.0 ± 2.0 deg	M	M	M	M
Alpha = 1.0 ± 4.0 deg	N	N	N	
Alpha = 4.0 ± 4.0 deg	N	N	N	
Alpha = 9.0 ± 4.0 deg	N	N	N	
Alpha = 11.0 ± 4.0 deg	M	N	N	
Alpha = 13.0 ± 4.0 deg	M	M	M	
Alpha = 15.0 ± 4.0 deg	M	D	D	
Alpha = 17.0 ± 4.0 deg	M	D	D	
Alpha = 13.0 ± 5.0 deg	D	D		
Alpha = 17.0 ± 5.0 deg	M	D		
<b>N = No stall case</b> <b>M = Moderate stall (light stall) case</b> <b>D = Deep stall case</b>				

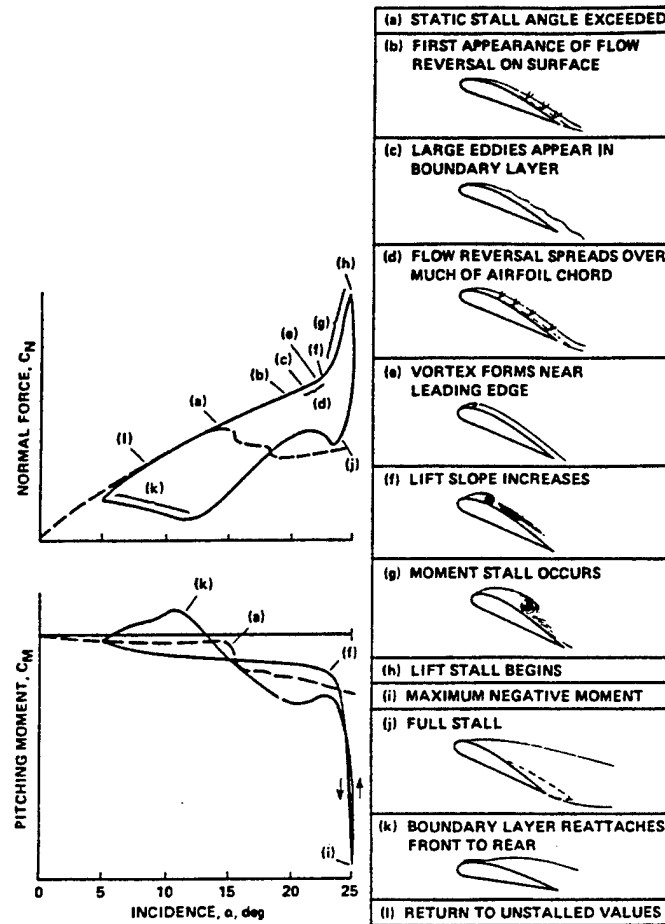


Fig.1. Development of dynamic stall on an oscillating Airfoil at  $Re = 2 \times 10^6$ ,  $M_\infty = 0.09$  (Ref. 1)

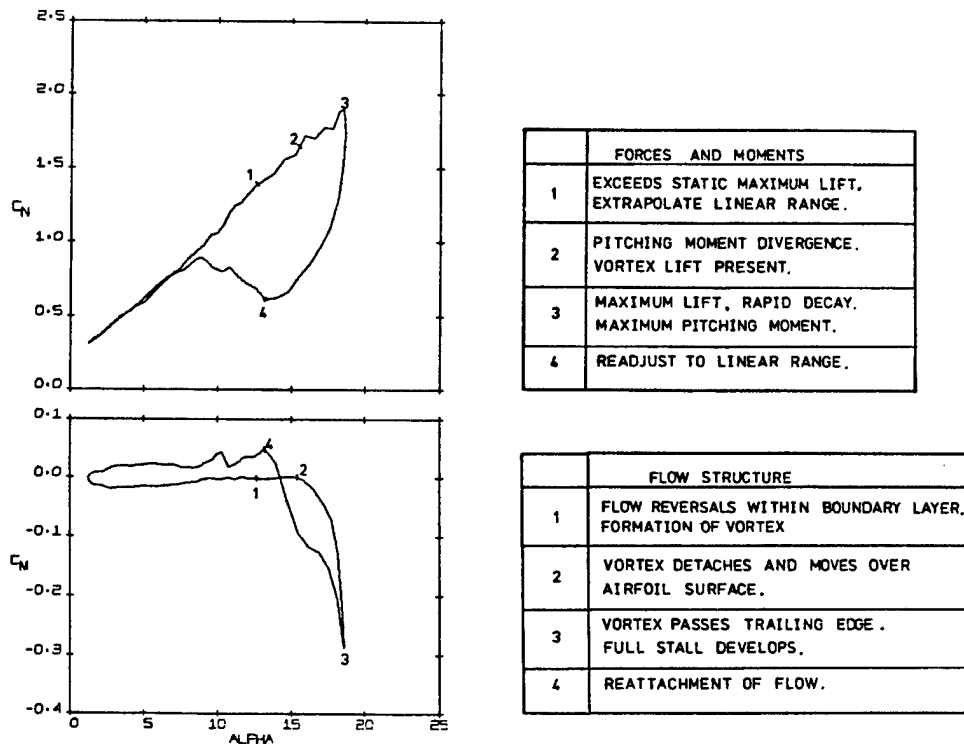


Fig. 2. Dynamic stall events (ref. 15)

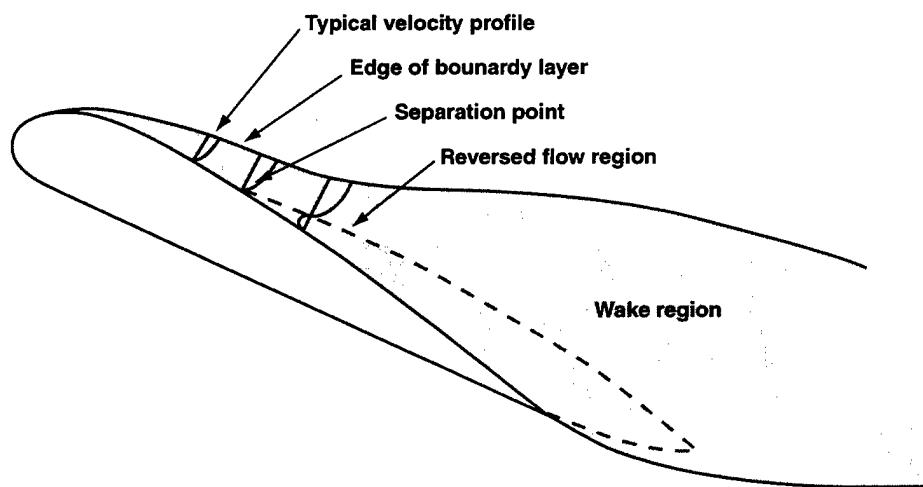


Fig. 3. Steady separation on an airfoil (*Ref. 2*)

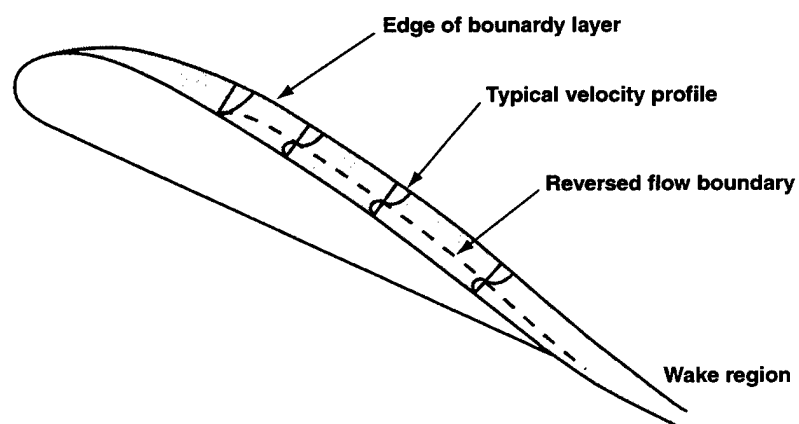
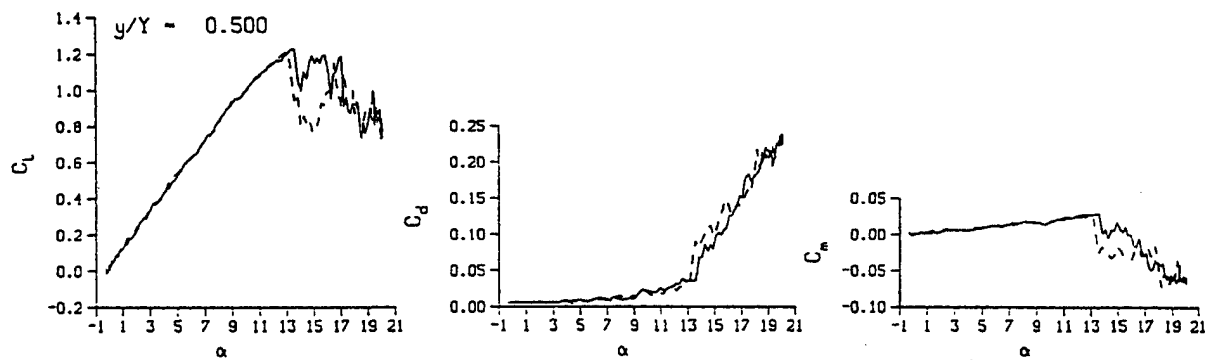


Fig. 4. Unsteady flow reversal on an oscillation airfoil (*Ref. 2*)



DataPointID: 2dqstl.r0885

$\alpha = 10.27 = 10.15$  Deg.

$\nu = 0.000$

Fig. 5. NACA 0015 Airfoil, Quasi-steady data (ref. 1)

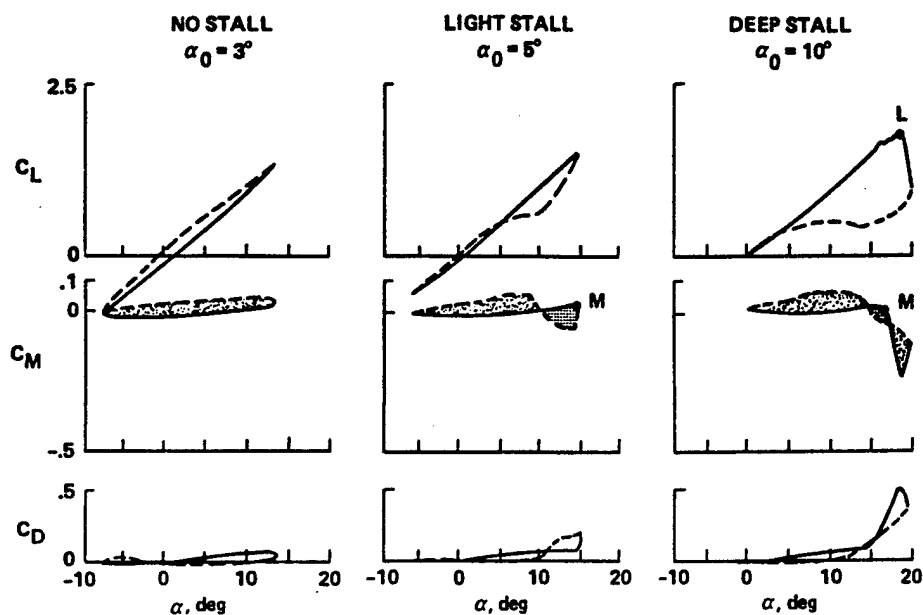


Fig. 6. Dynamic stall regimes, NACA 0012 Airfoil,  $\alpha = \alpha_0 + 10^\circ \sin \omega t$ ,  $k = 0.10$ ; solid lines denote increasing  $\alpha$ , dashed lines decreasing  $\alpha$ . (ref. 14)

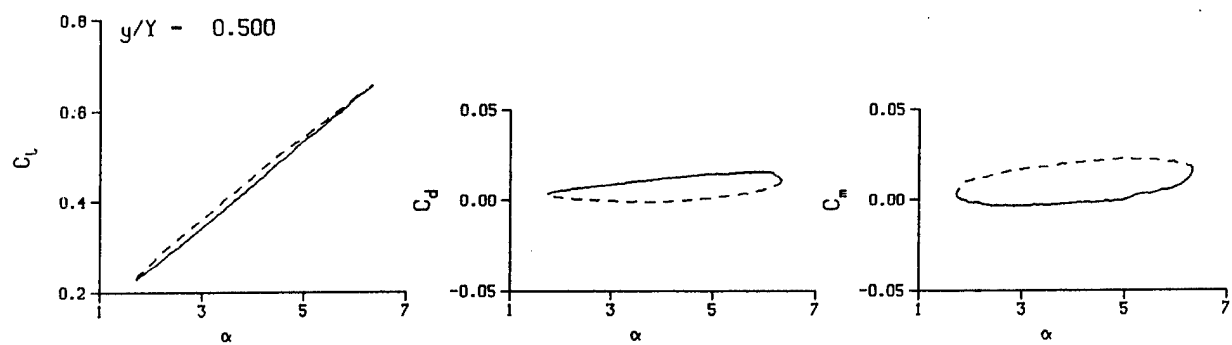


Fig. 7a

DataPointID: 2DPOT1.R0763

$$\alpha = 4.06 \pm 2.30 \text{ Deg.}$$

$$\nu = 0.188$$

*note: different y-axis scale*

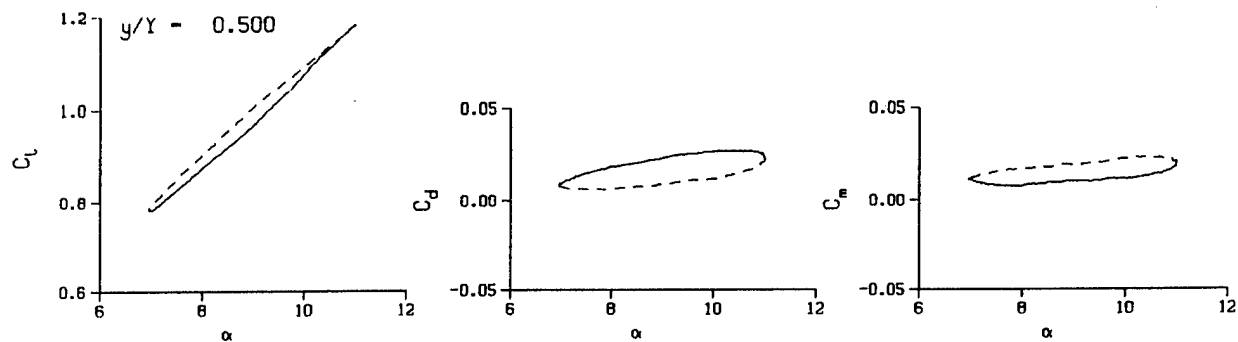


Fig. 7b

DataPointID: 2DPOT1.R0766

$$\alpha = 8.97 \pm 2.04 \text{ Deg.}$$

$$\nu = 0.094$$

*note: different y-axis scale*

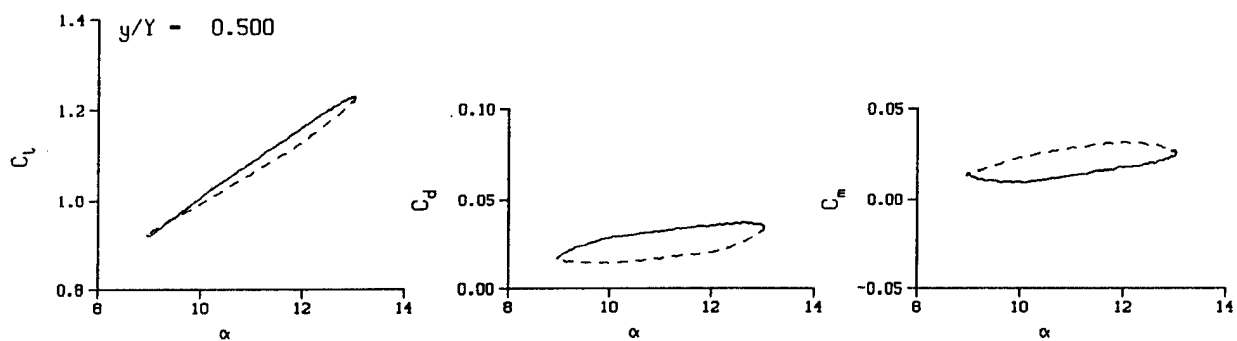


Fig. 7c

DataPointID: 2DPOT1.R0750

$$\alpha = 10.99 \pm 2.04 \text{ Deg.}$$

$$\nu = 0.095$$

*note: different y-axis scale*

Fig. 7. Lift, drag and pitching moment for the No stall case with an amplitude of 2 degrees at different mean angles (ref. 1)

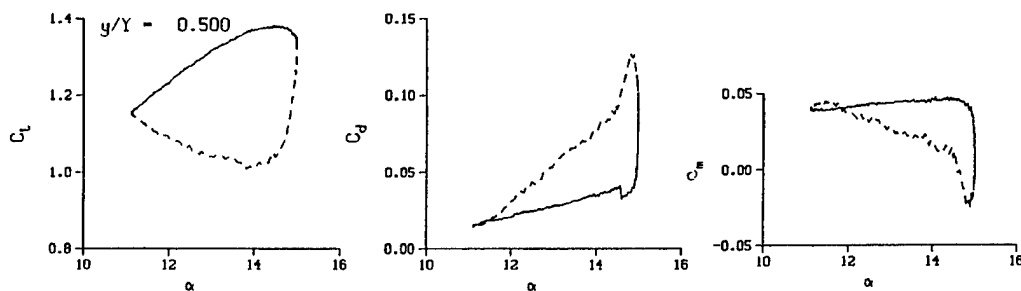


**Fig.8a**

DataPointID: 2DP0T1.R0770

$\alpha = 13.07 \pm 1.97$  Deg.

$\nu = 0.038$

*note: different y-axis scale*

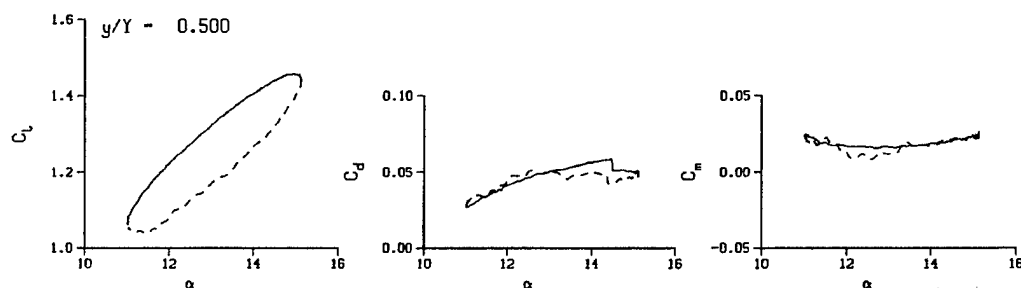


**Fig.8b**

DataPointID: 2DP0T1.R0772

$\alpha = 13.08 \pm 2.13$  Deg.

$\nu = 0.133$

**Fig. 8.** Lift, drag and pitching moment for the case of  $13 \pm 2$  deg at different reduced frequencies (*ref. 1*)

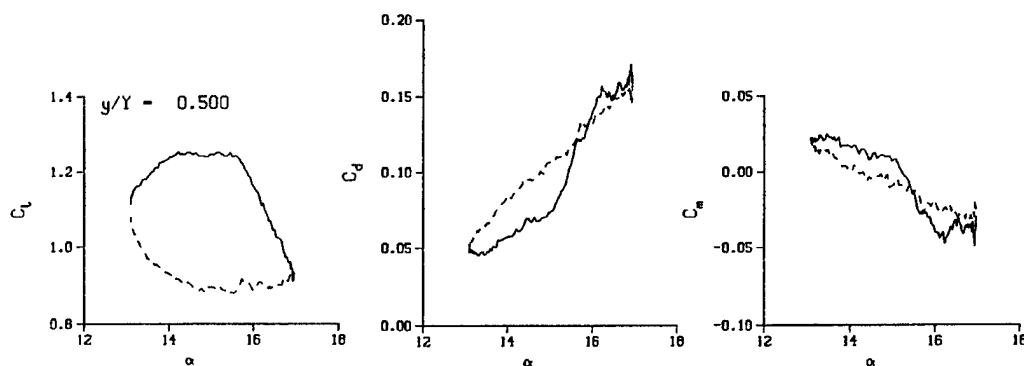


**Fig.9a**

DataPointID: 2DP0T1.R0775

$\alpha = 15.03 \pm 1.95$  Deg.

$\nu = 0.038$

*note: different y-axis scale*

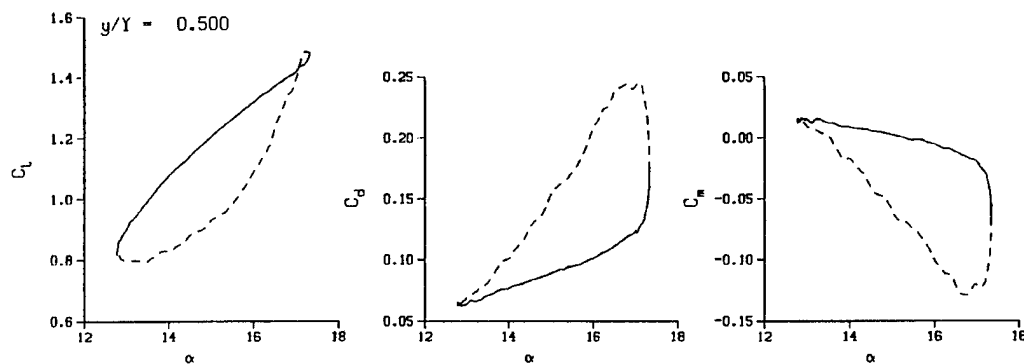


**Fig.9b**

DataPointID: 2DP0T1.R0778

$\alpha = 15.03 \pm 2.28$  Deg.

$\nu = 0.190$

**Fig. 9.** Lift, drag and pitching moment for the case of  $15 \pm 2$  deg at different reduced frequencies (*ref. 1*)



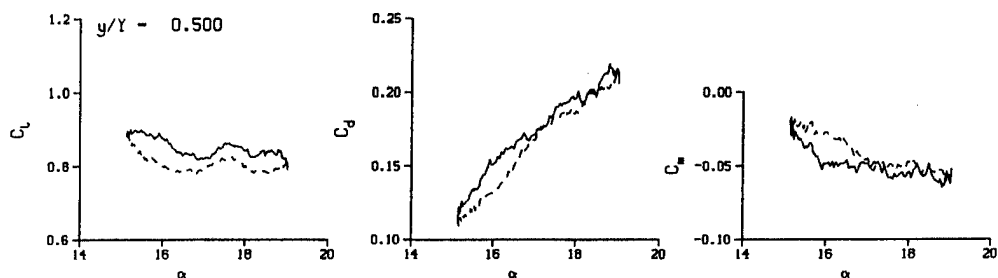


**Fig. 10a**

DataPointID: 2DP0T1.R0780

$$\alpha = 17.09 \pm 1.97 \text{ Deg.}$$

$$\nu = 0.038$$

*note: different y-axis scale*

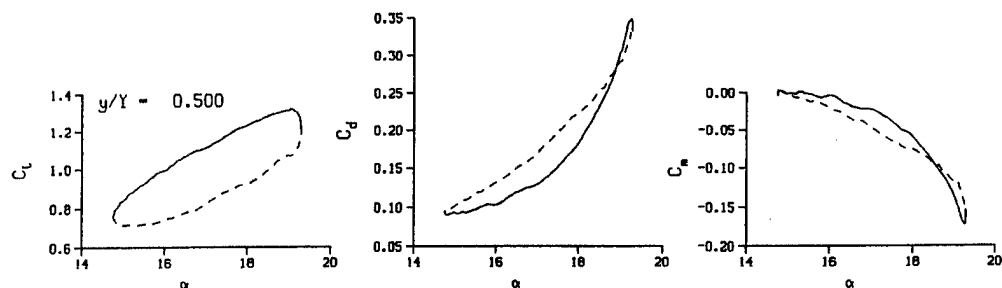


**Fig. 10b**

DataPointID: 2DP0T1.R0783

$$\alpha = 17.09 \pm 2.26 \text{ Deg.}$$

$$\nu = 0.191$$

**Fig. 10. Lift, drag and pitching moment for the case of  $17 \pm 2$  deg at different reduced frequencies (ref. 1)**

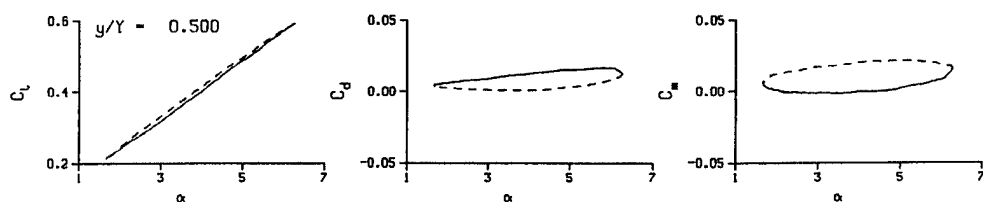


**Fig. 11a**

DataPointID: 2DP0TN.R0631

$$\alpha = 3.99 \pm 2.31 \text{ Deg.}$$

$$\nu = 0.190$$

*note: different y-axis scale*

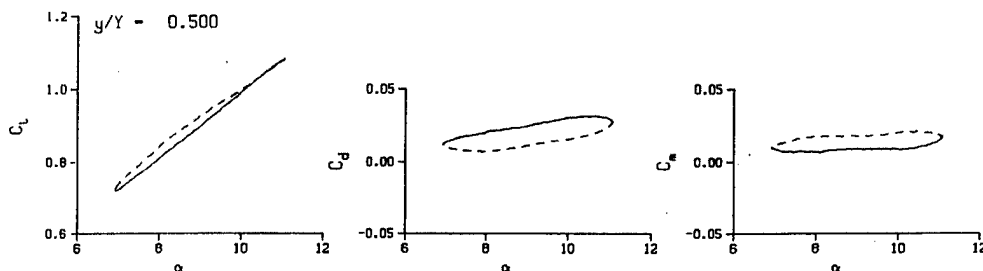


**Fig. 11b**

DataPointID: 2DP0TN.R0634

$$\alpha = 8.99 \pm 2.08 \text{ Deg.}$$

$$\nu = 0.096$$

*note: different y-axis scale*

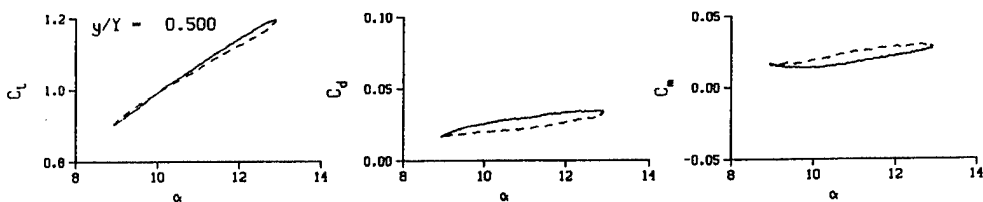


**Fig. 11c**

DataPointID: 2DP0TN.R0638

$$\alpha = 10.92 \pm 2.01 \text{ Deg.}$$

$$\nu = 0.038$$

**Fig. 11. Lift, drag and pitching moment for the no-boundary layer (BL) trip case with an amplitude of 2 deg at different mean angles (ref. 1)**

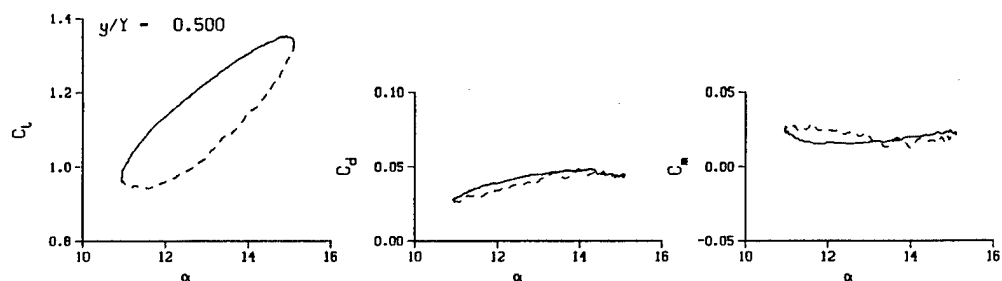
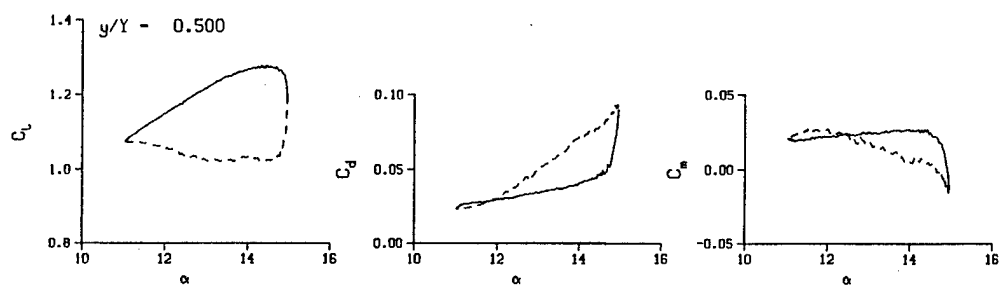
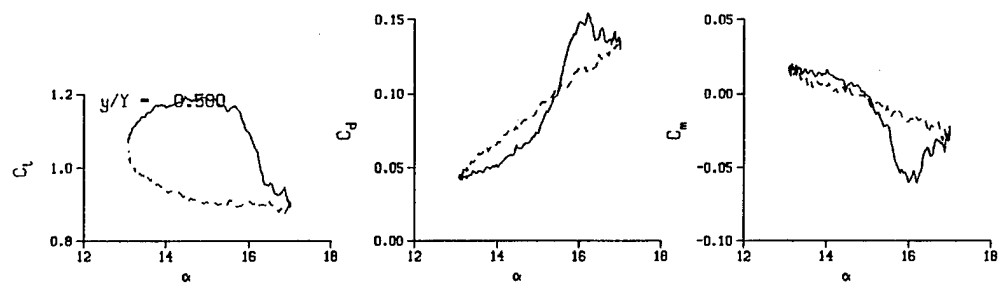


Fig. 12. Lift, drag and pitching moment for the no-BL trip case of  $13 \pm 2$  at different reduced frequencies (*ref. 1*)



*note: different y-axis scale*

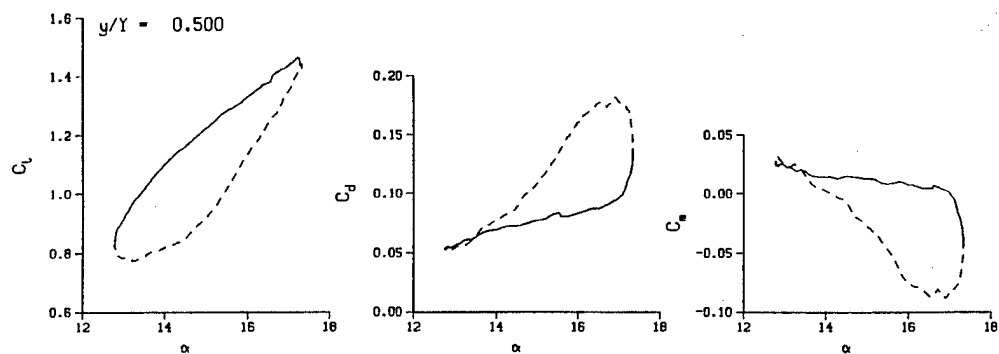
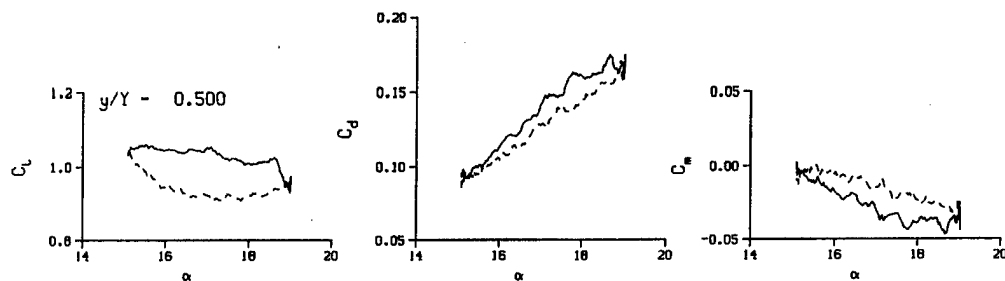


Fig. 13. Lift, drag and pitching moment for the no-BL case of  $15 \pm 2$  at different reduced frequencies (*ref. 1*)



**Fig.14a**

DataPointID: 2DP0TN.R0653

$\alpha = 17.06 \pm 1.99$  Deg.

$\nu = 0.038$

*note: different y-axis scale*

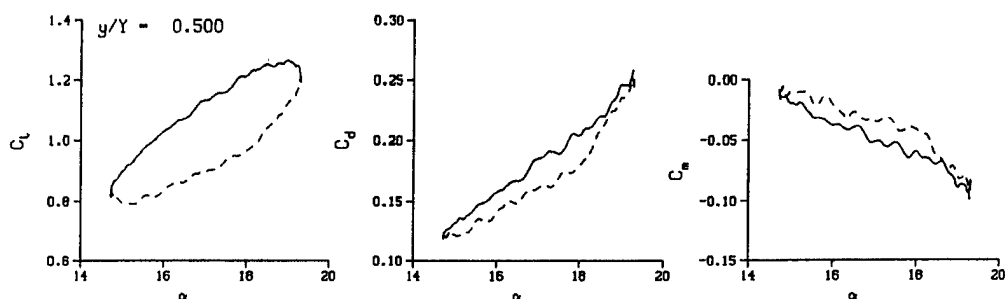


**Fig.14b**

DataPointID: 2DP0TN.R0656

$\alpha = 17.05 \pm 2.29$  Deg.

$\nu = 0.190$

**Fig. 14.** Lift, drag and pitching moment for the no-BL trip case of  $17 \pm 2$  deg at different reduced frequencies (*ref. 1*)

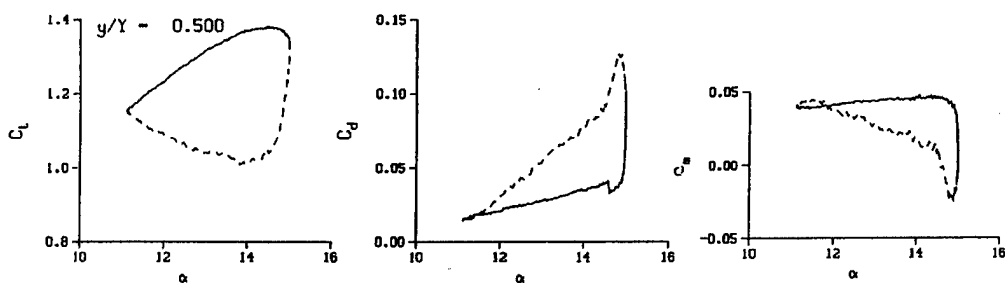


**Fig.15a BL Trip**

DataPointID: 2DP0T1.R0770

$\alpha = 13.07 \pm 1.97$  Deg.

$\nu = 0.038$

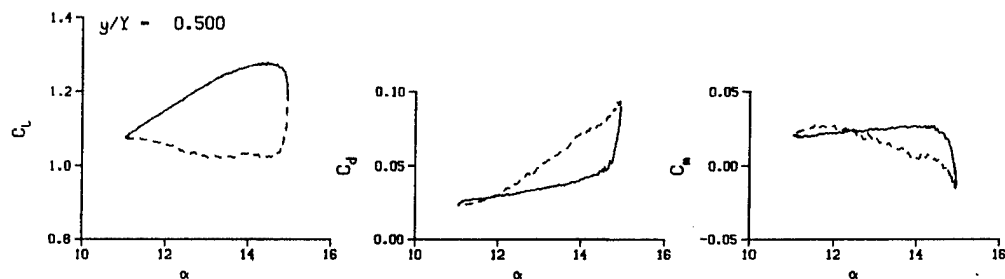


**Fig.15b No BL Trip**

DataPointID: 2DP0TN.R0643

$\alpha = 13.01 \pm 1.99$  Deg.

$\nu = 0.038$

**Fig. 15.** Lift, drag and pitching moment for BL trip vs. No-BL trip case of  $13 \pm 2$  deg, reduced frequency of 0.04 (*ref. 1*)

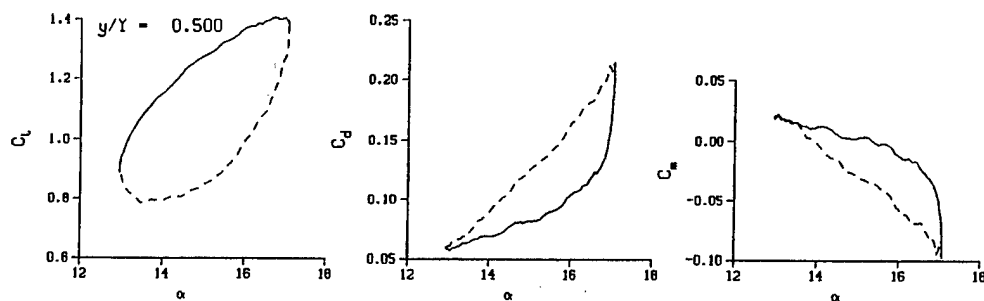


**Fig.16a BL Trip**  
 DataPointID: 2DPOT1.R0777  
 $\alpha = 15.04 \pm 2.11$  Deg.  
 $\nu = 0.133$

*note: different y-axis scale*

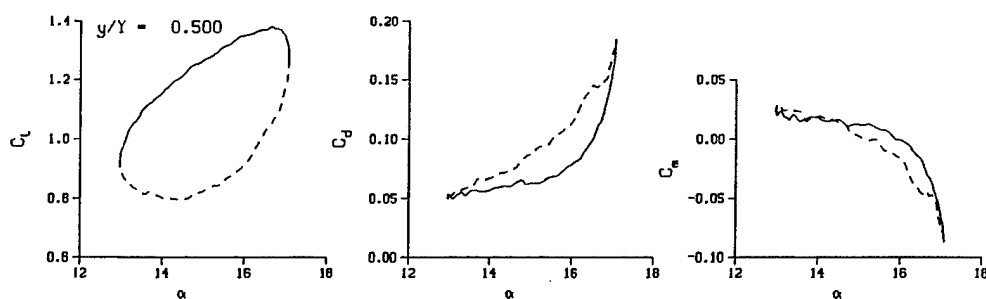


**Fig.16b No BL Trip**  
 DataPointID: 2DPOTN.R0650  
 $\alpha = 15.05 \pm 2.11$  Deg.  
 $\nu = 0.132$

**Fig. 16. Lift, drag and pitching moments for BL trip vs. No-BL trip in the case of  $15 \pm 2$  deg at a reduced frequency of 0.14 (ref. 1)**

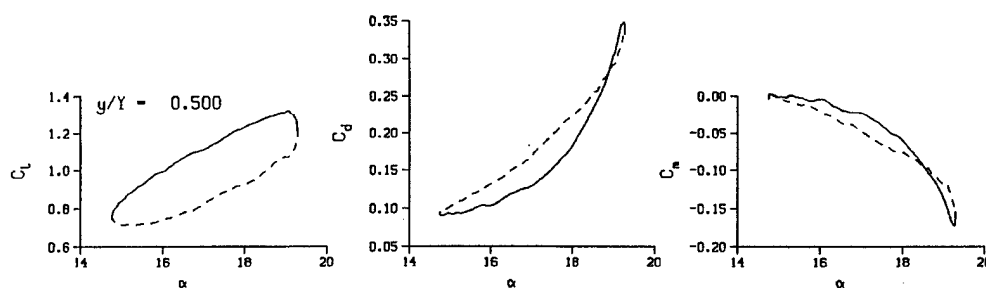


**Fig.17a BL Trip**  
 DataPointID: 2DPOT1.R0783  
 $\alpha = 17.09 \pm 2.26$  Deg.  
 $\nu = 0.191$

*note: different y-axis scale*

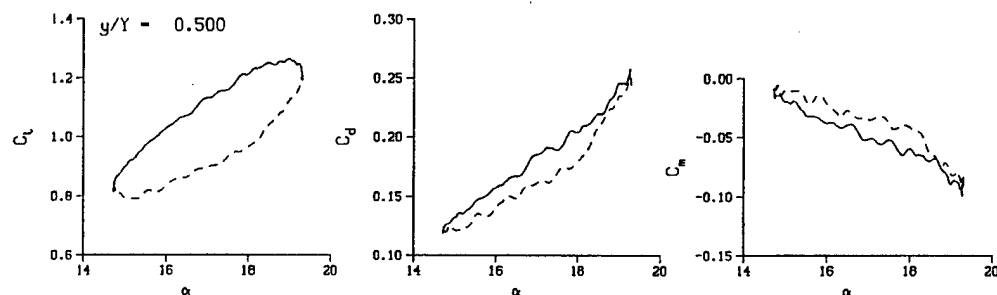


**Fig.17b No BL Trip**  
 DataPointID: 2DPOTN.R0656  
 $\alpha = 17.05 \pm 2.29$  Deg.  
 $\nu = 0.190$

**Fig. 17. Lift, drag and pitching moment for BL trip vs. No-BL trip in the case of  $17 \pm 2$  deg at a reduced frequency of 0.19 (ref. 1)**

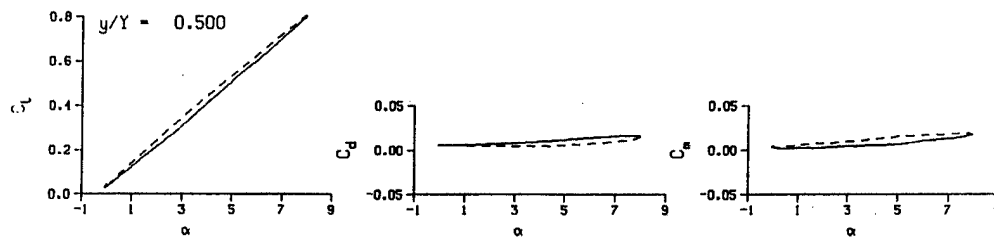


Fig. 18a

DataPointID: 2DPOT1.R0789

$\alpha = 3.99 \pm 4.04$  Deg.

$\nu = 0.038$

note: different y-axis scale

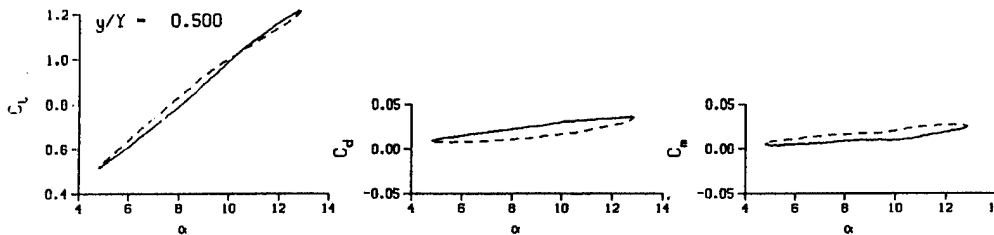


Fig. 18b

DataPointID: 2DPOT1.R0793

$\alpha = 8.86 \pm 4.05$  Deg.

$\nu = 0.038$

Fig. 18. Lift, drag and pitching moment for the No stall case with an amplitude of 4 deg at different mean angles (ref. 1)

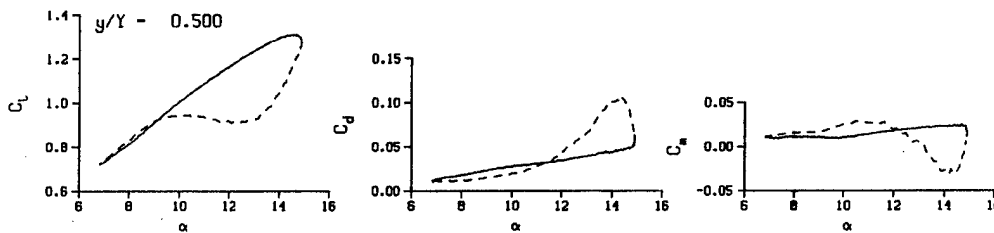


Fig. 19a

DataPointID: 2DPOT1.R0797

$\alpha = 10.88 \pm 4.07$  Deg.

$\nu = 0.038$

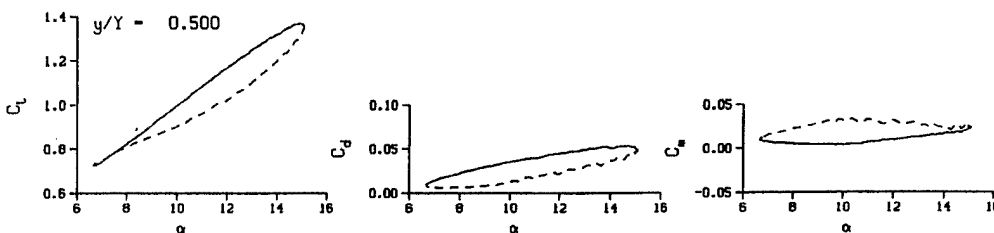


Fig. 19b

DataPointID: 2DPOT1.R0798

$\alpha = 10.88 \pm 4.22$  Deg.

$\nu = 0.095$

Fig. 19. Lift, drag and pitching moment for the case of  $11 \pm 4$  deg at different reduced frequencies (ref. 1)

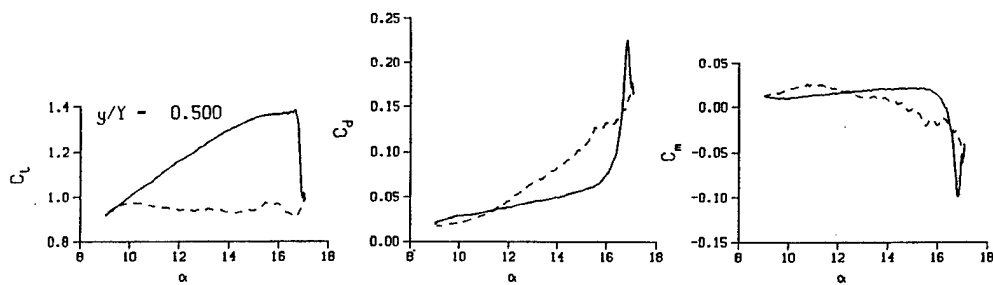


**Fig. 20a**

DataPointID: 2DPOT1.R0801

$\alpha = 13.06 \pm 4.04$  Deg.

$\nu = 0.038$

*note: different y-axis scale*

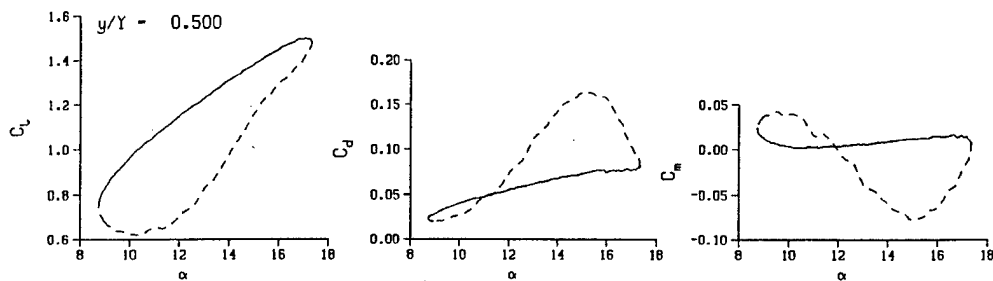


**Fig. 20b**

DataPointID: 2DPOT1.R0803

$\alpha = 13.07 \pm 4.35$  Deg.

$\nu = 0.134$

**Fig. 20. Lift, drag and pitching moment for the case of  $13 \pm 4$  deg at different reduced frequencies (ref. 1)**

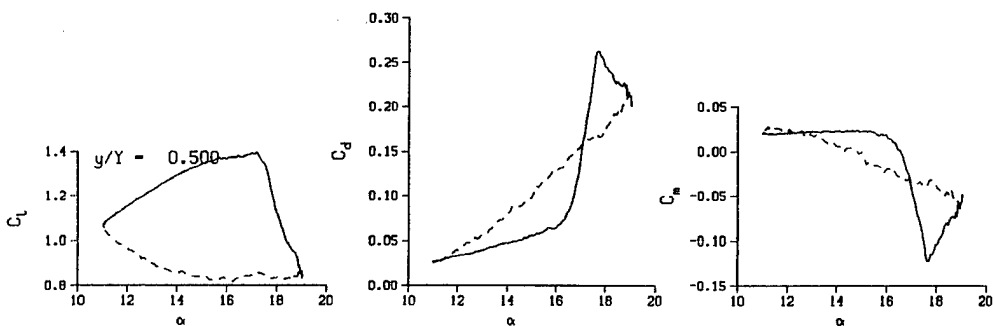


**Fig. 21a**

DataPointID: 2DPOT1.R0805

$\alpha = 15.04 \pm 4.04$  Deg.

$\nu = 0.038$

*note: different y-axis scale*

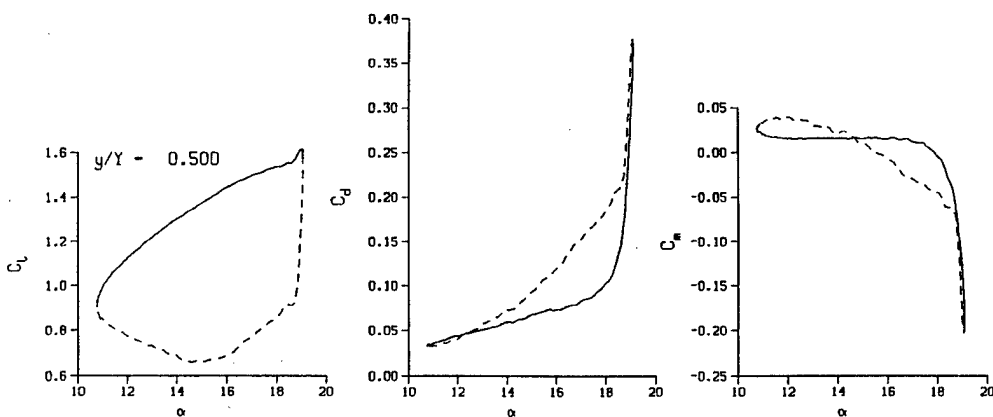


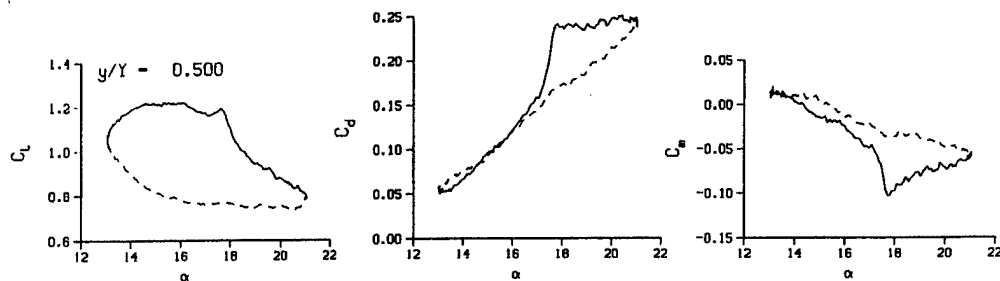
**Fig. 21b**

DataPointID: 2DPOT1.R0806

$\alpha = 15.04 \pm 4.16$  Deg.

$\nu = 0.096$

**Fig. 21. Lift, drag and pitching moment for the case of  $15 \pm 4$  deg at different reduced frequencies (ref. 1)**



*note: different y-axis scale*

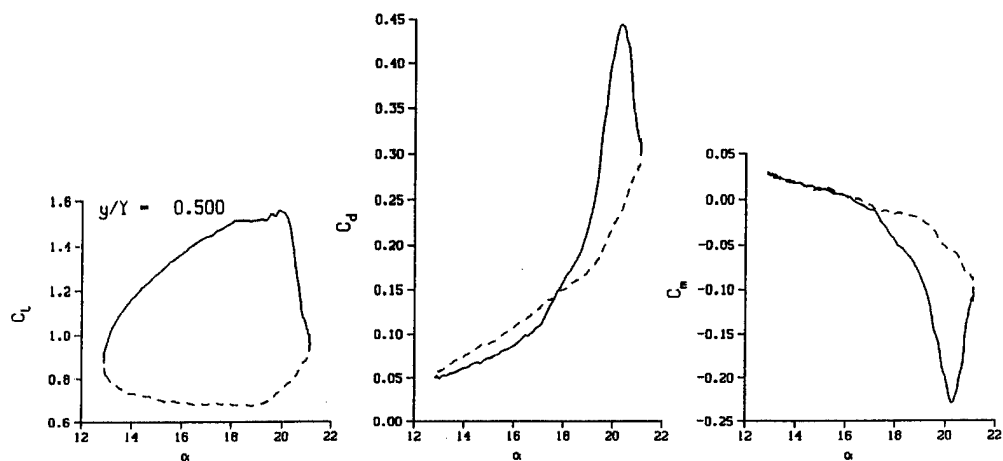


**Fig. 22.** Lift, drag and pitching moment for the case of  $17 \pm 4$  deg at different reduced frequencies (*ref. 1*)

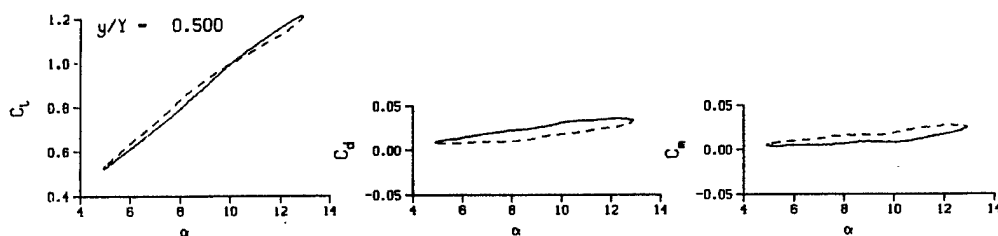
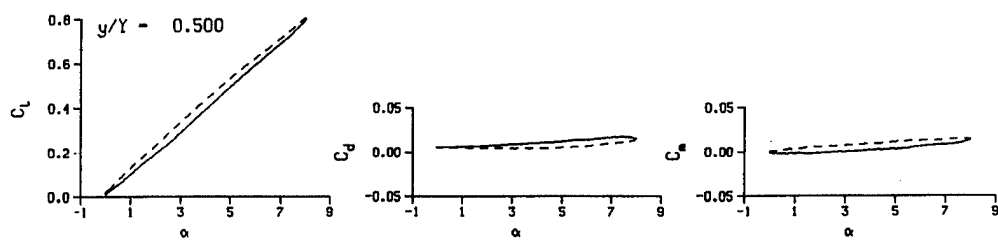


**Fig. 23.** Lift, drag and pitching moment for the no-BL trip case with an amplitude of 2 deg at different mean angles (*ref. 1*)

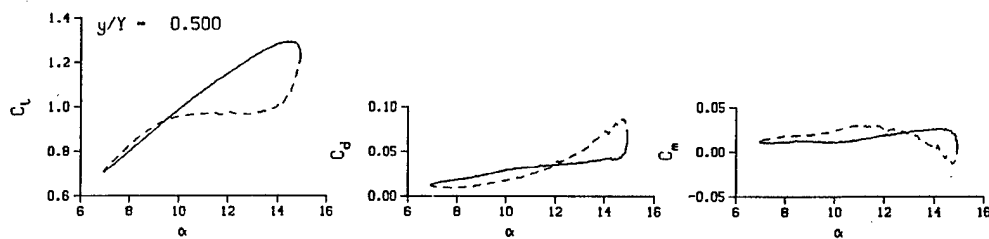


**Fig. 24a**

DataPointID: 2DPOTN.R0670

$$\alpha = 10.95 \pm 4.04 \text{ Deg.}$$

$$\nu = 0.038$$

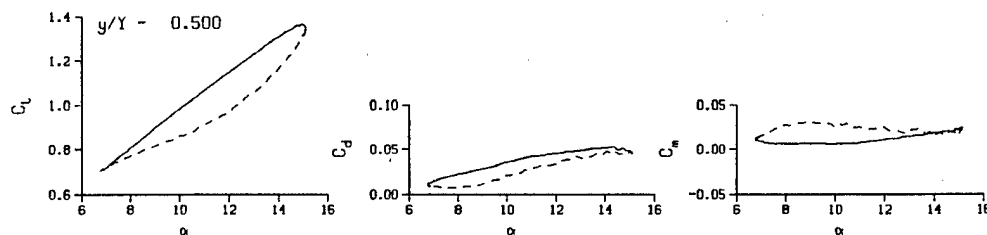


**Fig. 24b**

DataPointID: 2DPOTN.R0671

$$\alpha = 10.94 \pm 4.18 \text{ Deg.}$$

$$\nu = 0.095$$

**Fig. 24.** Lift, drag and pitching moment for the no-BL trip case of  $11 \pm 4$  deg at different reduced frequencies (*ref. 1*)

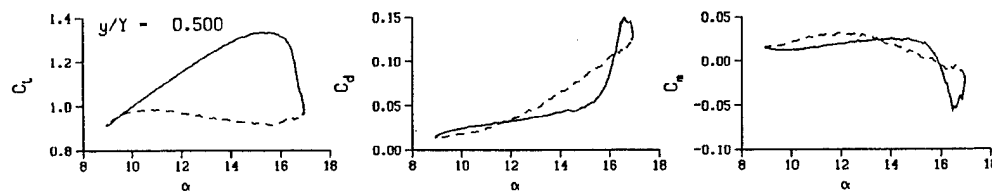


**Fig. 25a**

DataPointID: 2DPOTN.R0674

$$\alpha = 12.96 \pm 4.04 \text{ Deg.}$$

$$\nu = 0.038$$

*note: different y-axis scale*

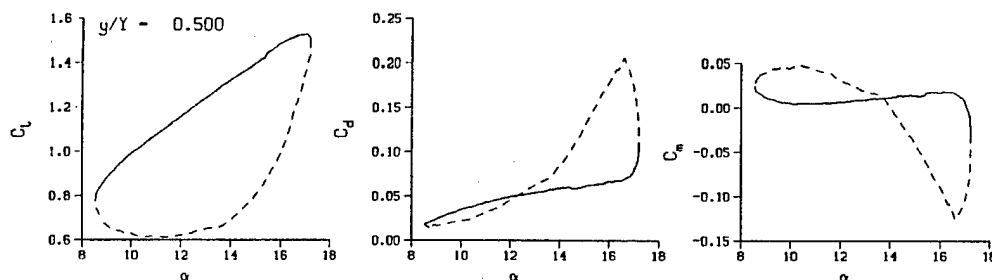


**Fig. 25b**

DataPointID: 2DPOTN.R0676

$$\alpha = 12.93 \pm 4.34 \text{ Deg.}$$

$$\nu = 0.132$$

**Fig. 25.** Lift, drag and pitching moment for the no-BL trip case of  $13 \pm 4$  deg at different reduced frequencies (*ref. 1*)



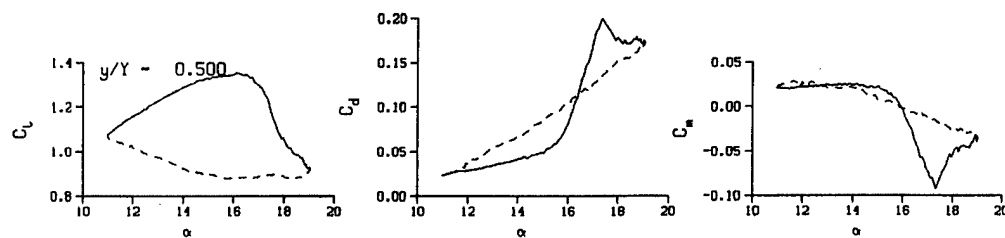


**Fig. 26a**

DataPointID: 2DP0TN.R0678

$\alpha = 15.04 \pm 4.06$  Deg.

$\nu = 0.038$

*note: different y-axis scale*

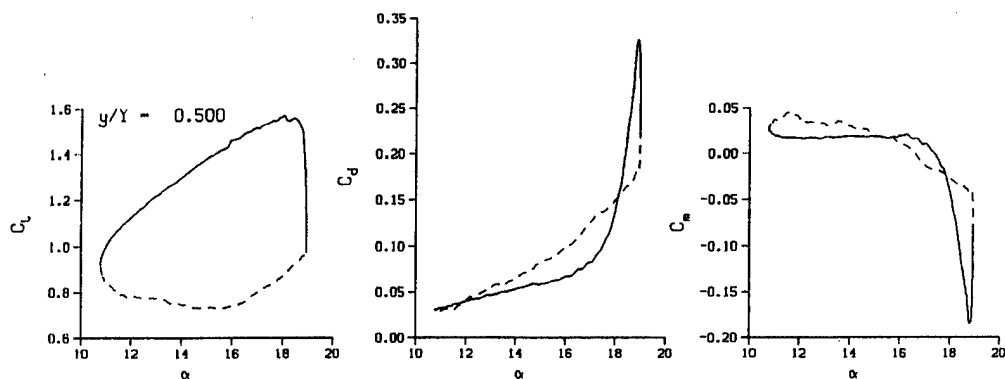


**Fig. 26b**

DataPointID: 2DP0TN.R0679

$\alpha = 15.02 \pm 4.17$  Deg.

$\nu = 0.095$

**Fig. 26.** Lift, drag and pitching moment for the no-BL trip case of  $15 \pm 4$  deg at different reduced frequencies (*ref. 1*)

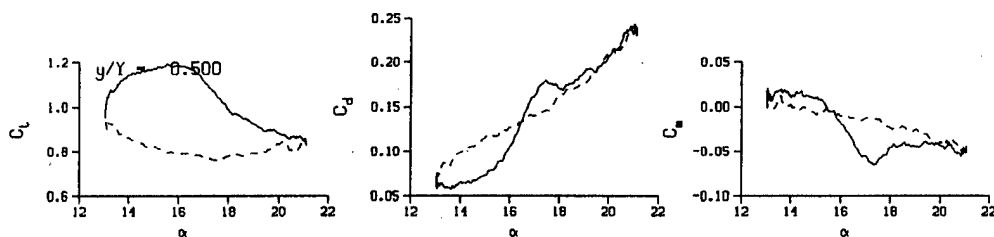


**Fig. 27a**

DataPointID: 2DP0TN.R0682

$\alpha = 17.10 \pm 4.06$  Deg.

$\nu = 0.038$

*note: different y-axis scale*

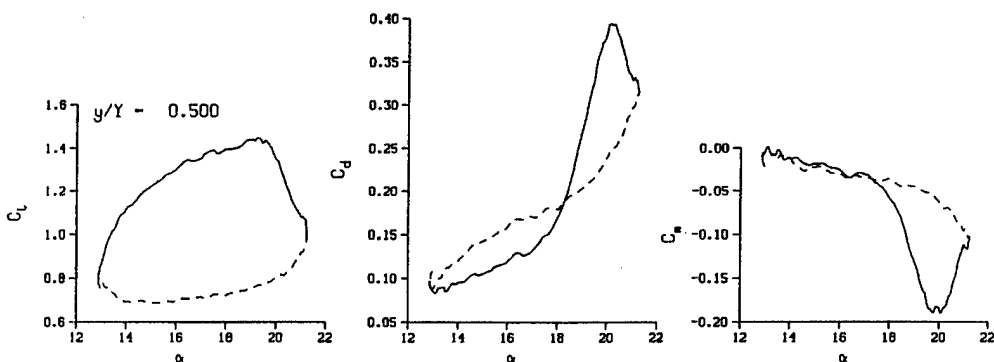


**Fig. 27b**

DataPointID: 2DP0TN.R0683

$\alpha = 17.09 \pm 4.17$  Deg.

$\nu = 0.096$

**Fig. 27.** Lift, drag and pitching moment for the no-BL trip case of  $17 \pm 4$  deg at different reduced frequencies (*ref. 1*)

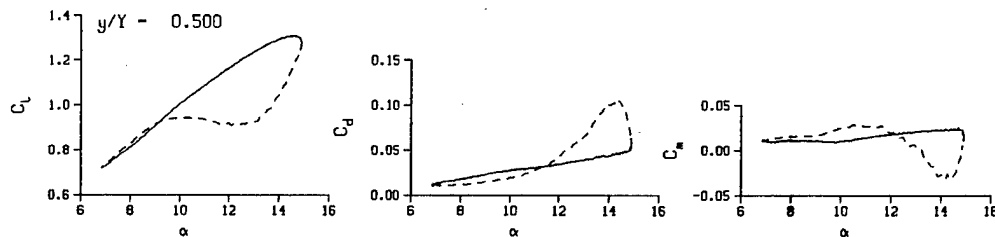


**Fig.28a BL Trip**

DataPointID: 2DPOT1.R0797

$$\alpha = 10.88 \pm 4.07 \text{ Deg.}$$

$$\nu = 0.038$$

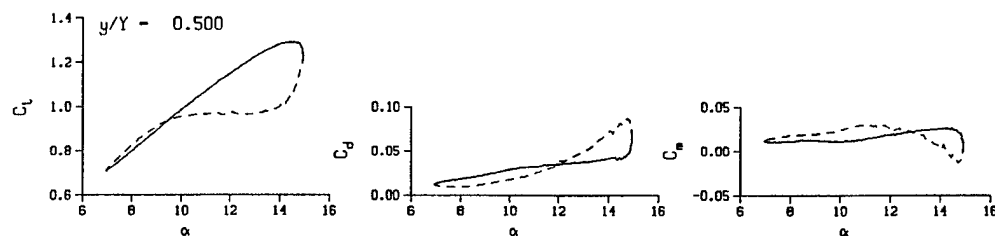


**Fig.28b No BL Trip**

DataPointID: 2DPOTN.R0670

$$\alpha = 10.95 \pm 4.04 \text{ Deg.}$$

$$\nu = 0.038$$

**Fig. 28. Lift, drag and pitching moment for BL trip vs. No-BL trip of  $11 \pm 4$  deg at a reduced frequency of 0.04 (ref. 1)**

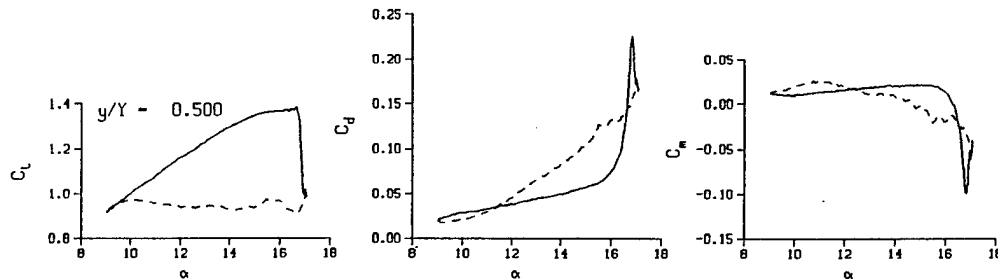


**Fig.29a BL Trip**

DataPointID: 2DPOT1.R0801

$$\alpha = 13.06 \pm 4.04 \text{ Deg.}$$

$$\nu = 0.038$$

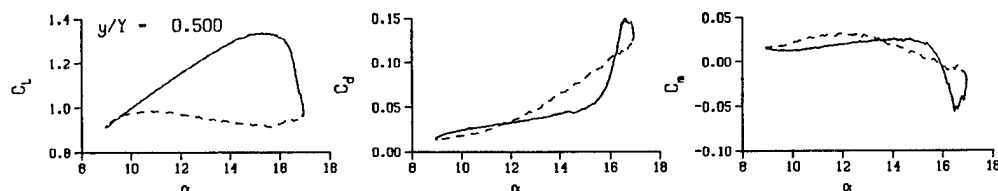


**Fig.29b No BL Trip**

DataPointID: 2DPOTN.R0674

$$\alpha = 12.96 \pm 4.04 \text{ Deg.}$$

$$\nu = 0.038$$

**Fig. 29. Lift, drag and pitching moment for BL trip vs. No-BL trip for  $13 \pm 4$  deg at a reduced frequency of 0.04 (ref. 1)**

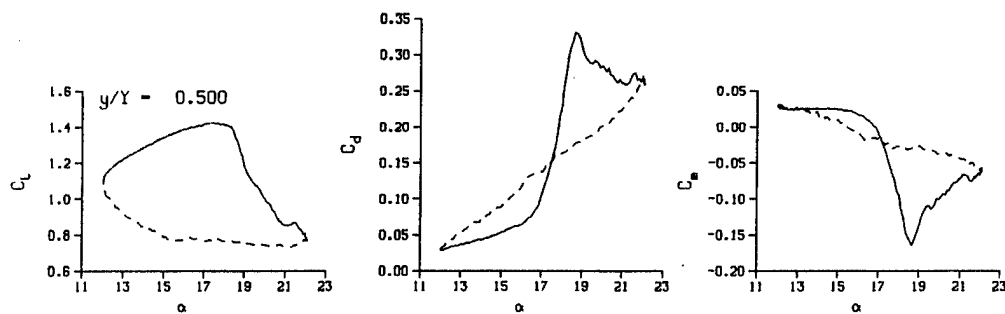
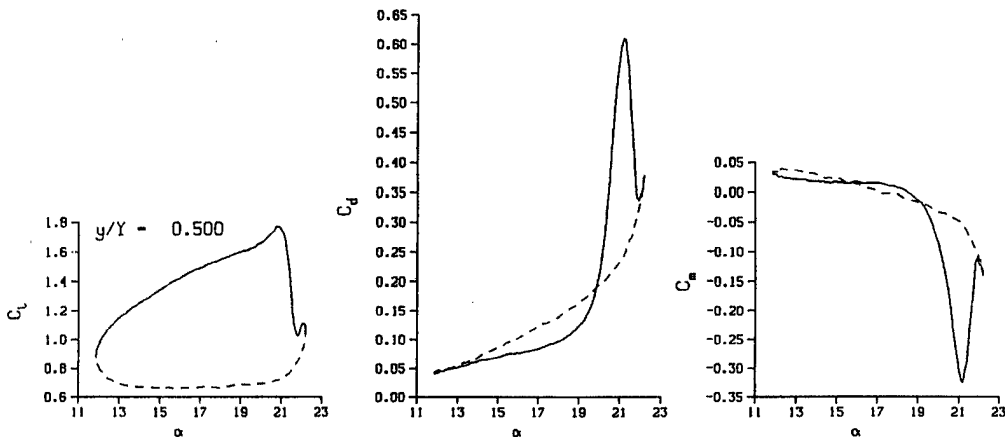


**Fig. 30a**

DataPointID: 2DPOT1.R0813

$\alpha = 17.09 \pm 5.07$  Deg.

$\nu = 0.038$



*note: different y-axis scale*

**Fig. 30b**

DataPointID: 2DPOT1.R0814

$\alpha = 17.08 \pm 5.18$  Deg.

$\nu = 0.095$

**Fig. 30. Lift, drag and pitching moment for the case of  $17 \pm 5$  deg at different reduced frequencies (ref. 1)**

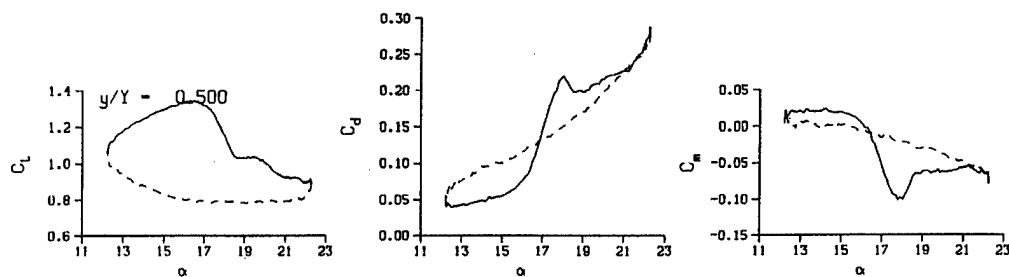
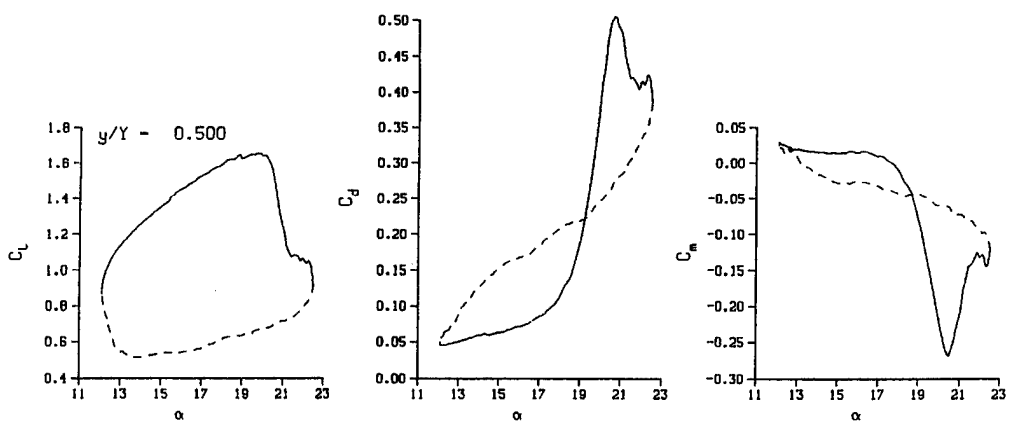


**Fig. 31a**

DataPointID: 2DPOTN.R0689

$\alpha = 17.27 \pm 5.05$  Deg.

$\nu = 0.038$



*note: different y-axis scale*

**Fig. 31b**

DataPointID: 2DPOTN.R0690

$\alpha = 17.26 \pm 5.17$  Deg.

$\nu = 0.095$

**Fig. 31. Lift, drag and pitching moment for the no-BL trip case of  $17 \pm 5$  deg at different reduced frequencies (ref. 1)**

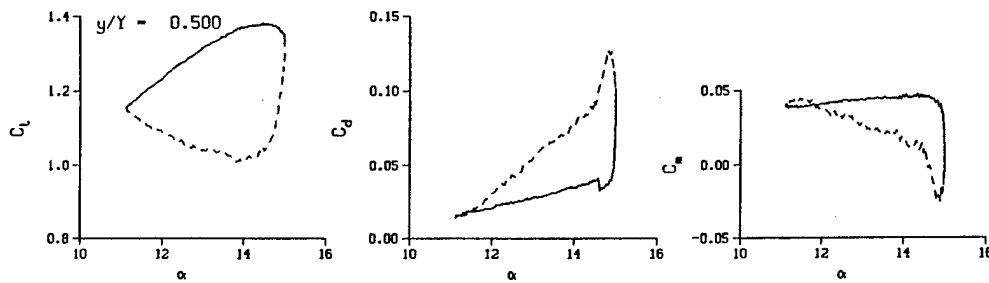


**Fig. 32a**

DataPointID: 2DPOT1.R0770

$$\alpha = 13.07 \pm 1.97 \text{ Deg.}$$

$$\nu = 0.038$$

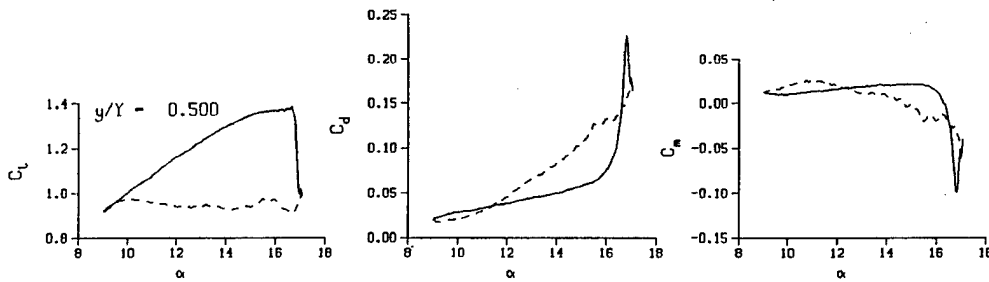


**Fig. 32b**

DataPointID: 2DPOT1.R0801

$$\alpha = 13.06 \pm 4.04 \text{ Deg.}$$

$$\nu = 0.038$$

**Fig. 32. Lift, drag and pitching moment for the mean angle of 13 deg at different amplitudes (ref. 1)**

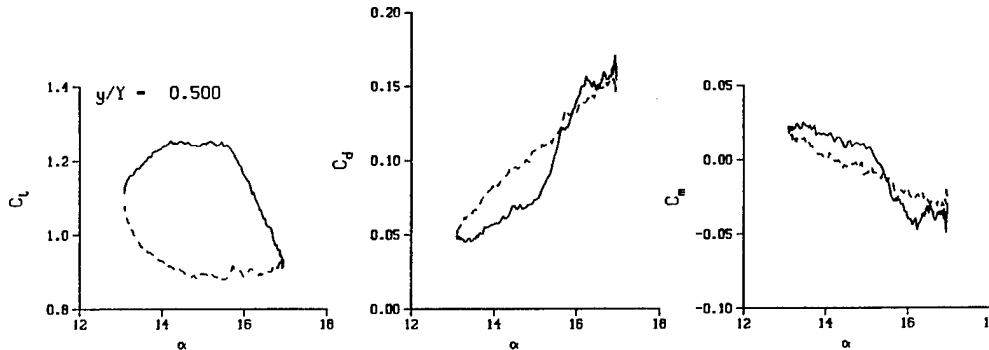


**Fig. 33a**

DataPointID: 2DPOT1.R0775

$$\alpha = 15.03 \pm 1.95 \text{ Deg.}$$

$$\nu = 0.038$$

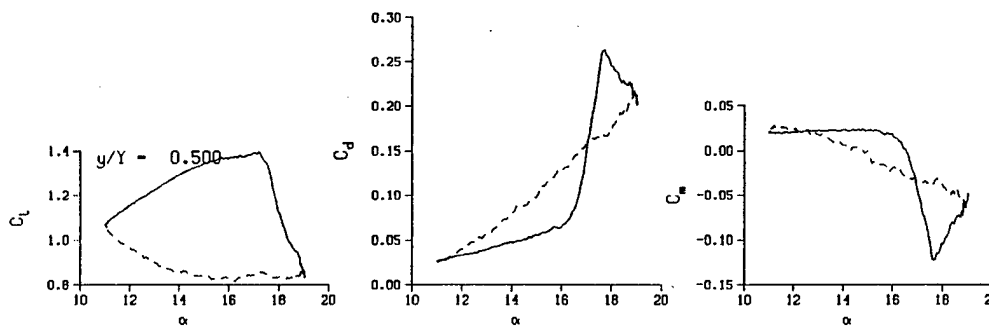


**Fig. 33b**

DataPointID: 2DPOT1.R0805

$$\alpha = 15.04 \pm 4.04 \text{ Deg.}$$

$$\nu = 0.038$$

**Fig. 33. Lift, drag and pitching moment for the case of mean angle of 15 deg at different amplitudes (ref. 1)**

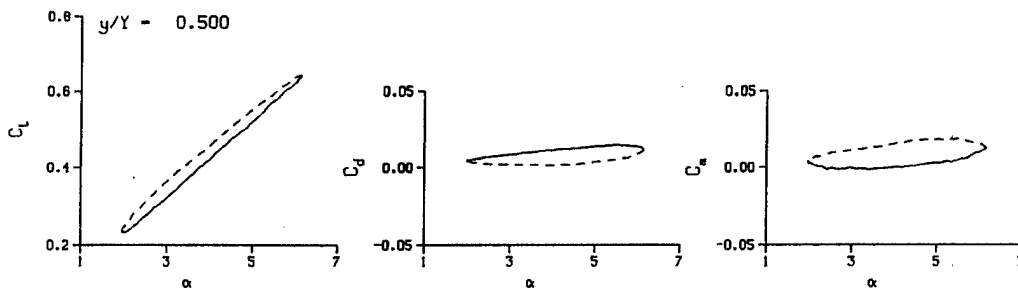
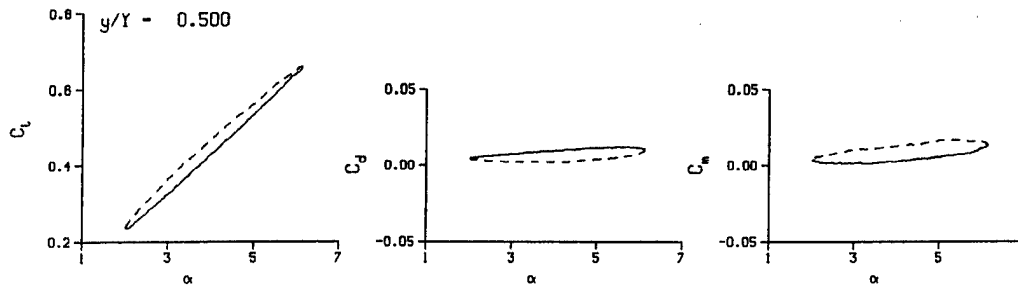
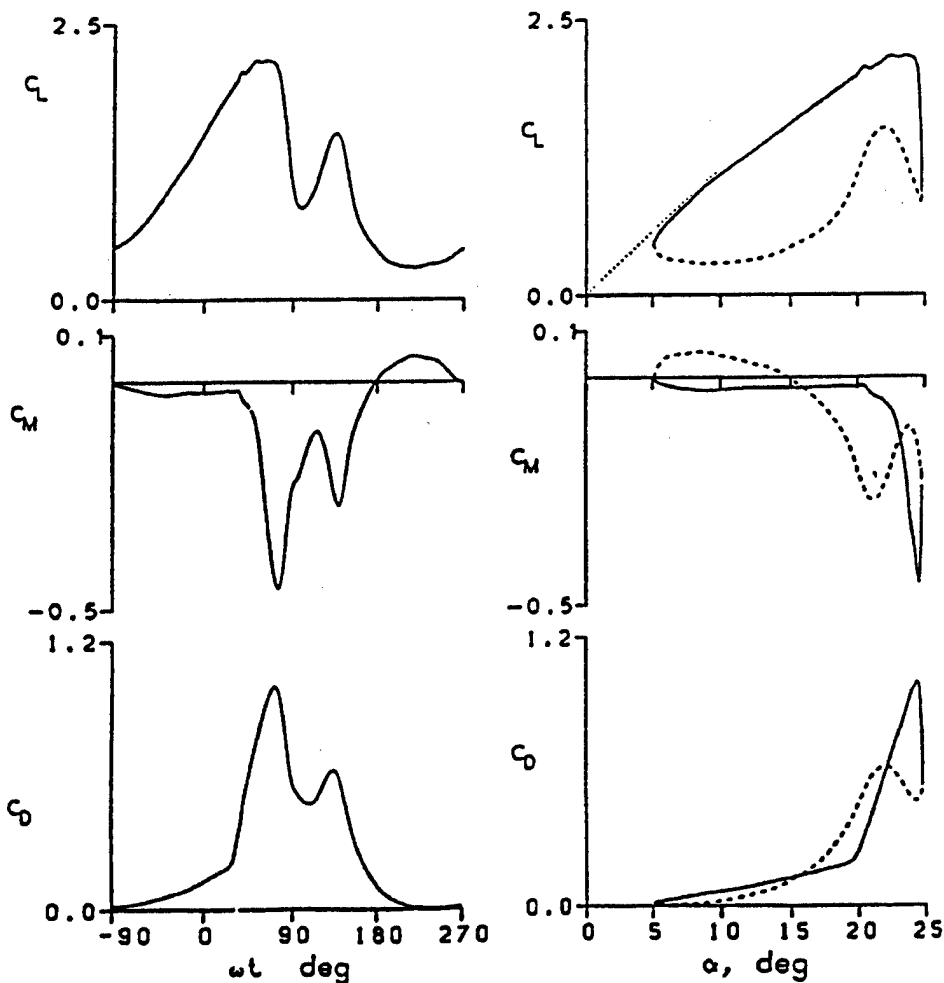


Fig.34. Lift, drag and pitching moment for the case of  $4 \pm 2$  deg at different reduced frequencies (ref. 1)



NACA 0012 AIRFOIL

FRAME : 14023

Re = 2.43 E6

$C_{Lmax} = 2.17$

$\alpha_{Lmax} = 23.6^\circ$

$\alpha_{Cmin} = 14.4^\circ$

$A0 = 14.83^\circ$

$A1 = 9.89^\circ$

$C_{Mmin} = -0.46$

$\xi = 0.011$

$-C_{Pmax} = 12.0$

TRIP

$k = 0.150$

$M = 0.182$

$C_{Dmax} = 1.00$

$M_{max} = 0.723$

$\alpha_{Mmax} = 19.5^\circ$

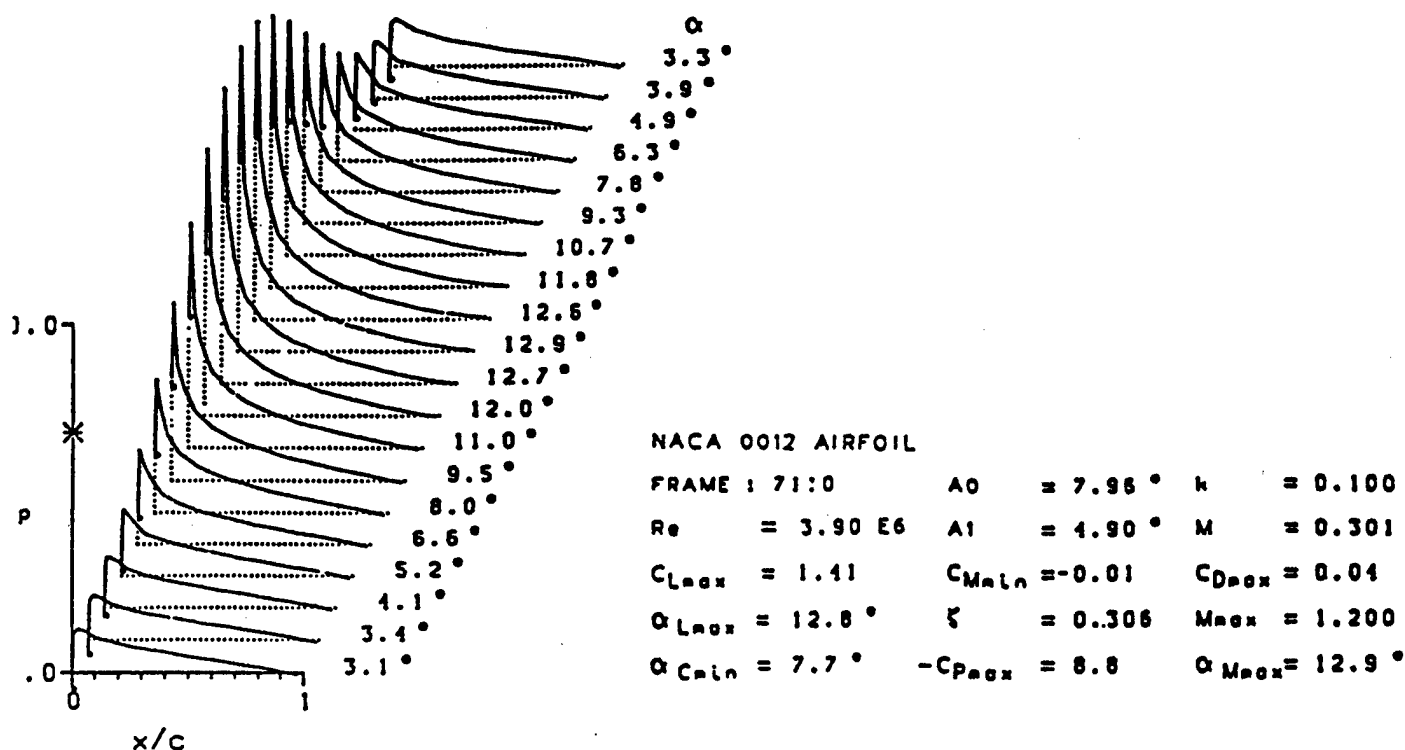


Fig. 36a. A typical plot of instantaneous pressure distributions (ref. 12)

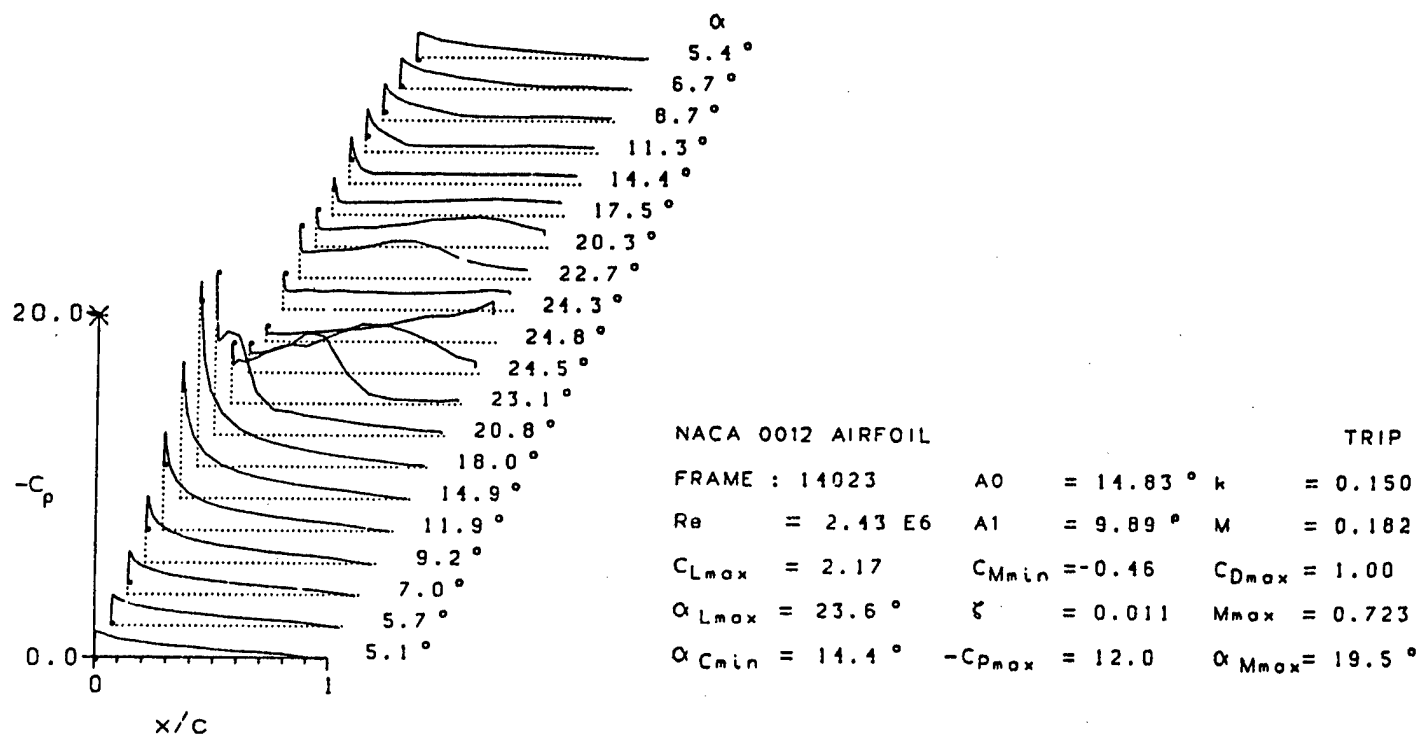
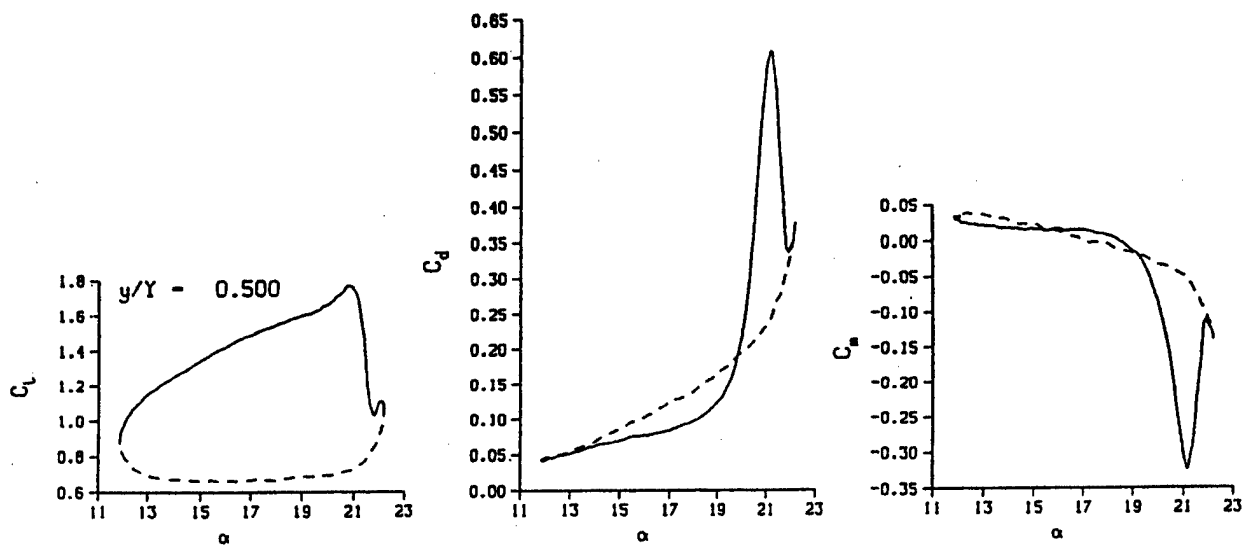


Fig. 36b. A typical plot of instantaneous pressure distributions showing a vortex development (ref. 12)



DataPointID: 2DPOT1.R0814

$\alpha = 17.08 \pm 5.18$  Deg.

$\nu = 0.095$

Fig. 37. Lift, drag, and pitching moment for  $17 \pm 5$  deg,  $k = 0.1$  (ref. 1)

Upper Pressure vs. Chord Position  
Data Point : 2DPOT1.PM814, 50.0% Span

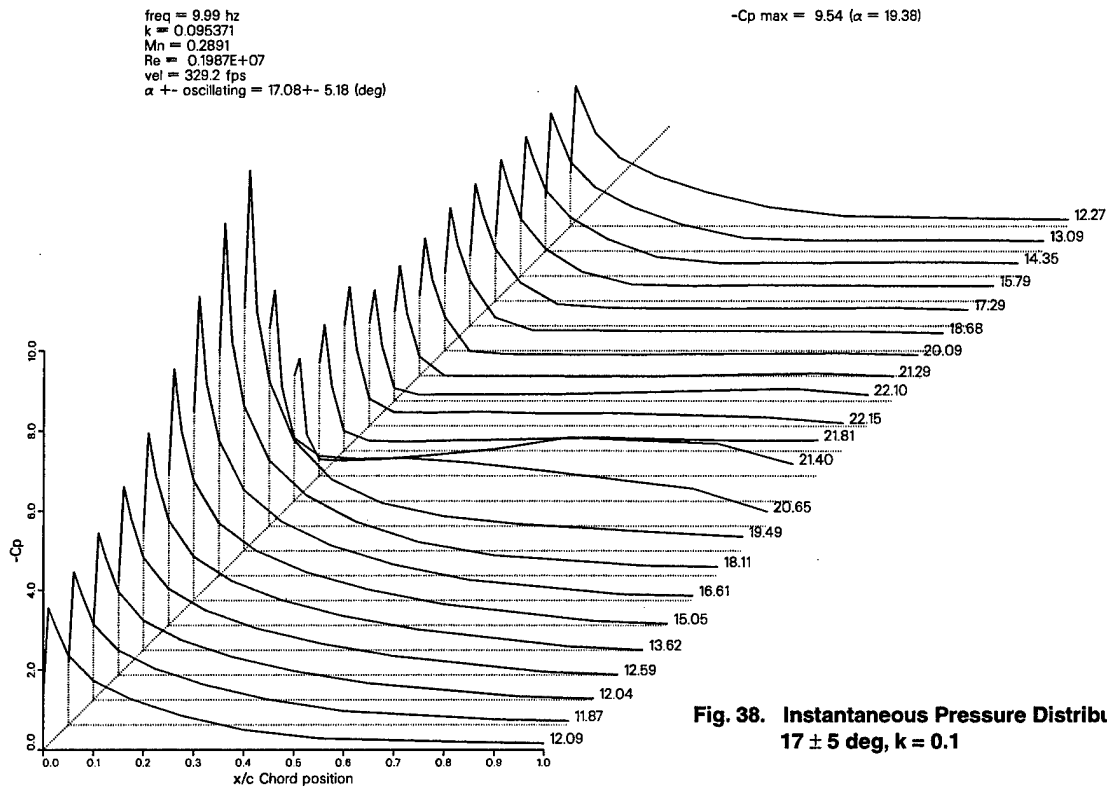


Fig. 38. Instantaneous Pressure Distributions  
 $17 \pm 5$  deg,  $k = 0.1$

Upper Surface Pressure vs. Chord Position  
Data Point : 2DPOT1.PM814 , (50.0% Span)

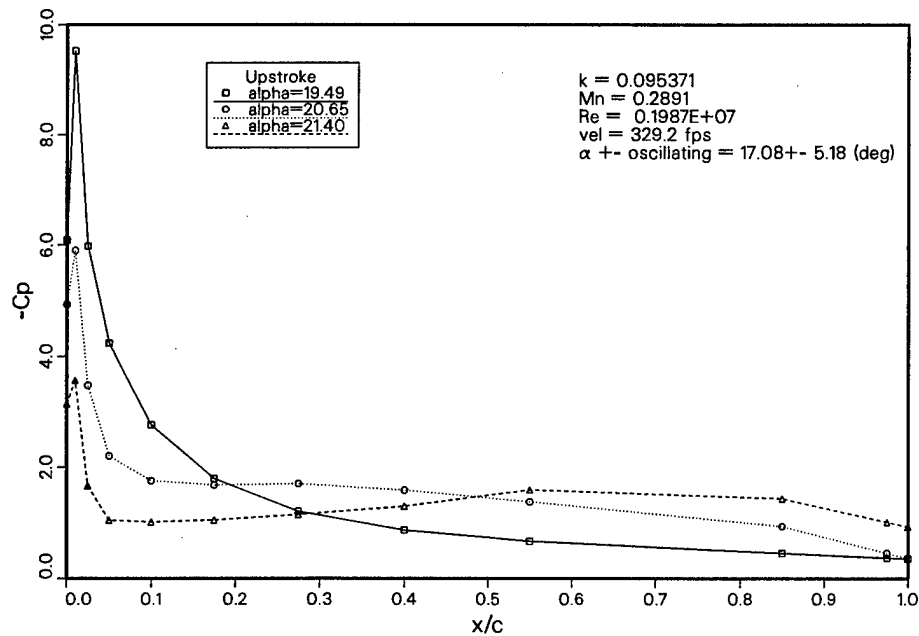


Fig. 39. Upper Surface Pressure vs. Chord Position  
 $17 \pm 5$  deg,  $k = 0.1$



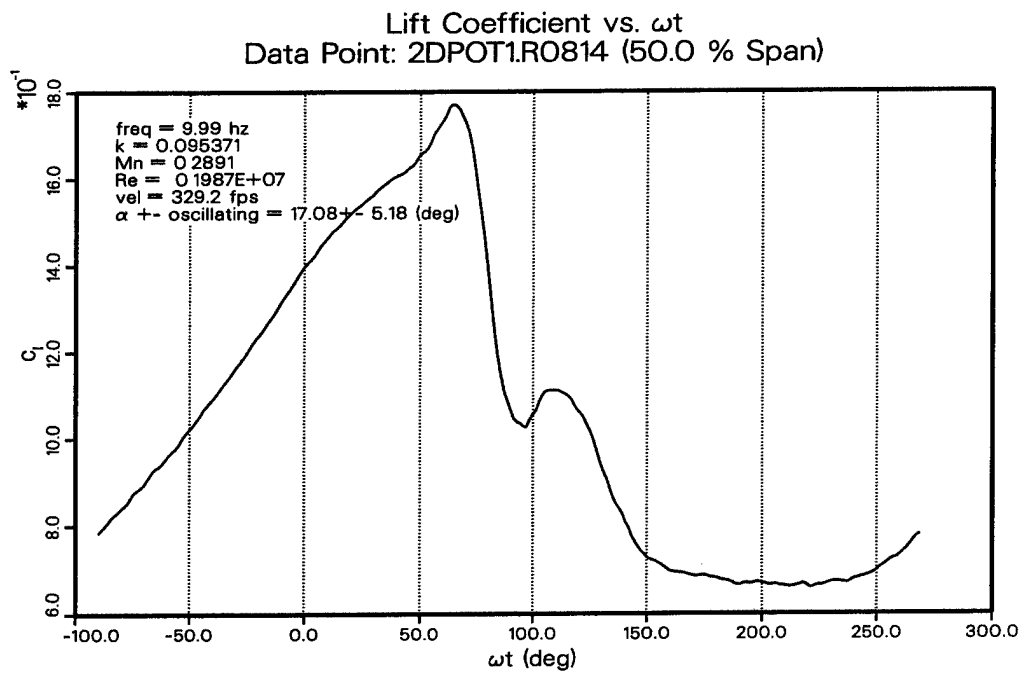


Fig. 40a

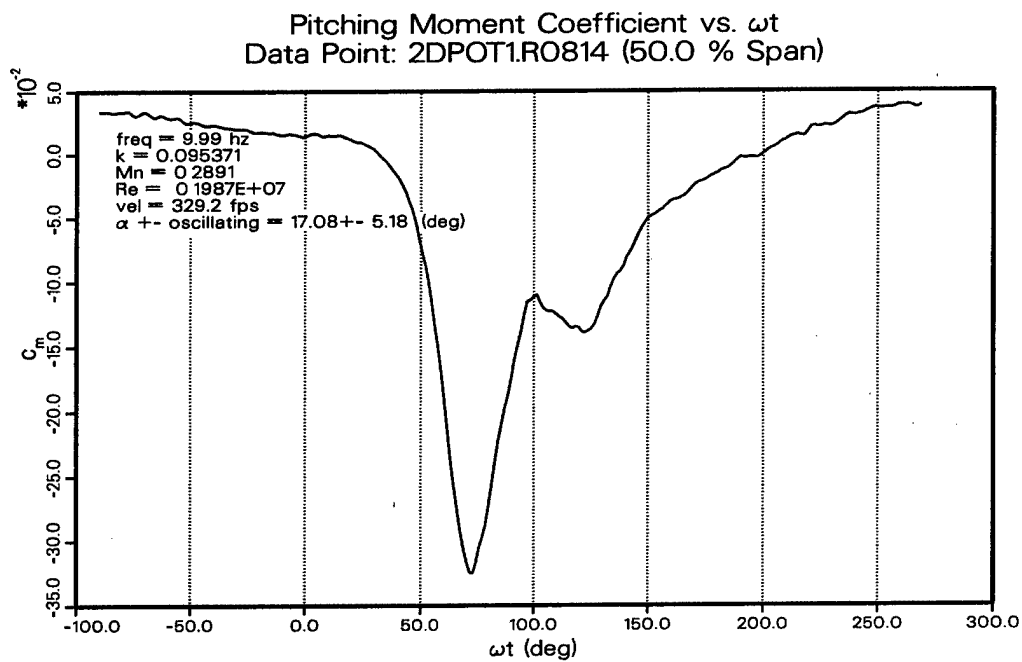


Fig. 40b

Fig. 40. Lift and Pitching Moment vs.  $\omega t$ ,  
 $17 \pm 5$  deg,  $k = 0.1$

Comparison of Lift Coefficient vs.  $\alpha$   
Data Points: 2DPOT1.R0814 and 2DQST1.R0885 (50.0 % Span)

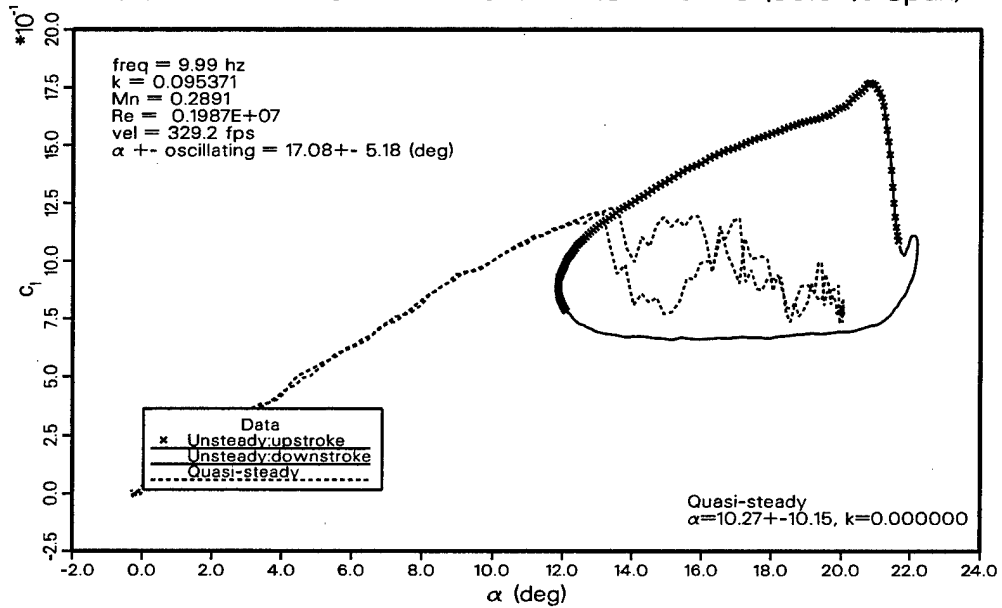


Fig. 41a

Comparison of Pitching Moment Coefficient vs.  $\alpha$   
Data Points: 2DPOT1.R0814 and 2DQST1.R0885 (50.0 % Span)

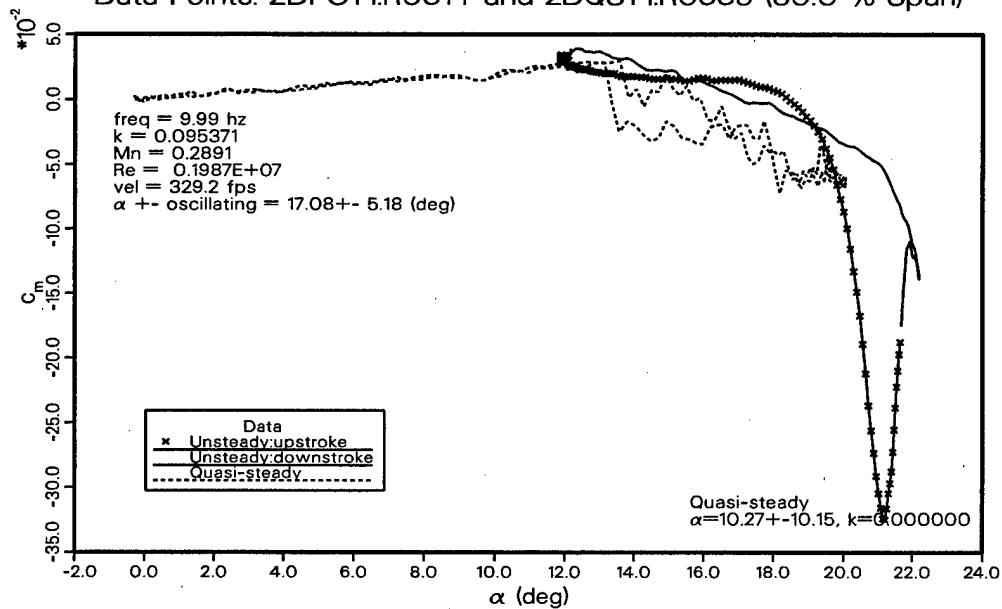
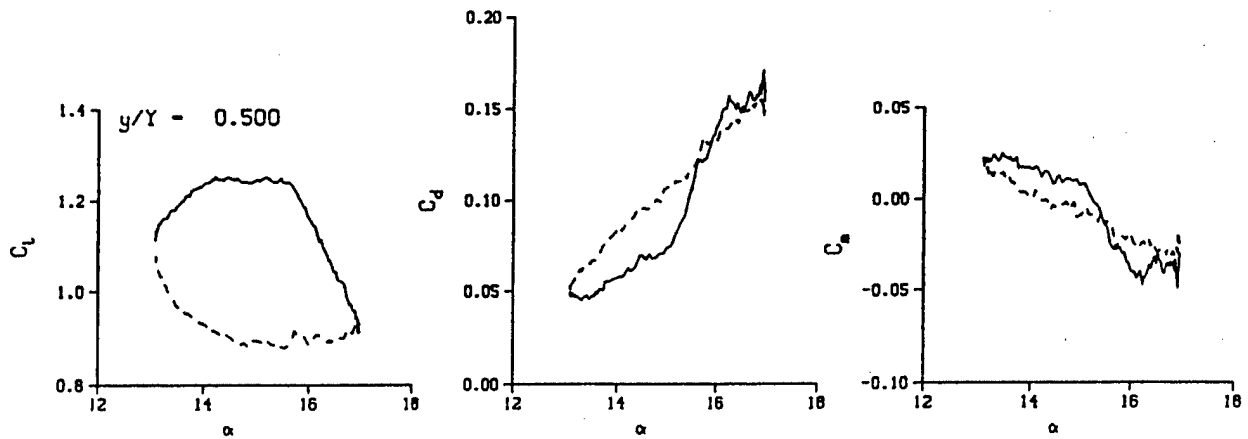
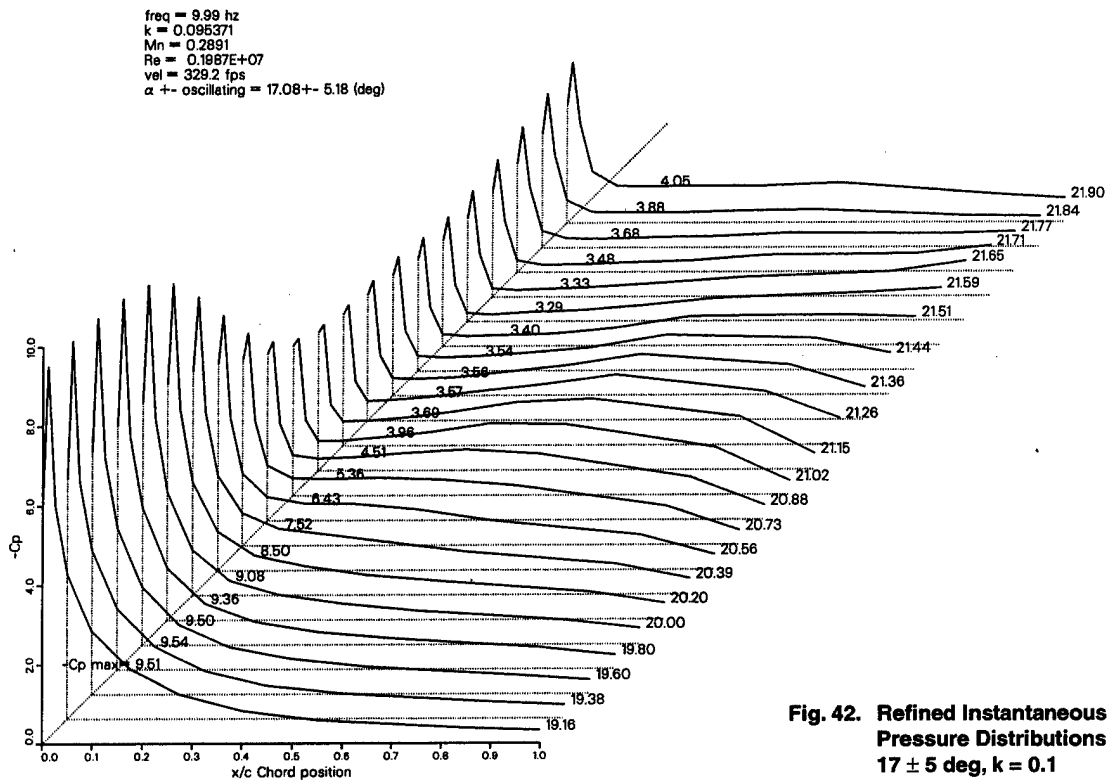


Fig. 41b

Fig. 41. Comparison of Lift and Pitching Moment vs. Angle  
 $17 \pm 5$  deg, k = 0.1

Upper Pressure vs. Chord Position  
Data Point : 2DP0T1.PM814, 50.0% Span



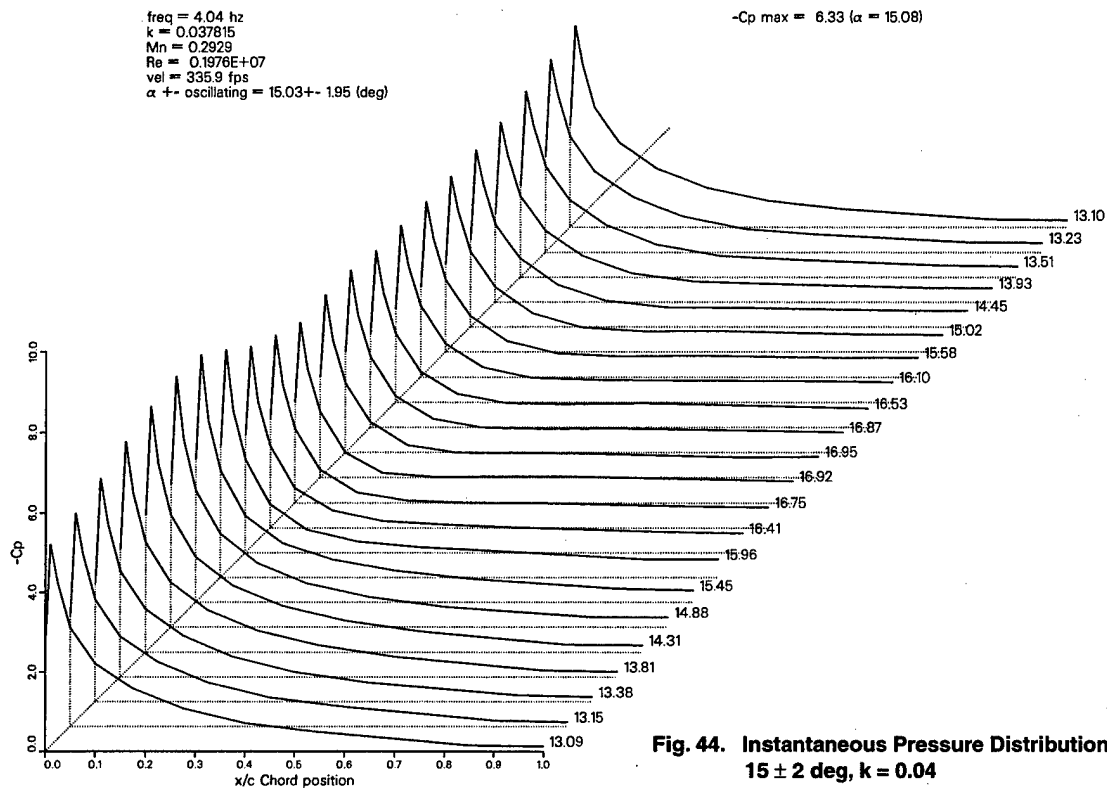
DataPointID: 2DP0T1.R0775

$\alpha = 15.03 \pm 1.95$  Deg.

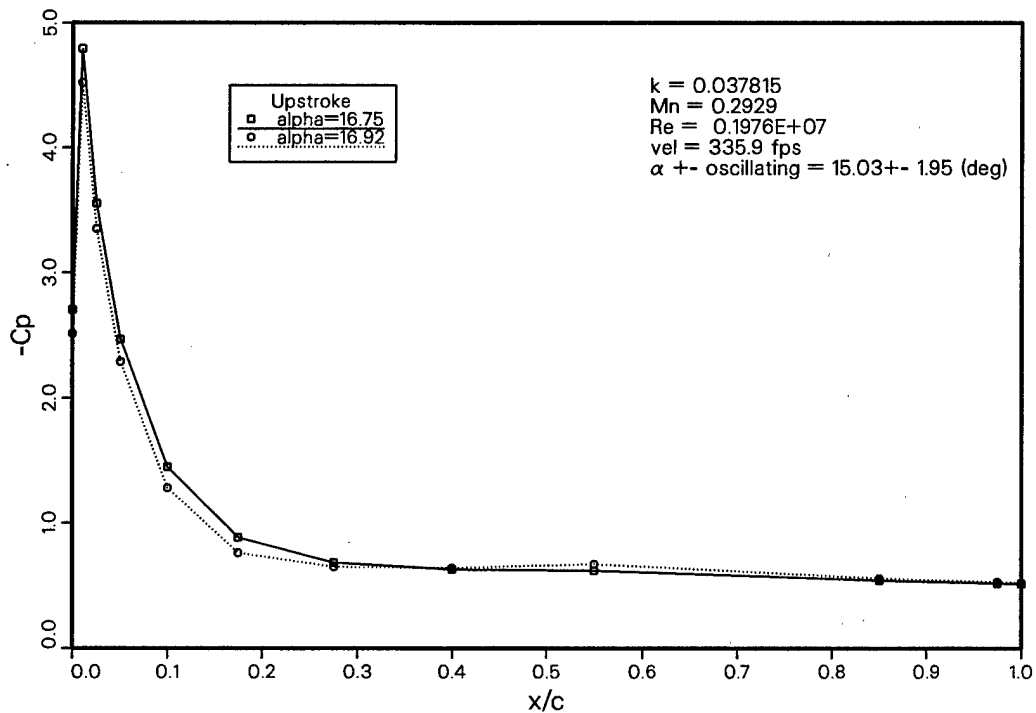
$\nu = 0.038$

Fig. 43. Lift, drag, and pitching moment for  $15 \pm 2$  deg,  $k = 0.04$  (ref. 1)

Upper Pressure vs. Chord Position  
Data Point : 2DPOT1PM775, 50.0% Span



Upper Surface Pressure vs. Chord Position  
Data Point : 2DPOT1PM775 , (50.0% Span)



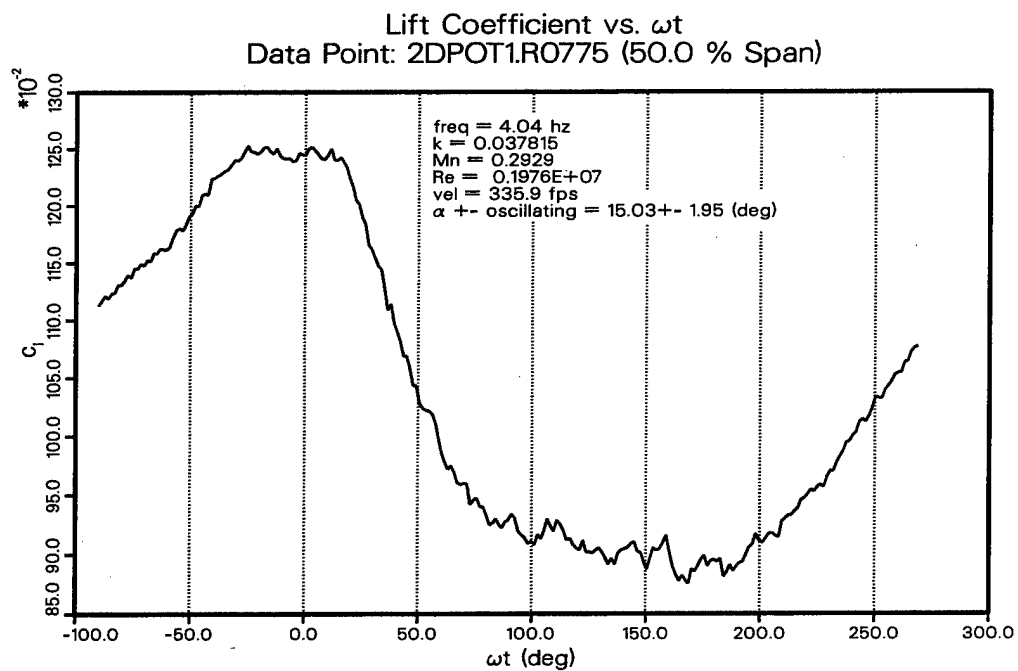


Fig. 46a

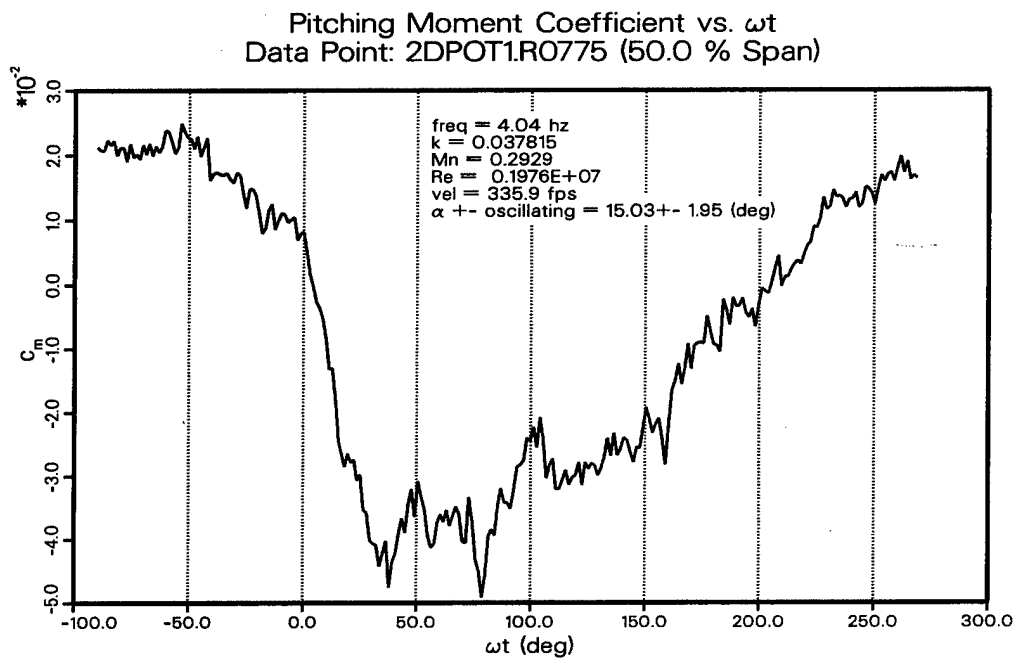


Fig. 46b

Fig. 46. Lift and Pitching Moment vs.  $\omega t$ ,  
 $15 \pm 2 \text{ deg}$ ,  $k = 0.04$

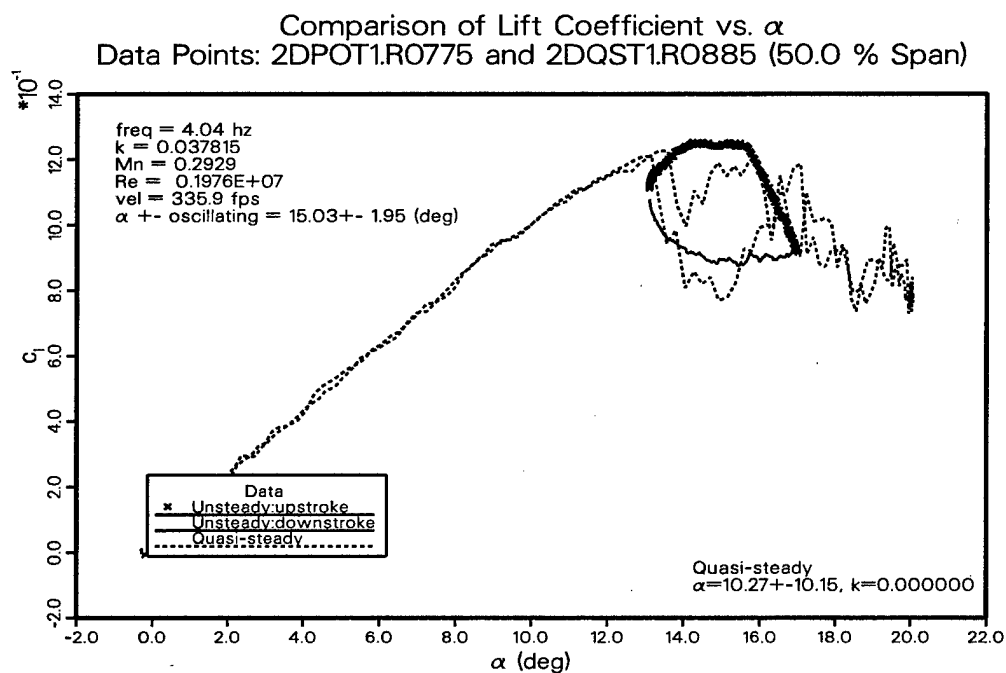


Fig. 47a

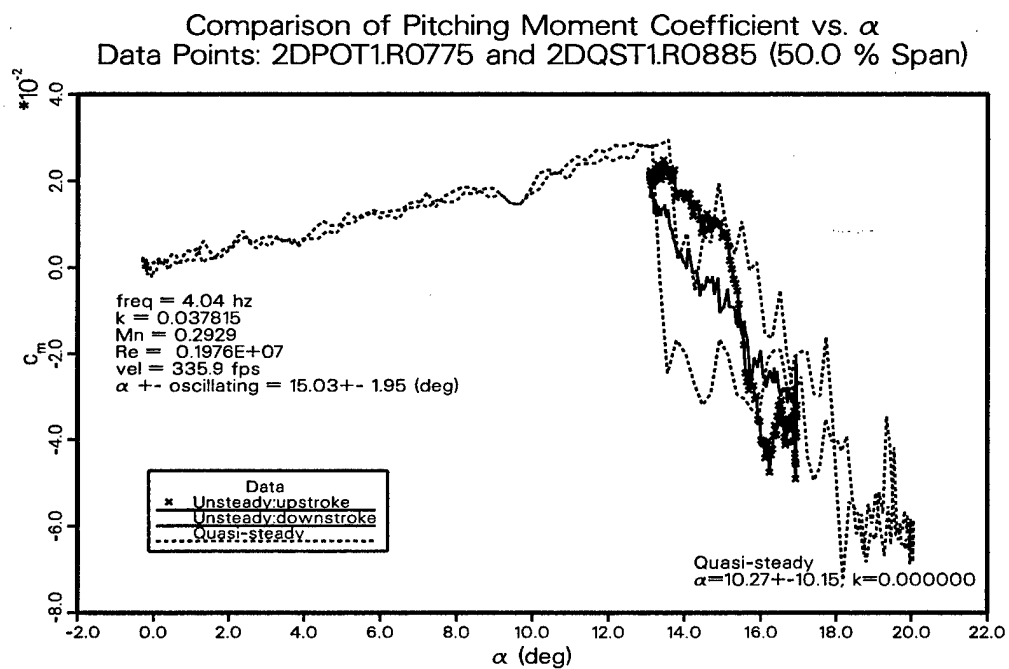
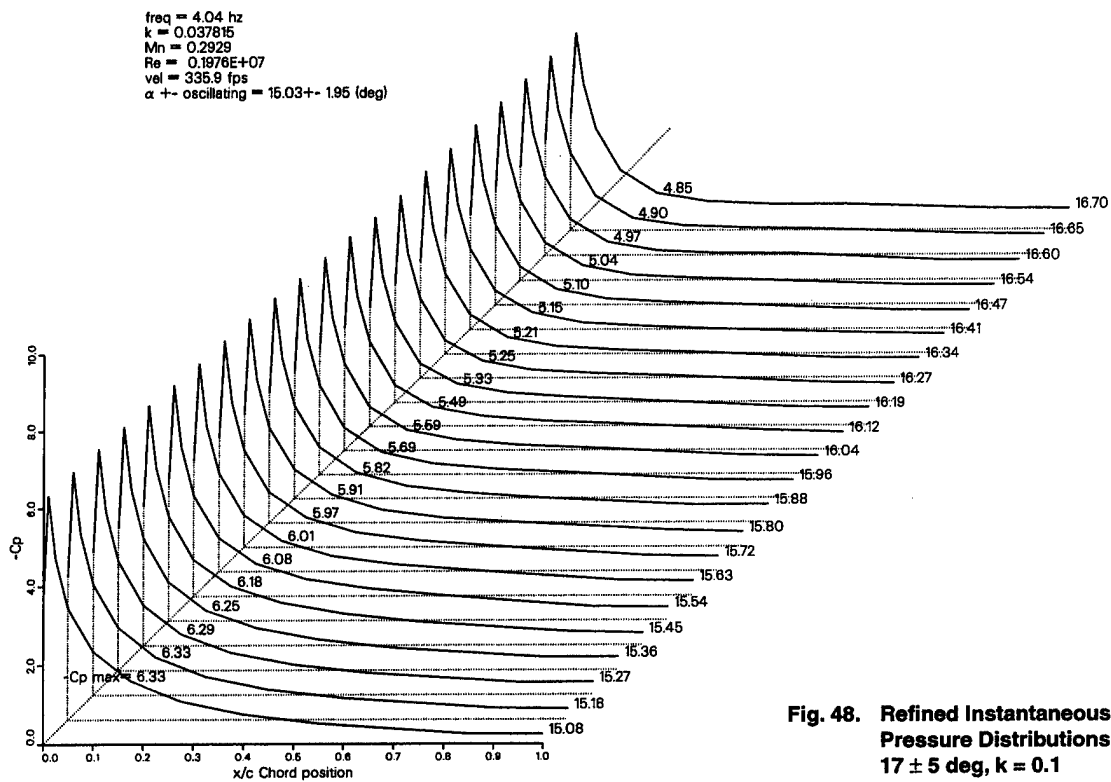


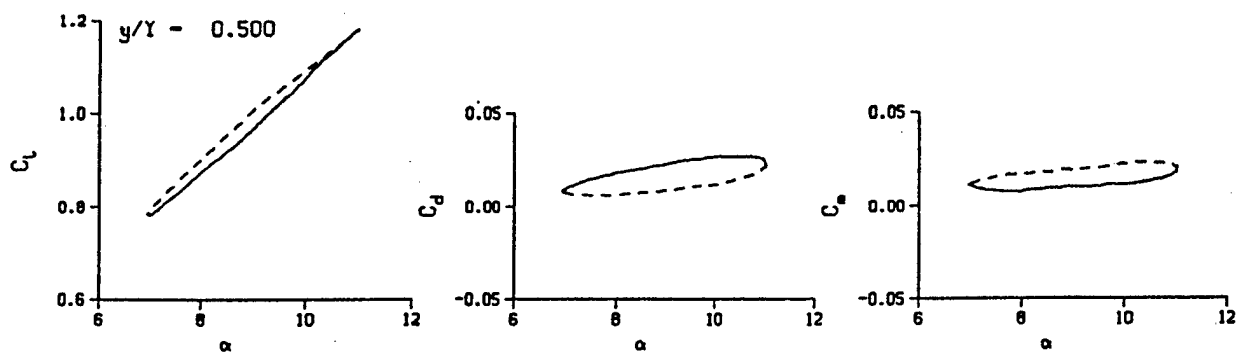
Fig. 47b

Fig. 47. Comparison of Lift and Pitching Moment vs. Angle  
 $15 \pm 2$  deg, k = 0.04

Upper Pressure vs. Chord Position  
Data Point : 2DPOT1.PM775, 50.0% Span



**Fig. 48. Refined Instantaneous Pressure Distributions**  
**17 ± 5 deg, k = 0.1**



DataPoint ID: 2DPOT1.R0766

$\alpha = 8.97 \pm 2.04$  Deg.

$\nu = 0.094$

Fig. 49. Lift, drag, and pitching moment for  $9 \pm 2$ ,  $k = 0.1$  (ref. 1)

Upper Pressure vs. Chord Position  
Data Point : 2DPOT1.PM766, 50.0% Span

freq = 10.03 hz  
 $k = 0.093861$   
Min = 0.2927  
Re =  $0.1971E+07$   
vel = 335.7 fps  
 $\alpha \pm$  oscillating =  $8.97 \pm 2.04$  (deg)

-Cp max = 4.98 ( $\alpha = 11.00$ )

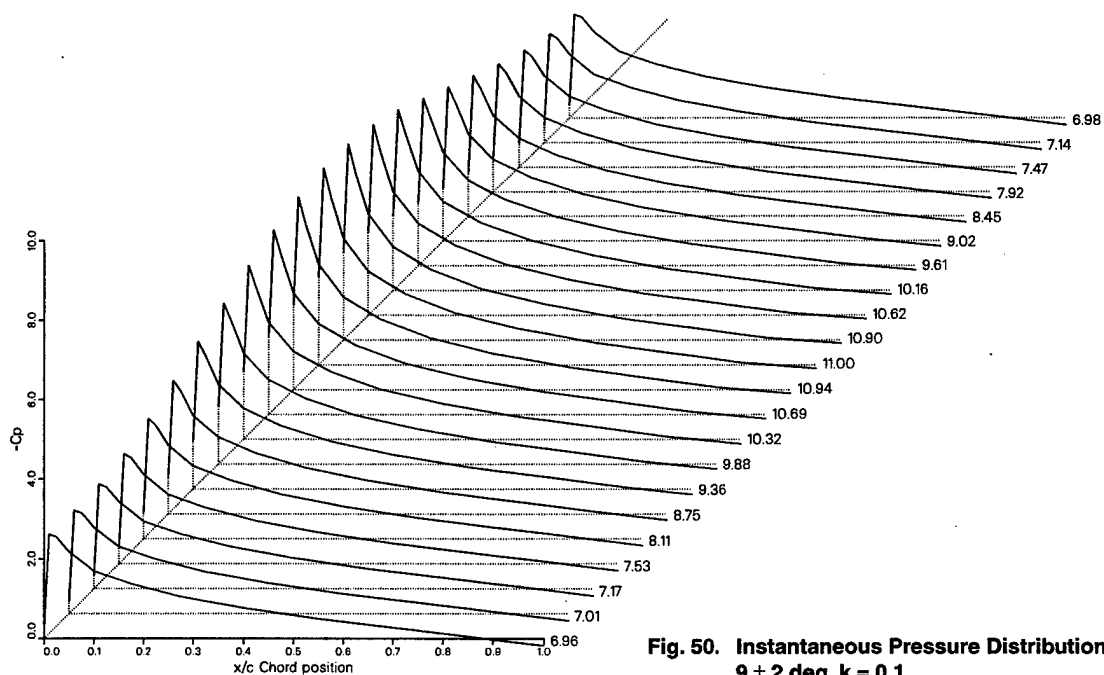


Fig. 50. Instantaneous Pressure Distributions  
 $9 \pm 2$  deg,  $k = 0.1$



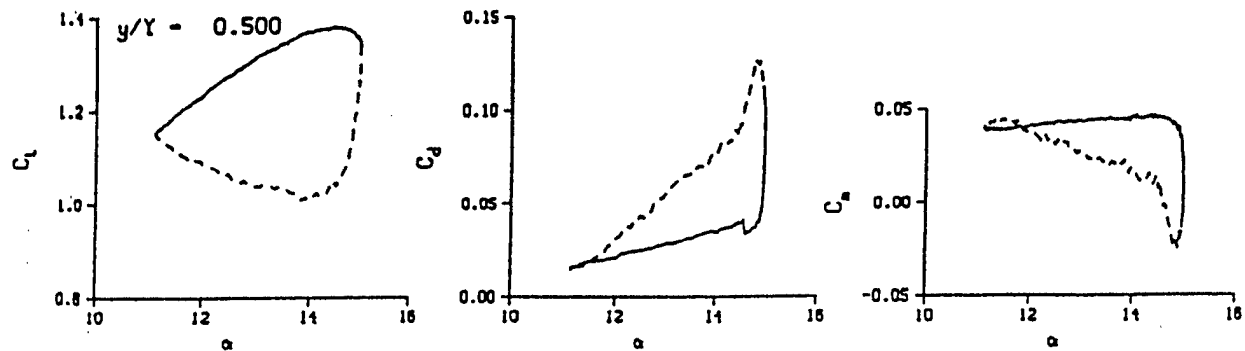


Fig. 51a

DataPointID: 2DP0T1.R0770

$\alpha = 13.07 \pm 1.97$  Deg.

$\nu = 0.038$

*note: different y-axis scale*

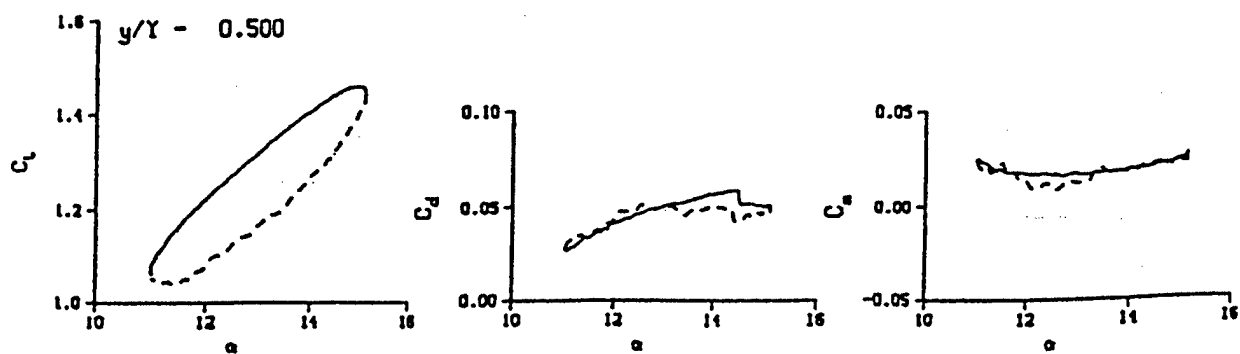


Fig. 51b

DataPointID: 2DP0T1.R0772

$\alpha = 13.08 \pm 2.13$  Deg.

$\nu = 0.133$

Fig. 51. Lift, drag, and pitching moment for  $13 \pm 2$  deg, at different reduced frequencies (*ref. 1*)

Upper Pressure vs. Chord Position  
Data Point : 2DPOT1.PM770, 50.0% Span

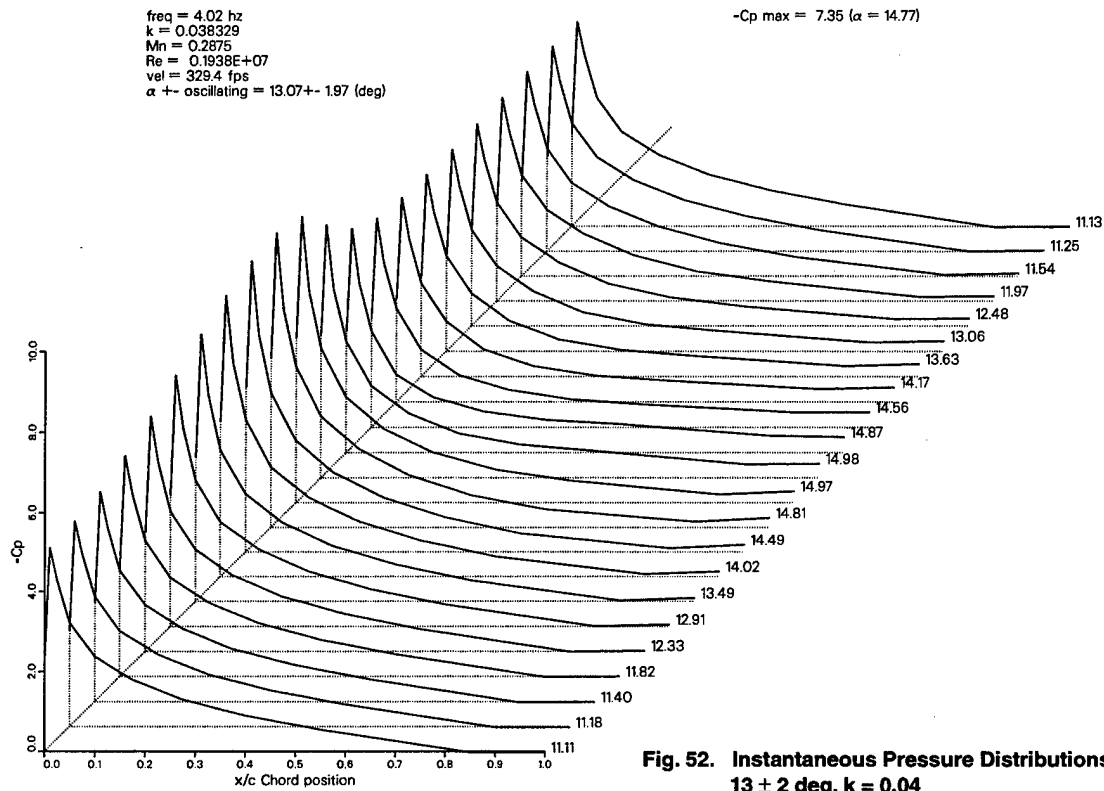


Fig. 52. Instantaneous Pressure Distributions  
 $13 \pm 2$  deg,  $k = 0.04$

Upper Pressure vs. Chord Position  
Data Point : 2DPOT1.PM772, 50.0% Span

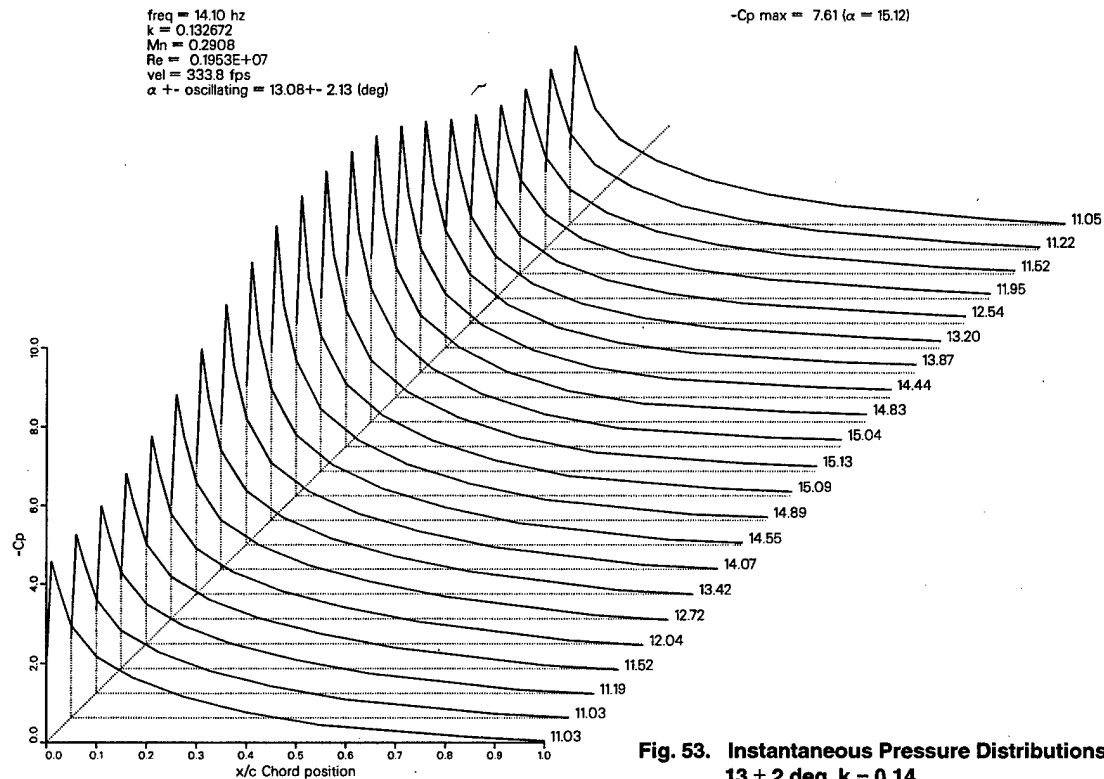


Fig. 53. Instantaneous Pressure Distributions  
 $13 \pm 2$  deg,  $k = 0.14$

Upper Surface Pressure vs. Chord Position  
Data Point : 2DPOT1.PM770 , (50.0% Span)

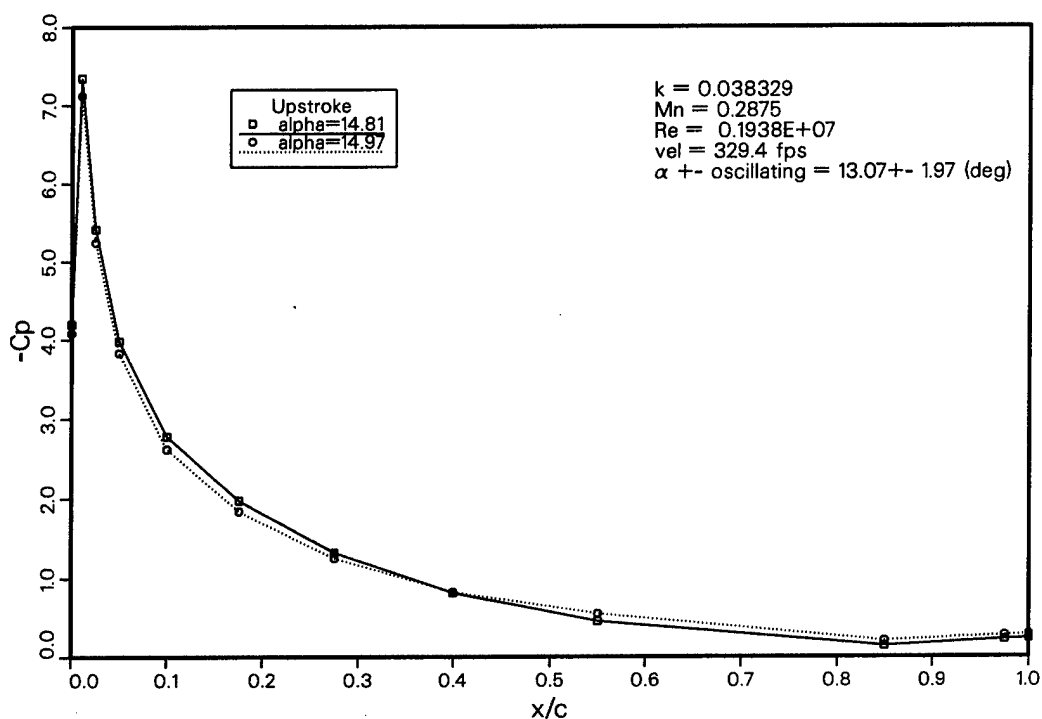


Fig. 54. Upper Surface Pressure vs. Chord Position  
 $13 \pm 2 \text{ deg}$ ,  $k = 0.04$

Upper Surface Pressure vs. Chord Position  
Data Point : 2DPOT1.PM772 , (50.0% Span)

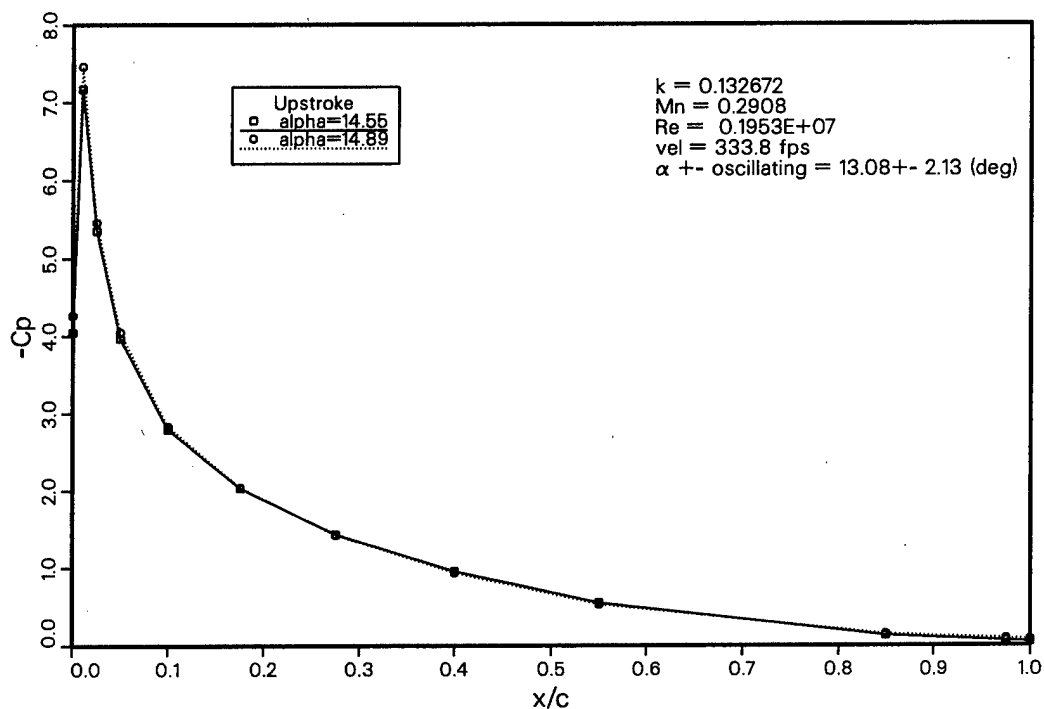


Fig. 55. Upper Surface Pressure vs. Chord Position  
 $13 \pm 2 \text{ deg}$ ,  $k = 0.14$

Comparison of Lift Coefficient vs.  $\alpha$   
Data Points: 2DPOT1.R0770 and 2DQST1.R0885 (50.0 % Span)

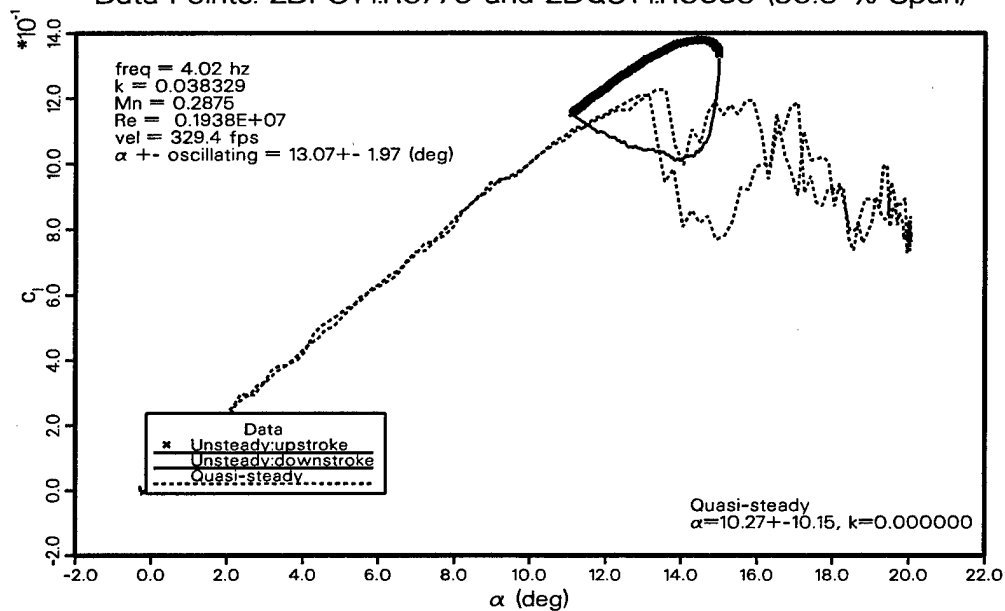


Fig. 56a

Comparison of Pitching Moment Coefficient vs.  $\alpha$   
Data Points: 2DPOT1.R0770 and 2DQST1.R0885 (50.0 % Span)

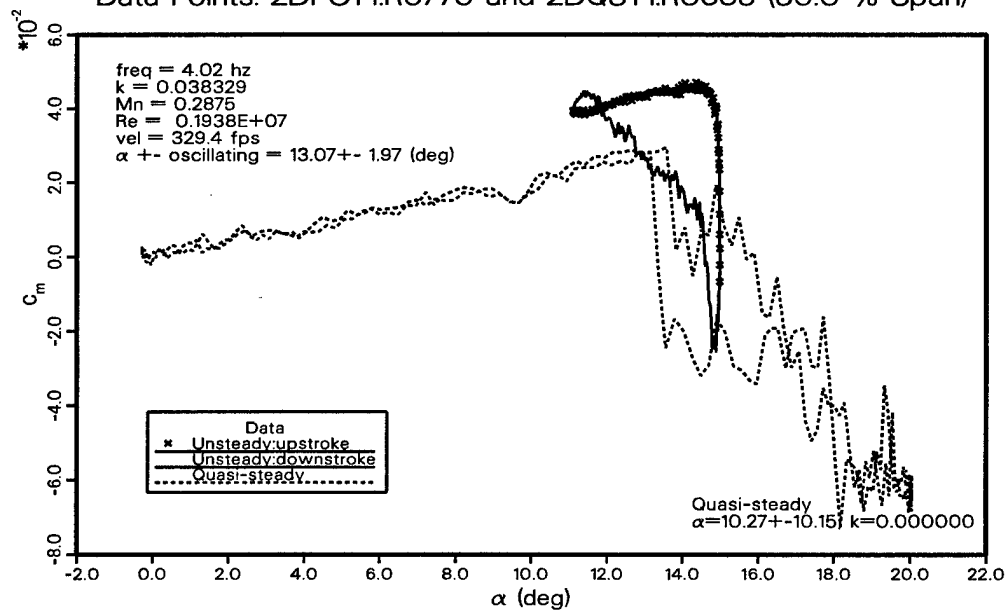


Fig. 56b

Fig. 56. Comparison of Lift and Pitching Moment vs. Angle  
 $13 \pm 2$  deg, k = 0.04

Comparison of Lift Coefficient vs.  $\alpha$   
Data Points: 2DPOT1.R0772 and 2DQST1.R0885 (50.0 % Span)

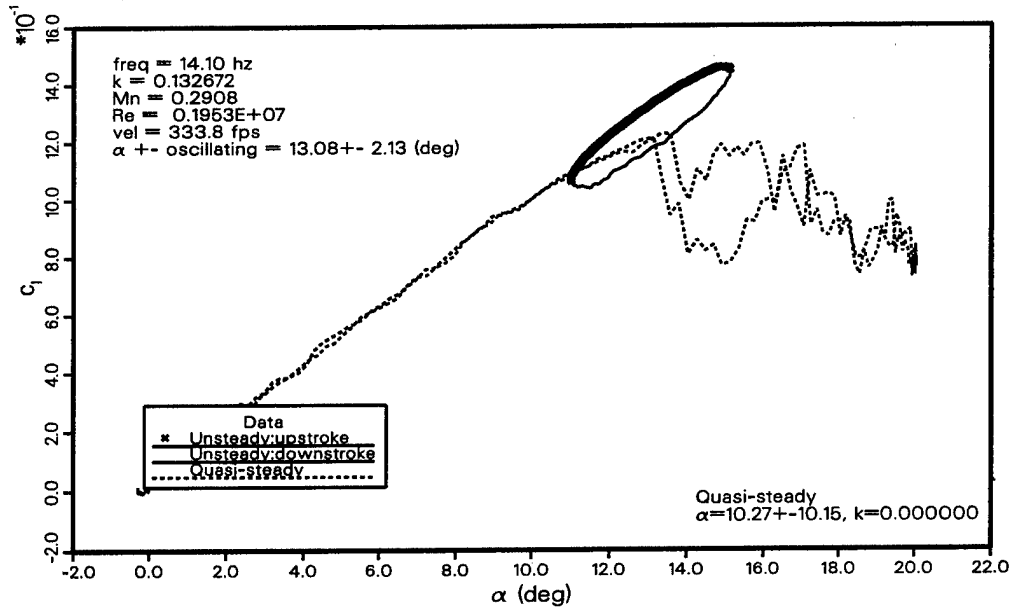


Fig. 57a

Comparison of Pitching Moment Coefficient vs.  $\alpha$   
Data Points: 2DPOT1.R0772 and 2DQST1.R0885 (50.0 % Span)

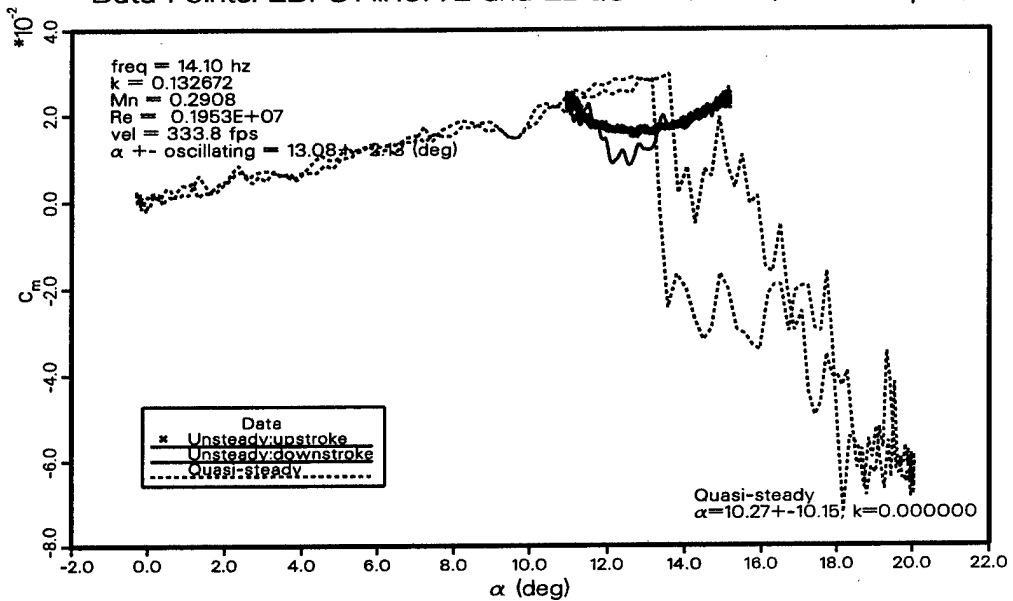


Fig. 57b

Fig. 57. Comparison of Lift and Pitching Moment vs. Angle  
 $13 \pm 2$  deg,  $k = 0.14$

Upper Pressure vs. Chord Position  
Data Point : 2DPOT1.PM770, 50.0% Span

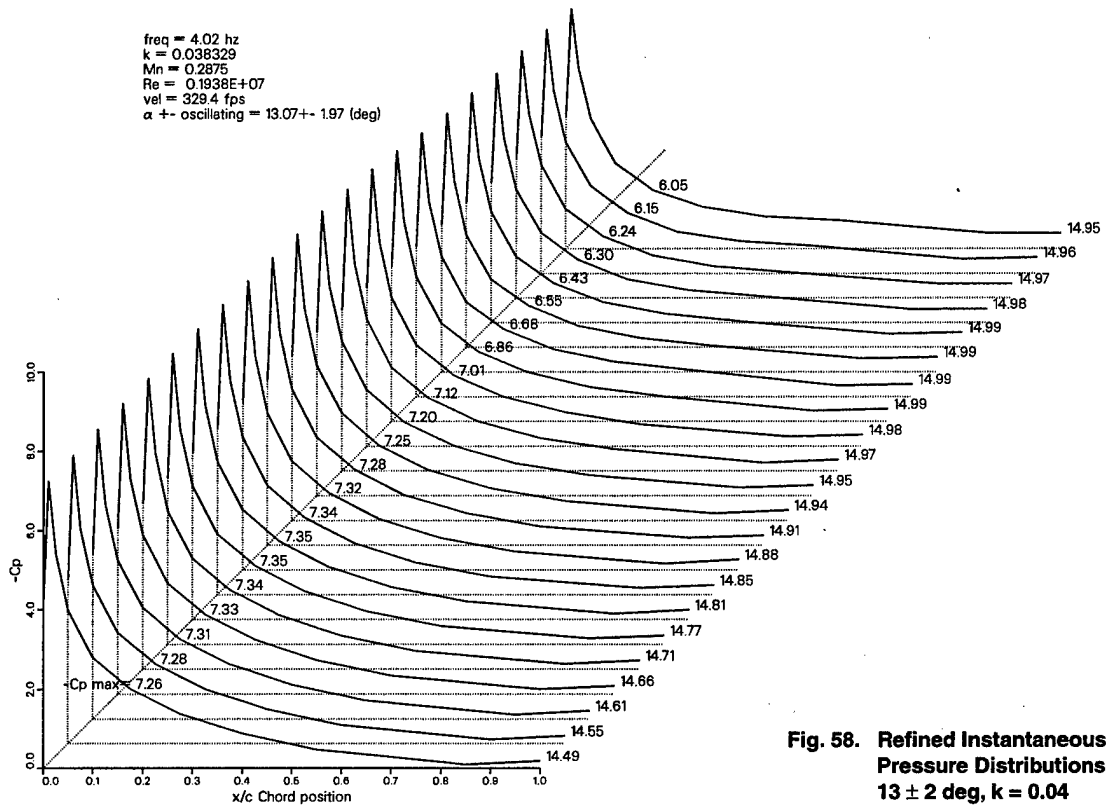


Fig. 58. Refined Instantaneous Pressure Distributions  
13 ± 2 deg, k = 0.04

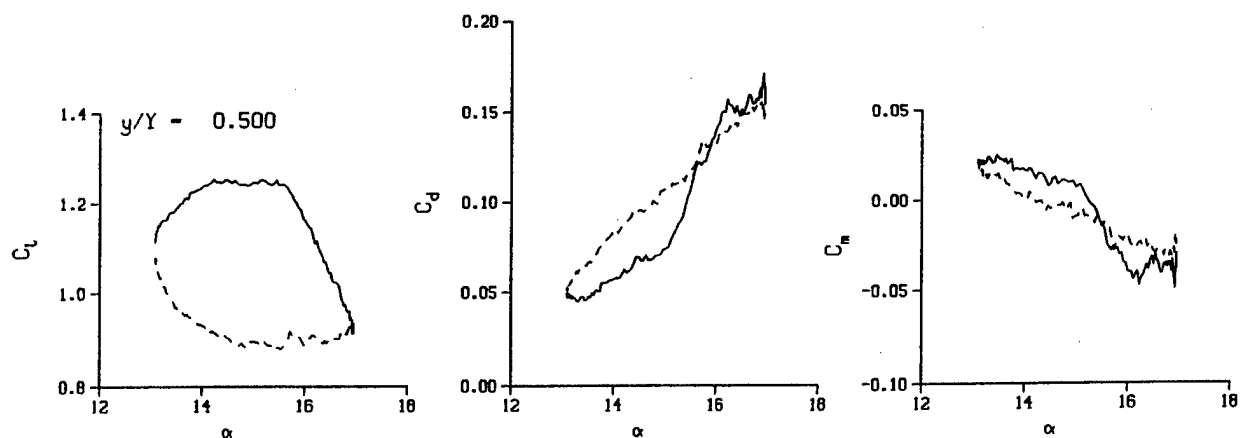


Fig. 59a

DataPointID: 2DPOT1.R0775

$\alpha = 15.03 \pm 1.95$  Deg.

$\nu = 0.038$

*note: different y-axis scale*

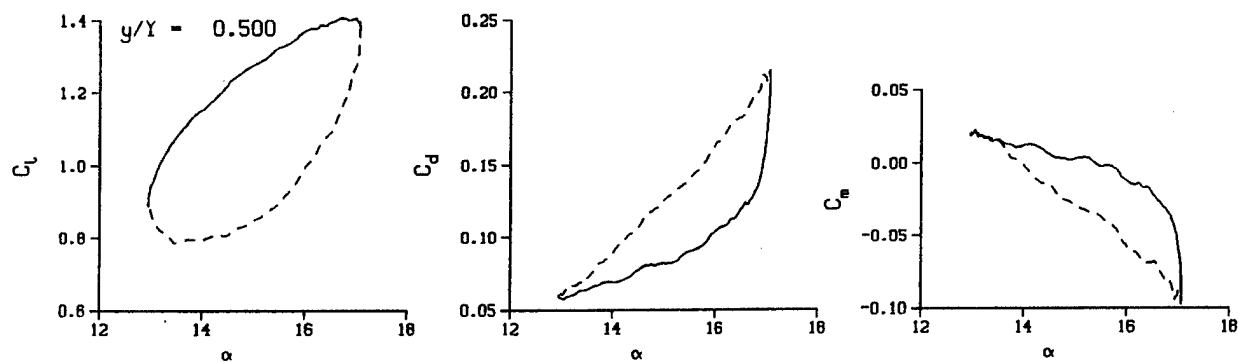


Fig. 59b

DataPointID: 2DPOT1.R0777

$\alpha = 15.04 \pm 2.11$  Deg.

$\nu = 0.133$

Fig. 59. Lift, drag and pitching moment for  $15 \pm 2$  deg at different reduced frequencies (ref. 1)

Upper Pressure vs. Chord Position  
Data Point : 2DPOT1.PM775, 50.0% Span

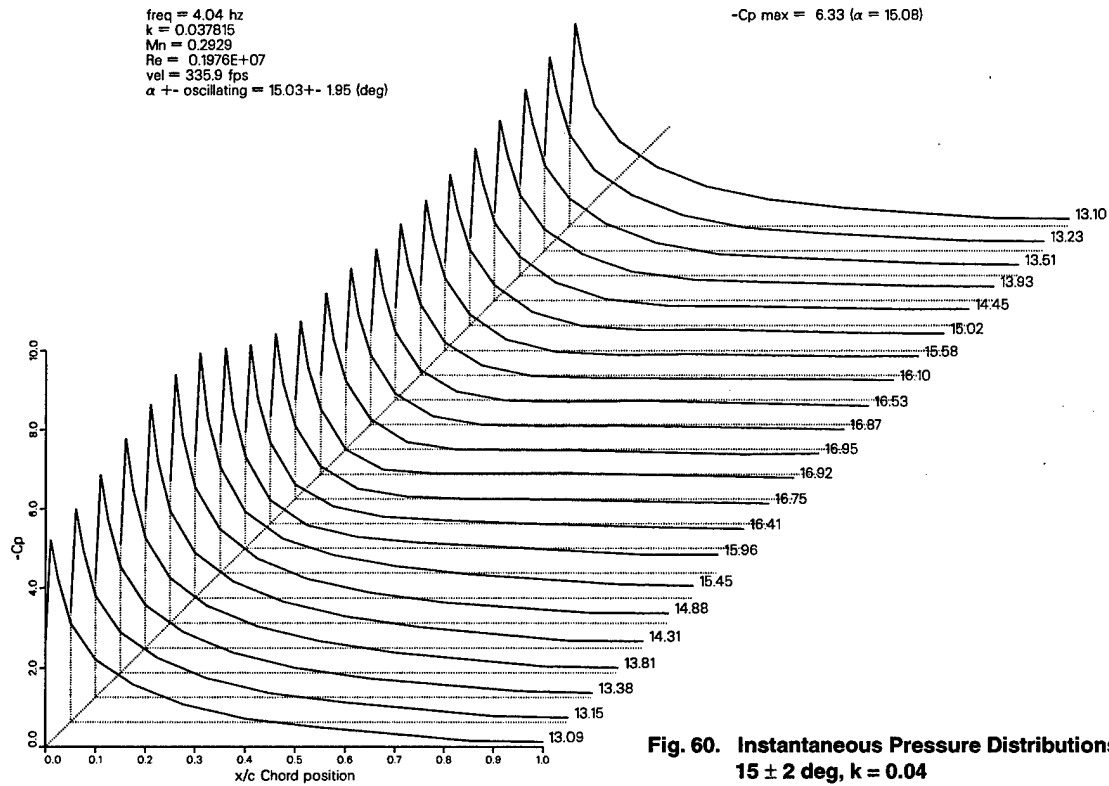


Fig. 60. Instantaneous Pressure Distributions  
15 ± 2 deg, k = 0.04



Upper Surface Pressure vs. Chord Position  
Data Point : 2DPOT1.PM775 , (50.0% Span)

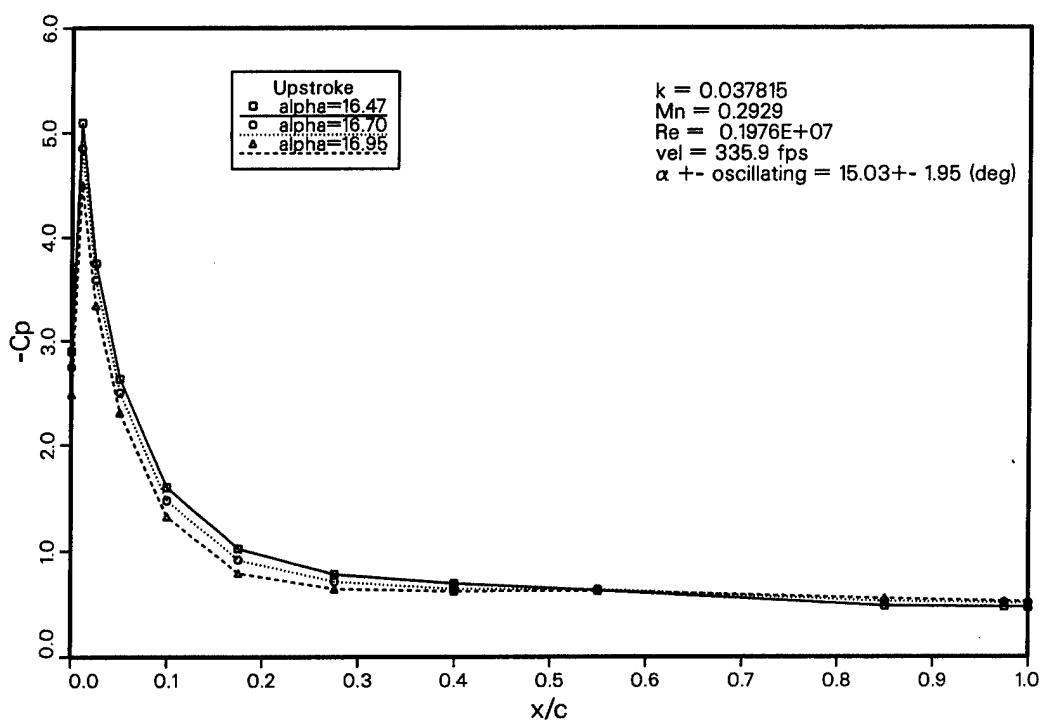


Fig. 61. Upper Surface Pressure vs. Chord Position  
 $15 \pm 2 \text{ deg}$ ,  $k = 0.04$ , upstroke

Upper Surface Pressure vs. Chord Position  
Data Point : 2DPOT1.PM775 , (50.0% Span)

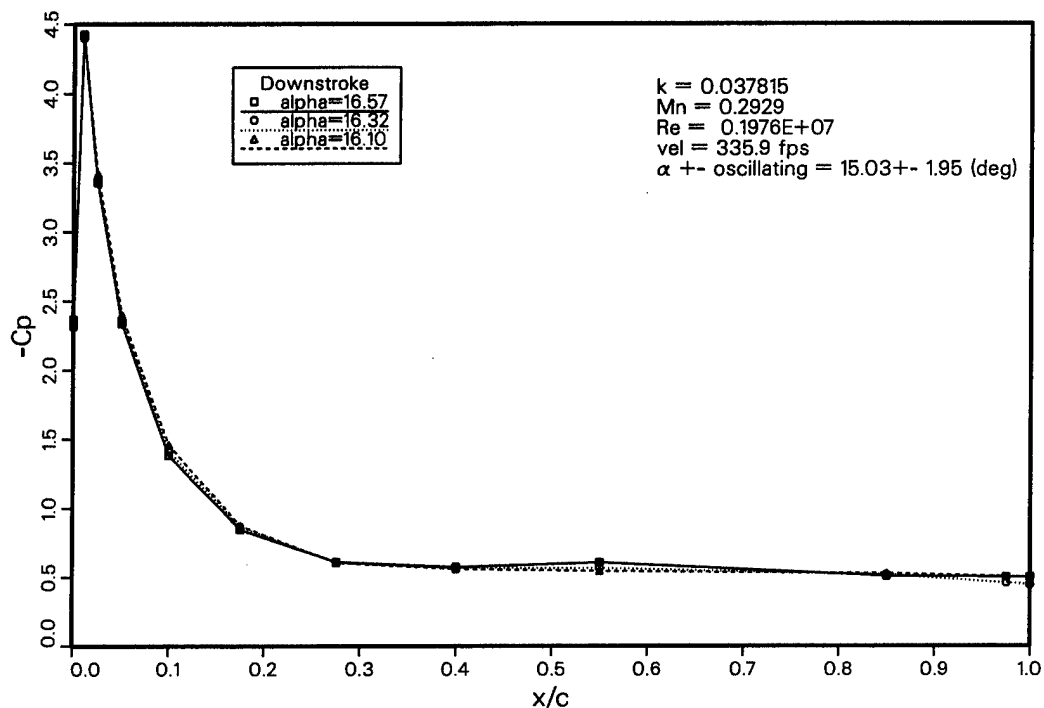
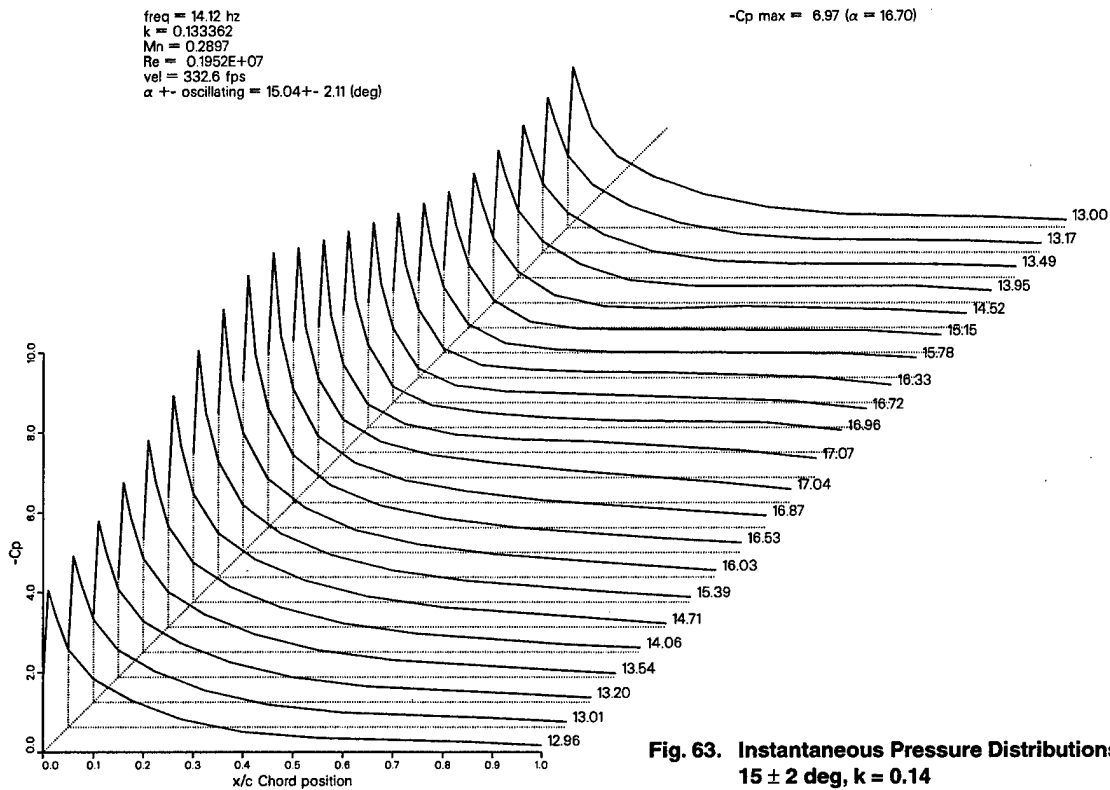
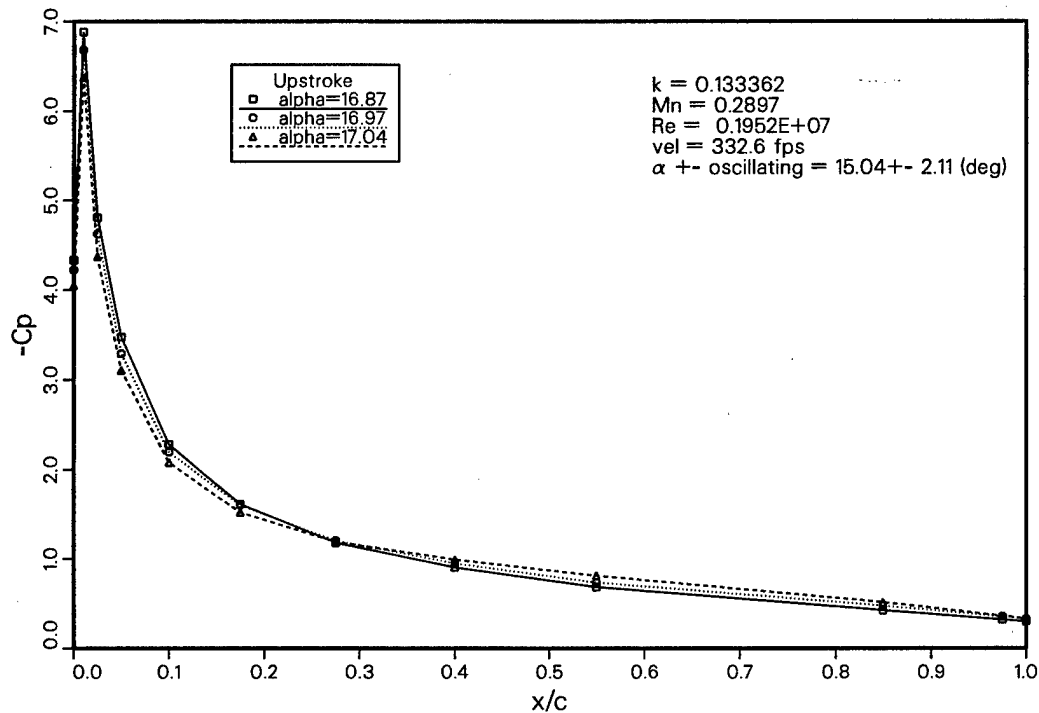


Fig. 62. Upper Surface Pressure vs. Chord Position  
 $15 \pm 2 \text{ deg}$ ,  $k = 0.04$ , downstroke

Upper Pressure vs. Chord Position  
Data Point : 2DPOT1.PM777, 50.0% Span



Upper Surface Pressure vs. Chord Position  
Data Point : 2DPOT1.PM777 , (50.0% Span)



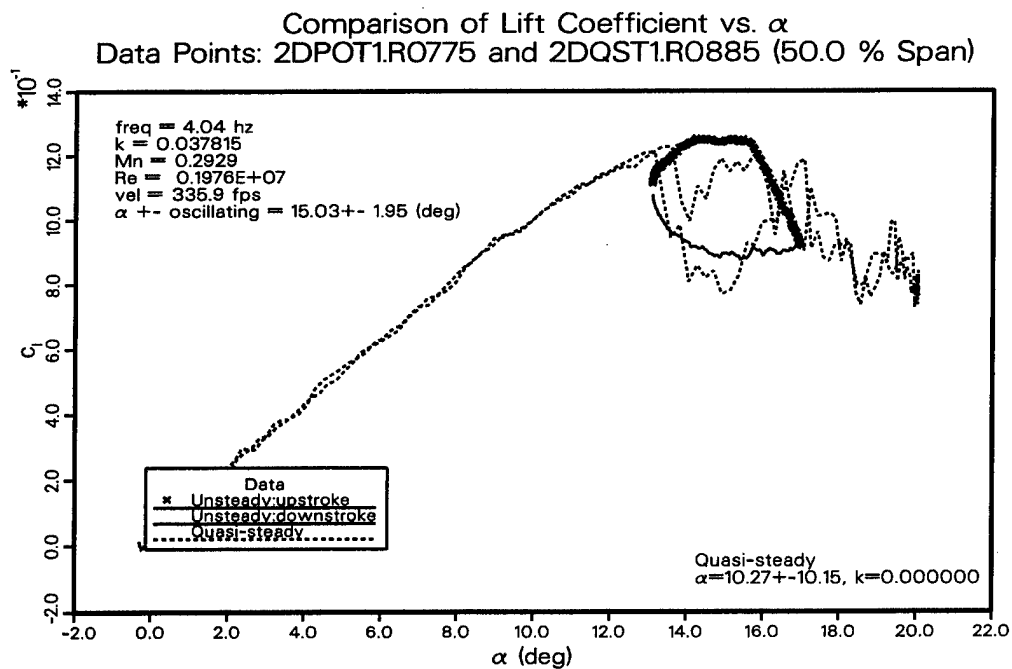


Fig. 65a

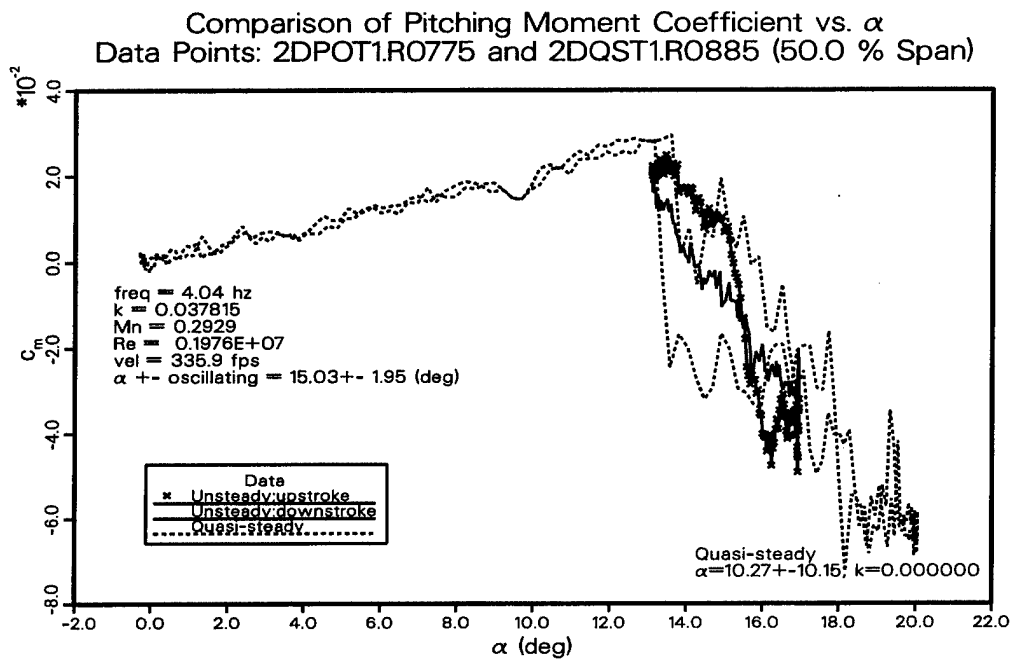


Fig. 65b

Fig. 65. Comparison of Lift and Pitching Moment vs. Angle  
 $15 \pm 2 \text{ deg}$ ,  $k = 0.04$

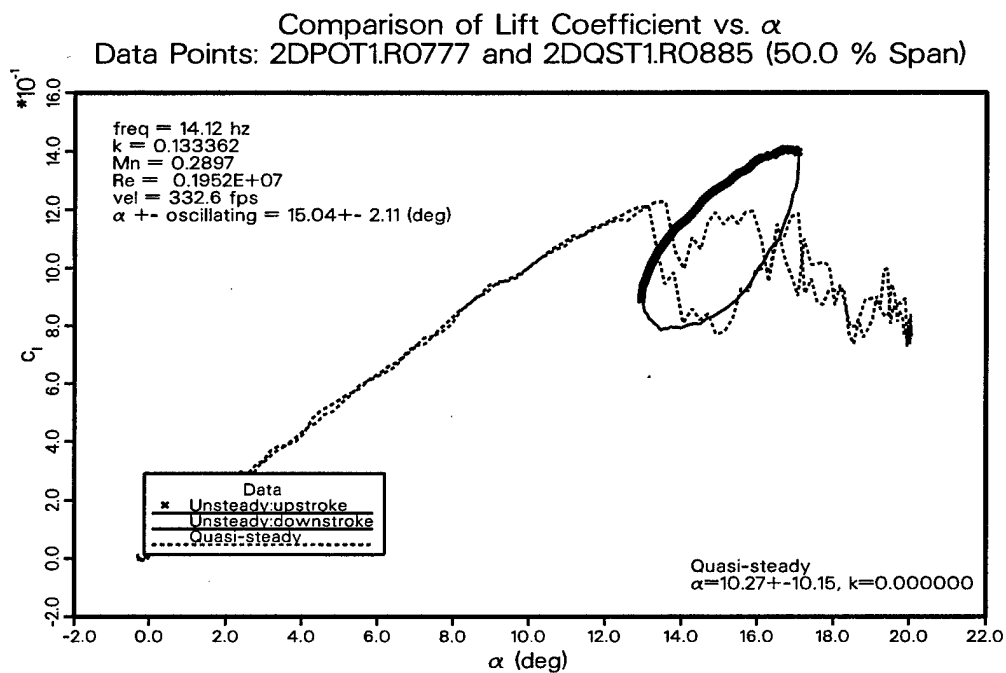


Fig. 66a

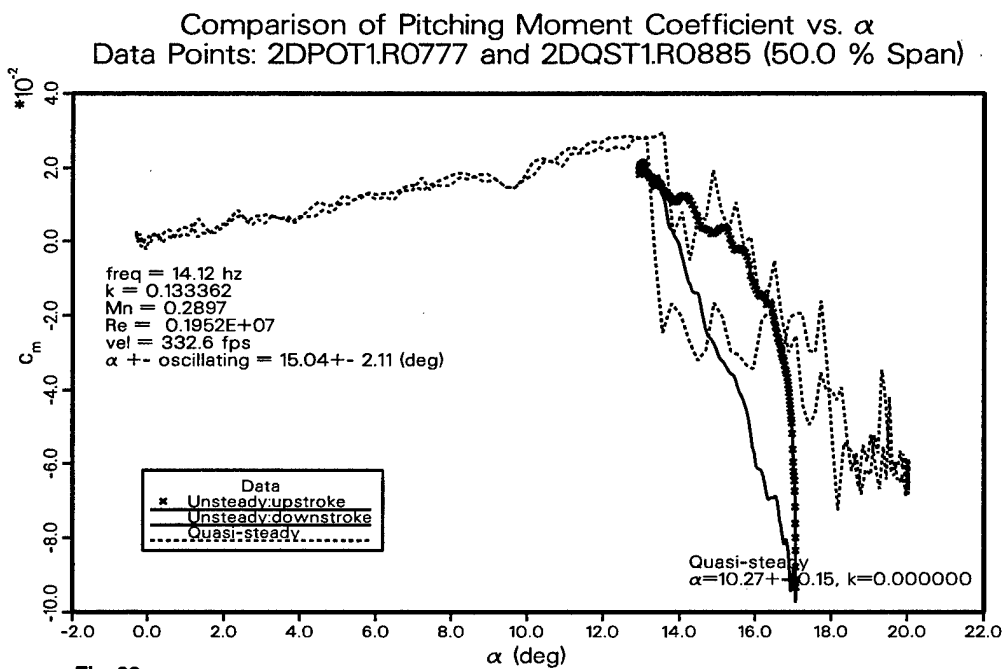
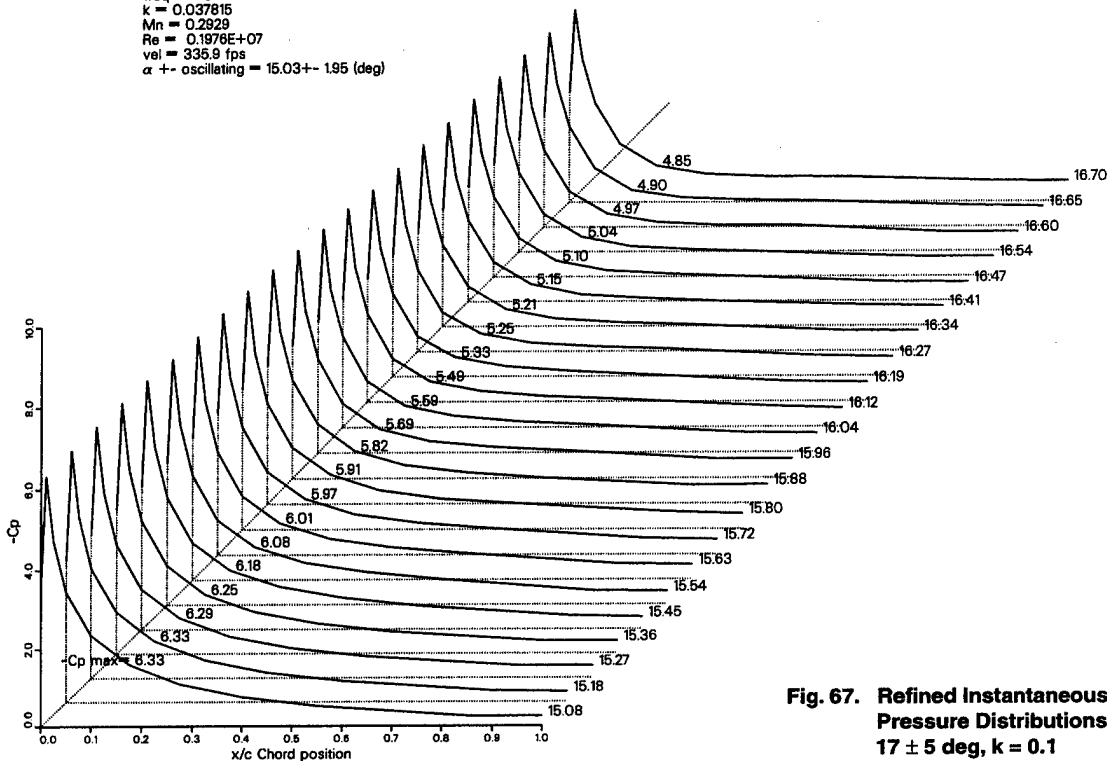


Fig. 66a

Fig. 66. Comparison of Lift and Pitching Moment vs. Angle  
 $15 \pm 2$  deg,  $k = 0.14$

Upper Pressure vs. Chord Position  
Data Point : 2DPOT1.PM775, 50.0% Span

freq = 4.04 hz  
k = 0.037815  
Mn = 0.2929  
Re = 0.1976E+07  
vel = 335.9 fps  
 $\alpha \pm$  oscillating = 15.03 $\pm$  1.95 (deg)



**Fig. 67. Refined Instantaneous Pressure Distributions**  
 **$17 \pm 5$  deg,  $k = 0.1$**

Upper Surface Pressure vs. Chord Position  
Data Point : 2DPOT1.PM777 , (50.0% Span)

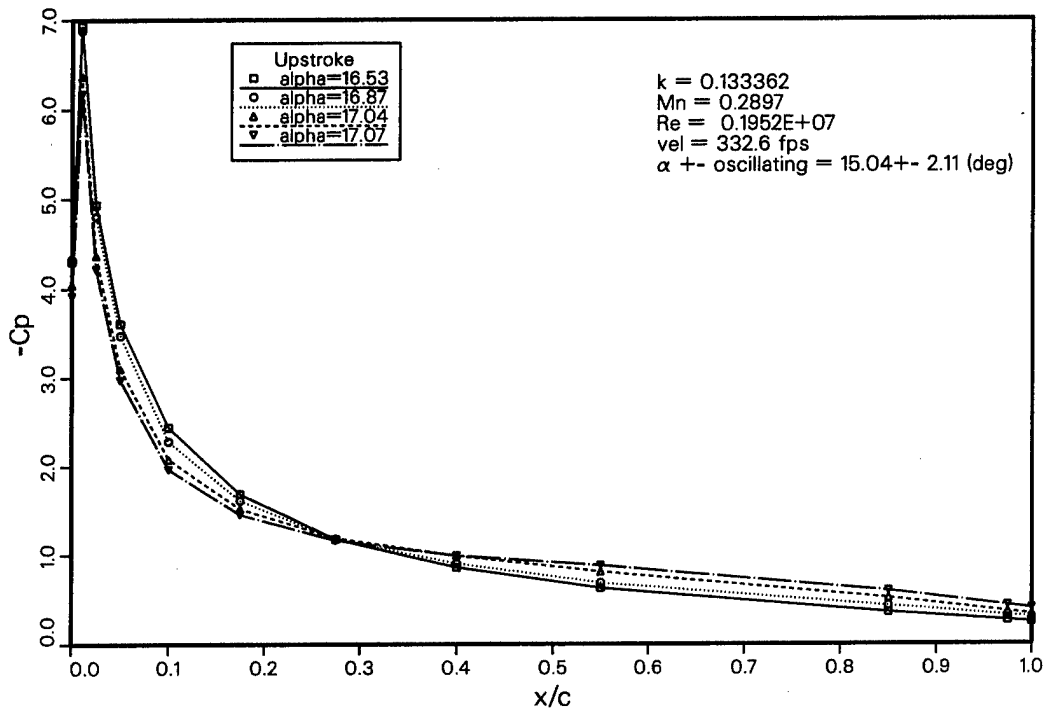


**Fig. 68. Upper Surface Pressure vs. Chord Position**  
**15 ± 2 deg, k = 0.14**

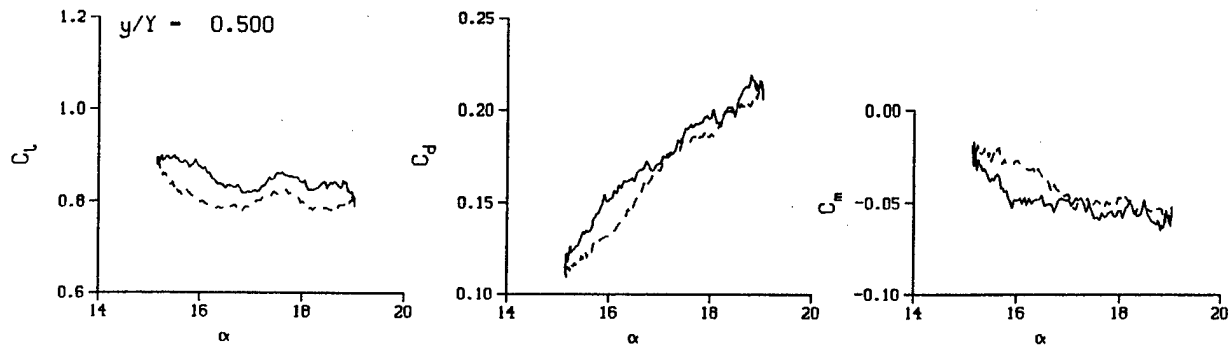


Fig. 69a

DataPointID: 2DPOT1.R0780

$\alpha = 17.09 \pm 1.97$  Deg.

$\nu = 0.038$

*note: different y-axis scale*

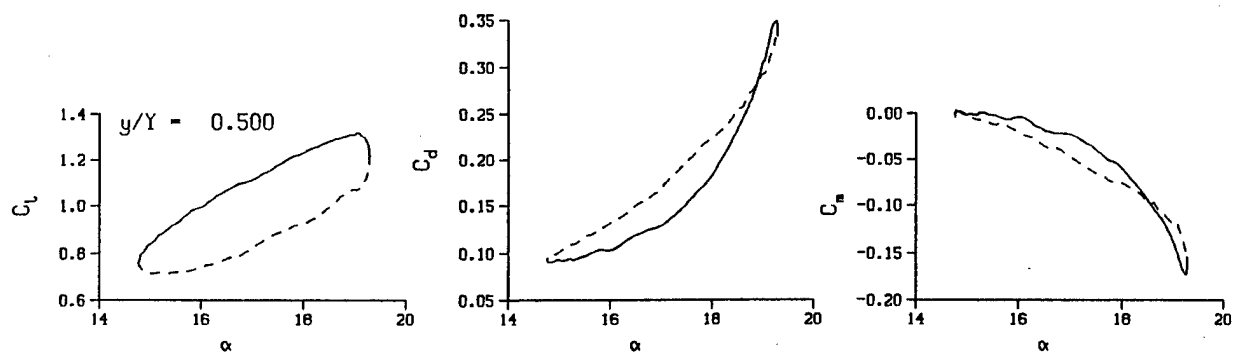


Fig. 69b

DataPointID: 2DPOT1.R0783

$\alpha = 17.09 \pm 2.26$  Deg.

$\nu = 0.191$

Fig. 69. Lift, drag, and pitching moment for  $17 \pm 2$  deg at different reduced frequencies (*ref. 1*)

Upper Pressure vs. Chord Position  
Data Point : 2DPOT1.PM780, 50.0% Span

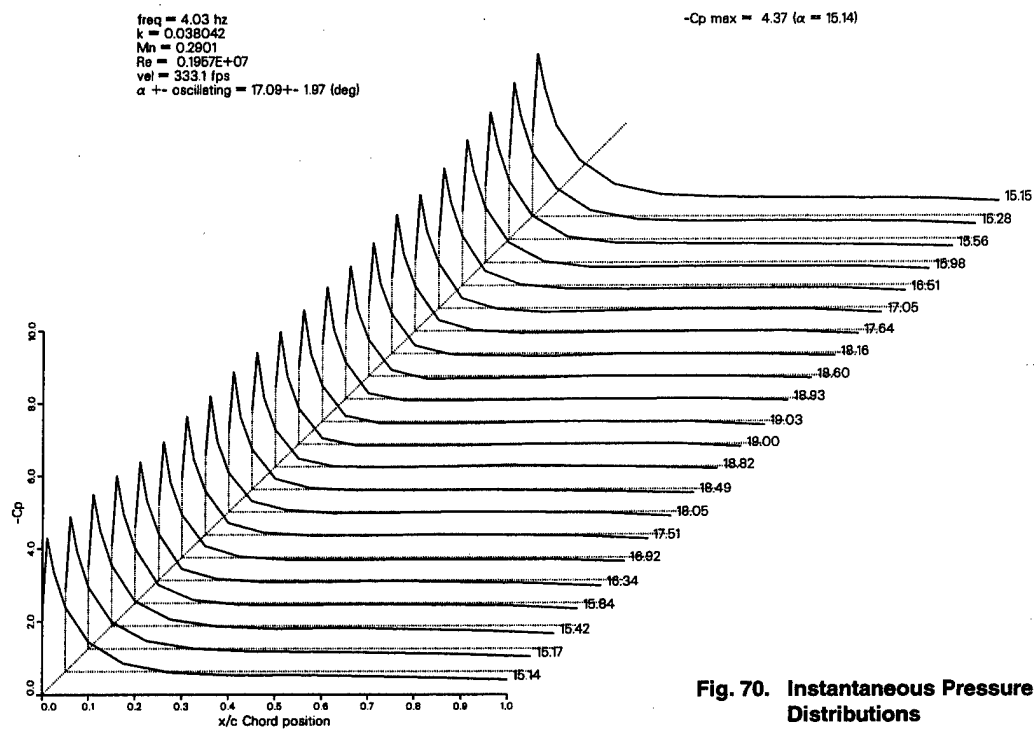


Fig. 70. Instantaneous Pressure  
Distributions  
 $17 \pm 2$  deg,  $k = 0.04$

Upper Surface Pressure vs. Chord Position  
Data Point : 2DPOT1.PM780 , (50.0% Span)

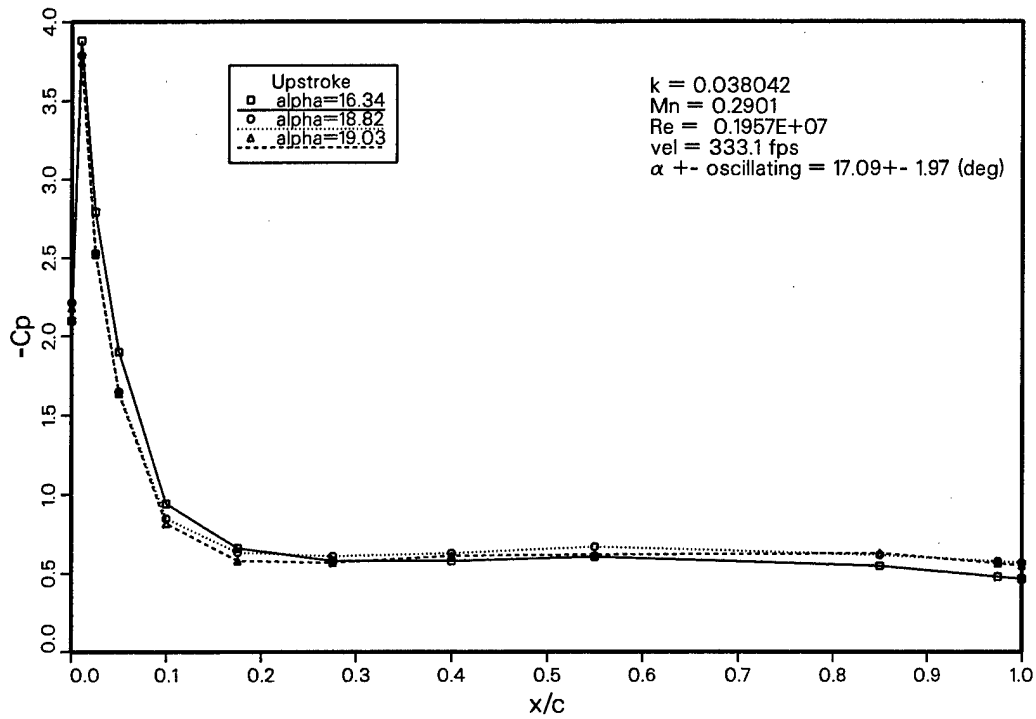


Fig. 71. Upper Surface Pressure vs. Chord Position  
 $17 \pm 2 \text{ deg}$ ,  $k = 0.04$

Upper Surface Pressure vs. Chord Position  
Data Point : 2DPOT1.PM780 , (50.0% Span)

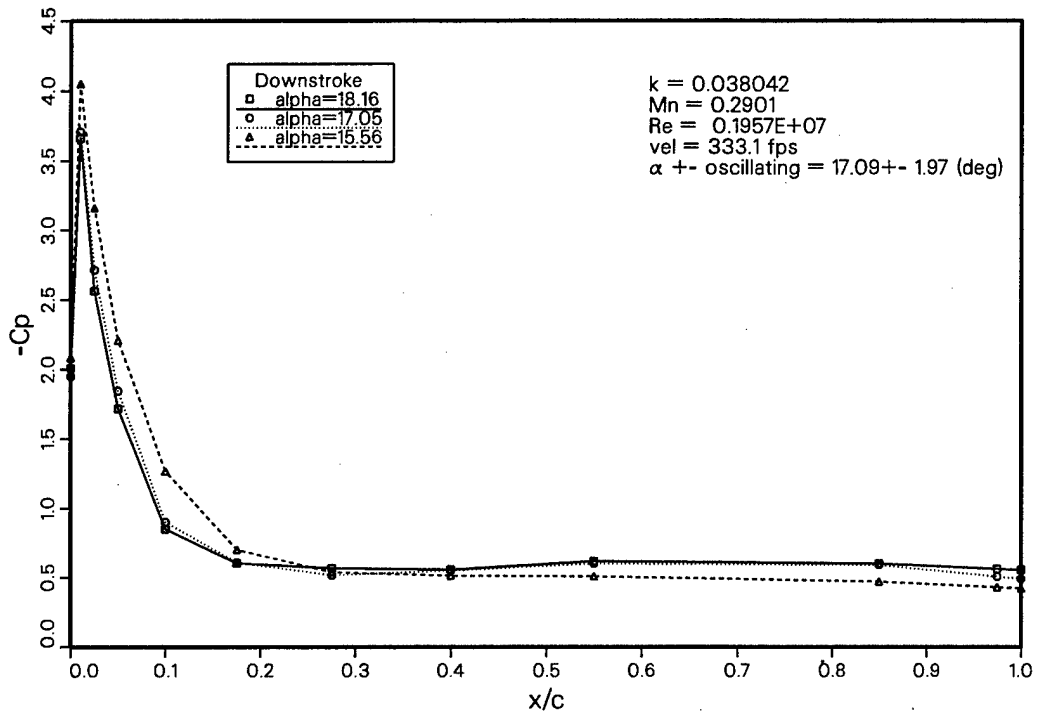
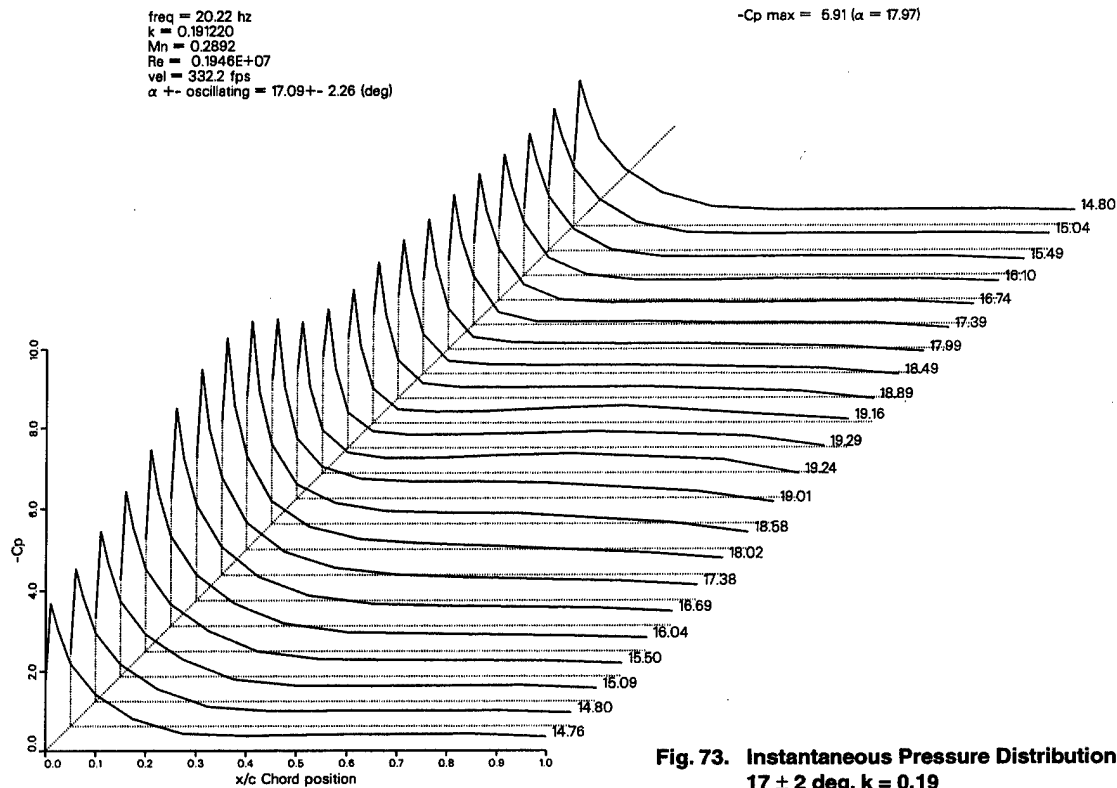


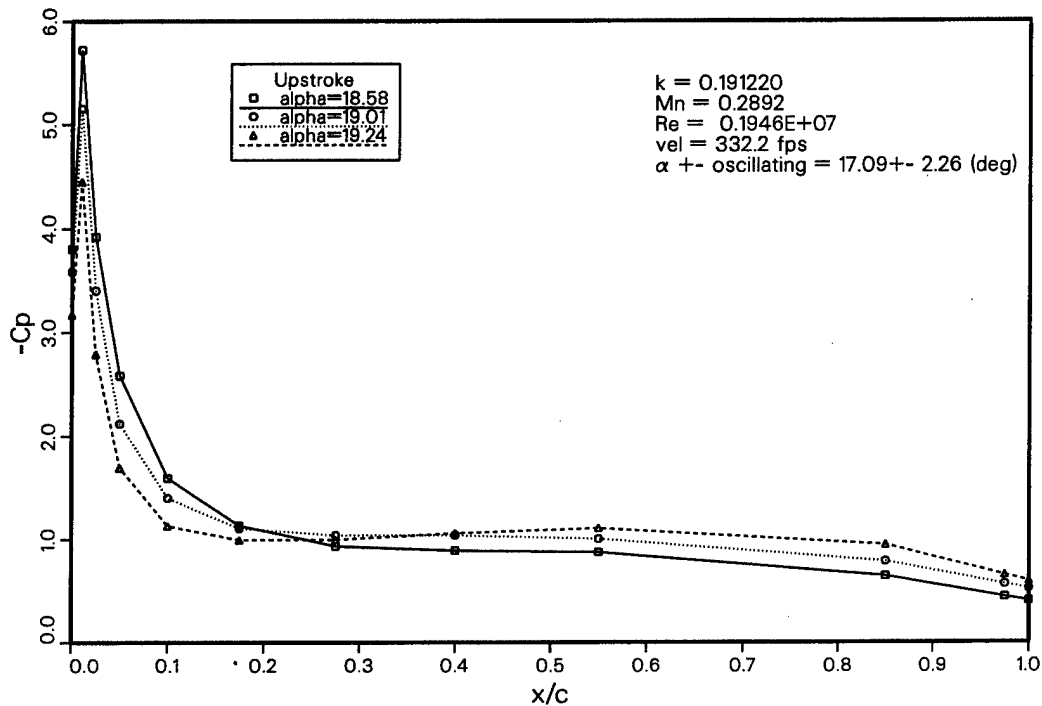
Fig. 72. Upper Surface Pressure vs. Chord Position  
 $17 \pm 2 \text{ deg}$ ,  $k = 0.04$



Upper Pressure vs. Chord Position  
Data Point : 2DPOT1.PM783, 50.0% Span



Upper Surface Pressure vs. Chord Position  
Data Point : 2DPOT1.PM783 , (50.0% Span)



Comparison of Lift Coefficient vs.  $\alpha$   
Data Points: 2DPOT1.R0780 and 2DQST1.R0885 (50.0 % Span)

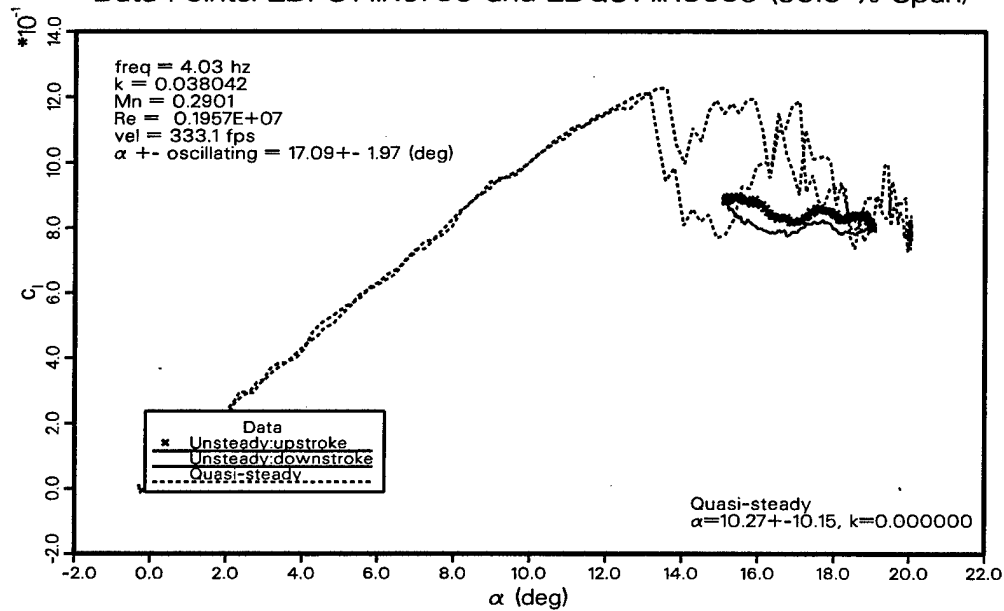


Fig. 75a

Comparison of Pitching Moment Coefficient vs.  $\alpha$   
Data Points: 2DPOT1.R0780 and 2DQST1.R0885 (50.0 % Span)

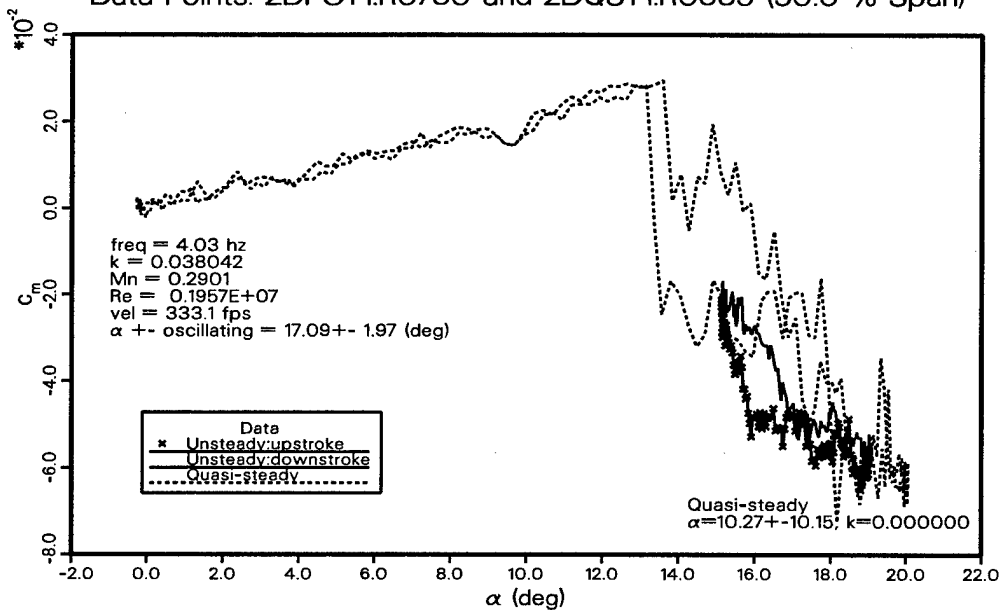


Fig. 75b

Fig. 75. Comparison of Lift and Pitching Moment vs. Angle  
 $17 \pm 2$  deg,  $k = 0.04$

Comparison of Lift Coefficient vs.  $\alpha$   
Data Points: 2DPOT1.R0783 and 2DQST1.R0885 (50.0 % Span)

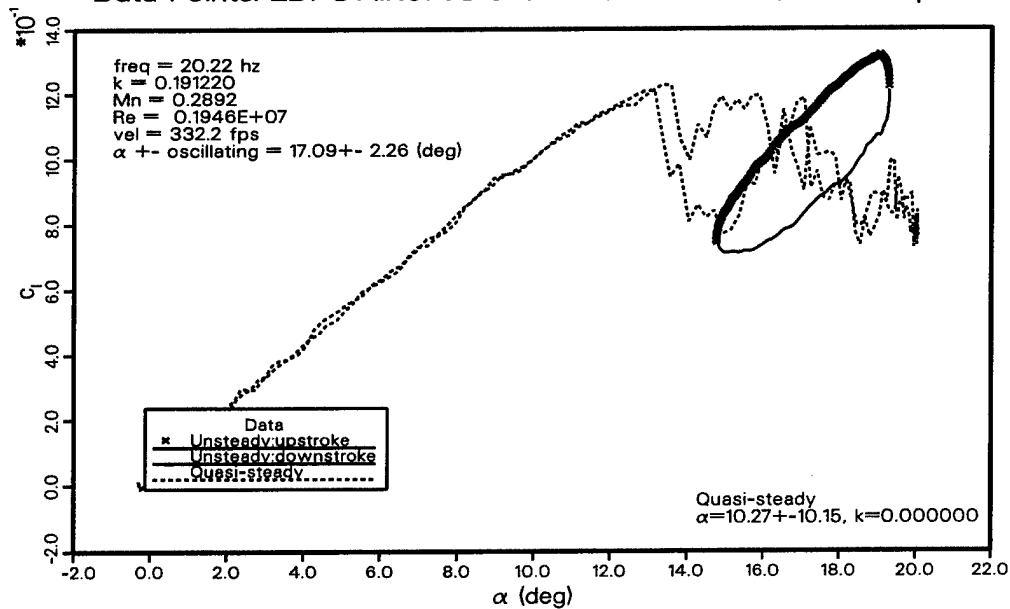


Fig. 76a

Comparison of Pitching Moment Coefficient vs.  $\alpha$   
Data Points: 2DPOT1.R0783 and 2DQST1.R0885 (50.0 % Span)

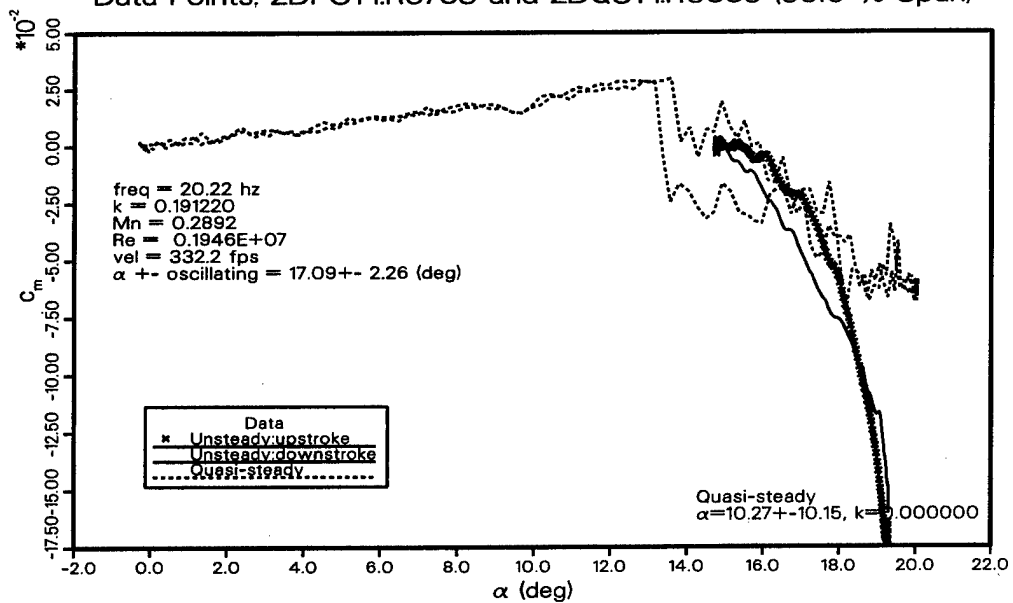
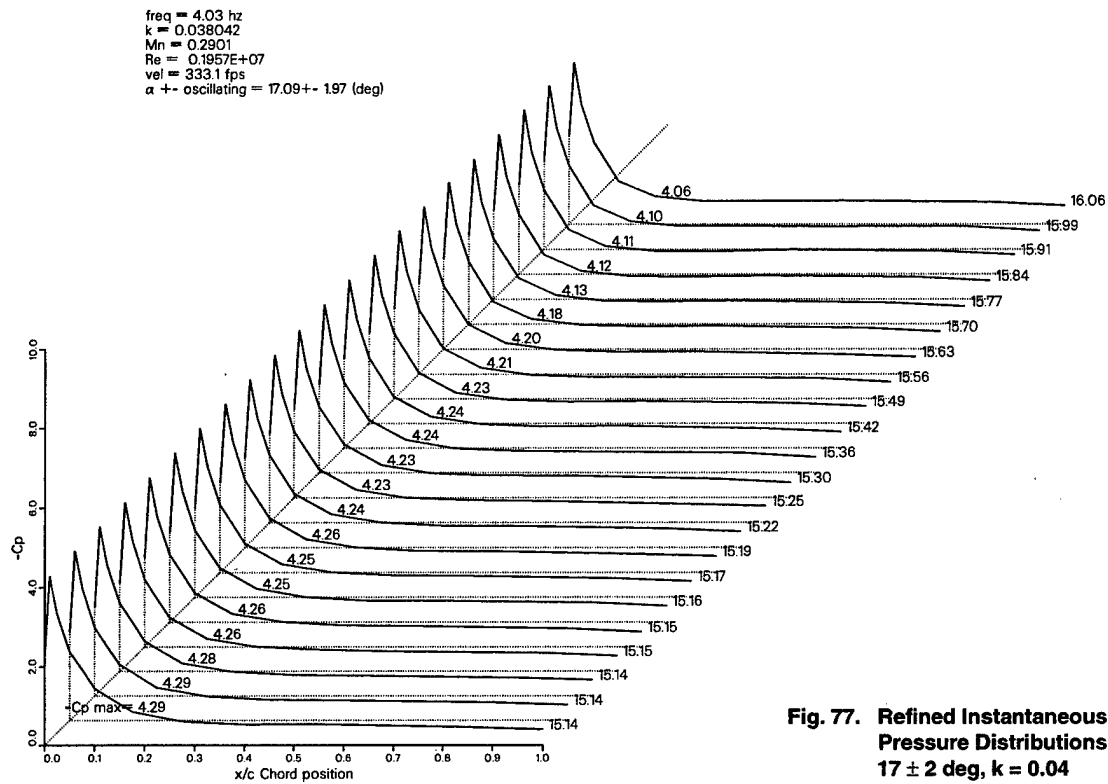


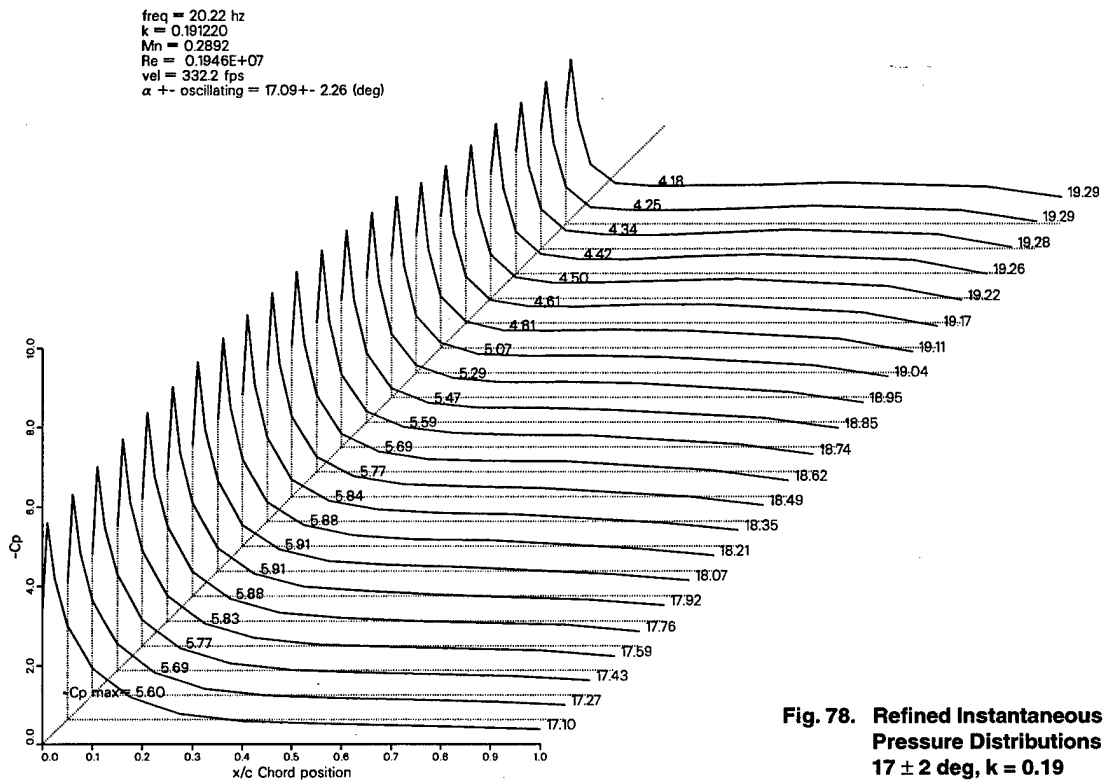
Fig. 76b

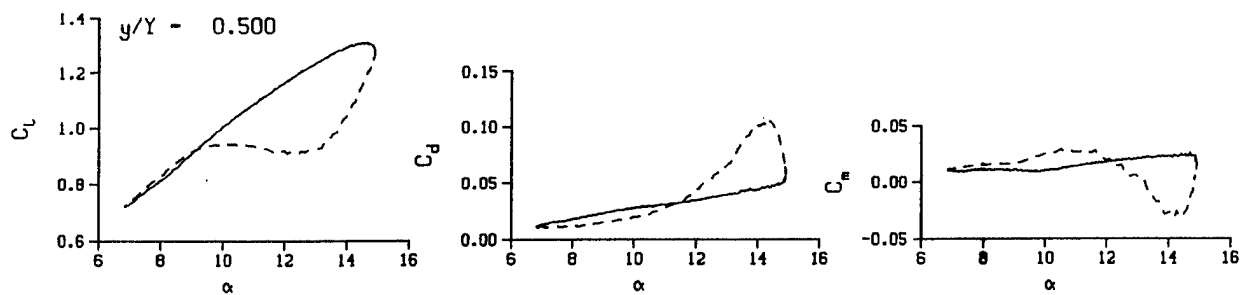
Fig. 76. Comparison of Lift and Pitching Moment vs. Angle  
 $17 \pm 2$  deg,  $k = 0.19$

Upper Pressure vs. Chord Position  
Data Point : 2DPOT1.PM780, 50.0% Span



Upper Pressure vs. Chord Position  
Data Point : 2DPOT1.PM783, 50.0% Span

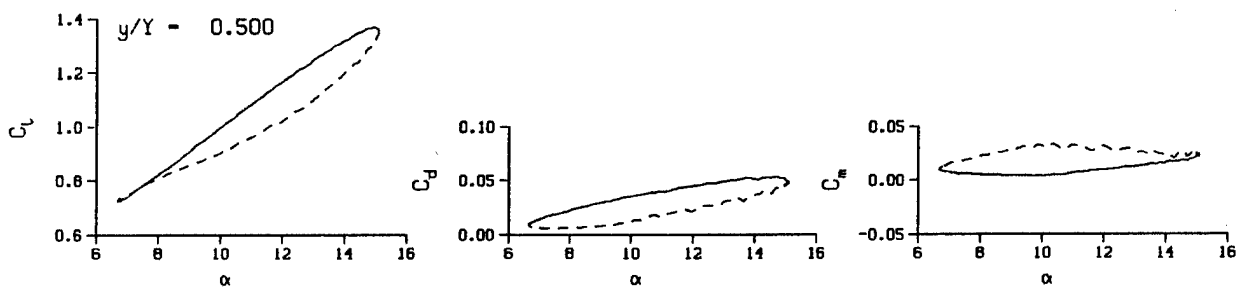




DataPointID: 2DPOT1.R0797

$\alpha = 10.88 \pm 4.07$  Deg.

$\nu = 0.038$



DataPointID: 2DPOT1.R0798

$\alpha = 10.88 \pm 4.22$  Deg.

$\nu = 0.095$

Fig. 79. Lift, drag, and pitching moment for  $11 \pm 4$  deg at different reduced frequencies (ref. 1)

Upper Pressure vs. Chord Position  
Data Point : 2DPOT1.PM797, 50.0% Span

freq = 4.04 hz  
k = 0.038010  
Mn = 0.2908  
Re = 0.1956E+07  
vel = 333.9 fps  
 $\alpha$  +- oscillating = 10.88+- 4.07 (deg)

-Cp max = 6.60 ( $\alpha$  = 14.82)

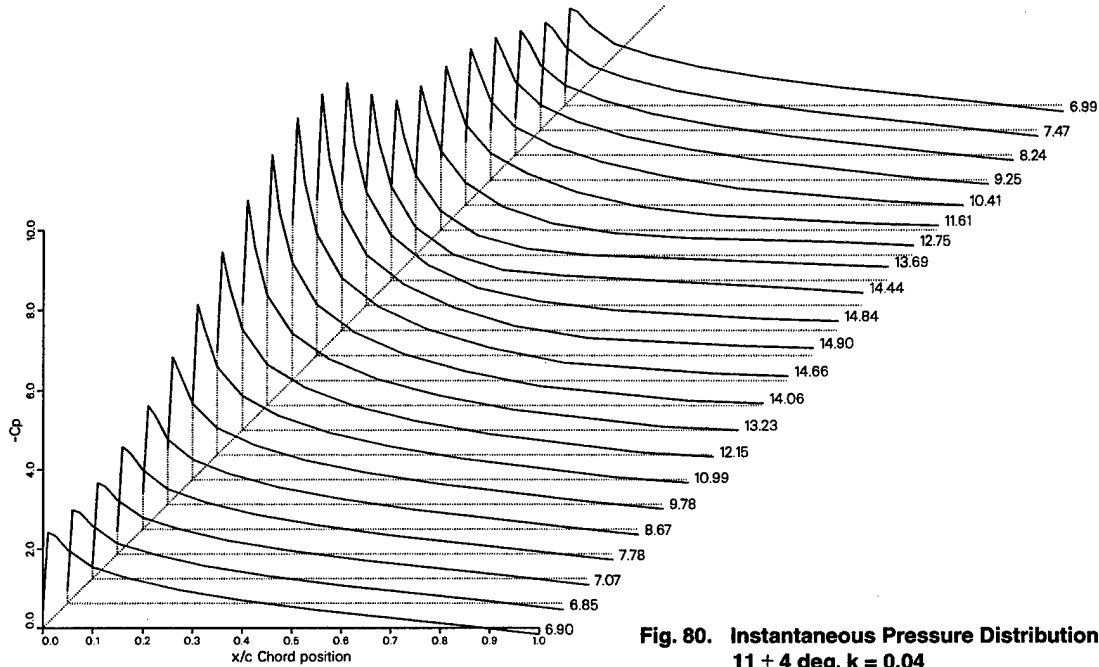


Fig. 80. Instantaneous Pressure Distributions  
 $11 \pm 4$  deg,  $k = 0.04$

Upper Surface Pressure vs. Chord Position  
Data Point : 2DPOT1.PM797 , (50.0% Span)

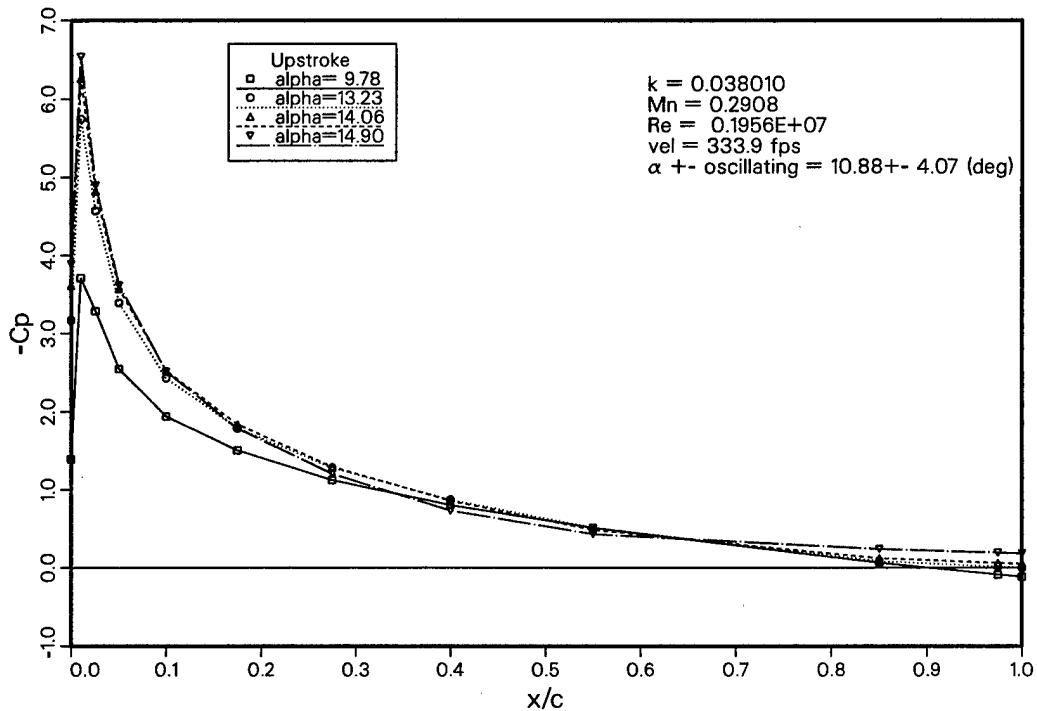
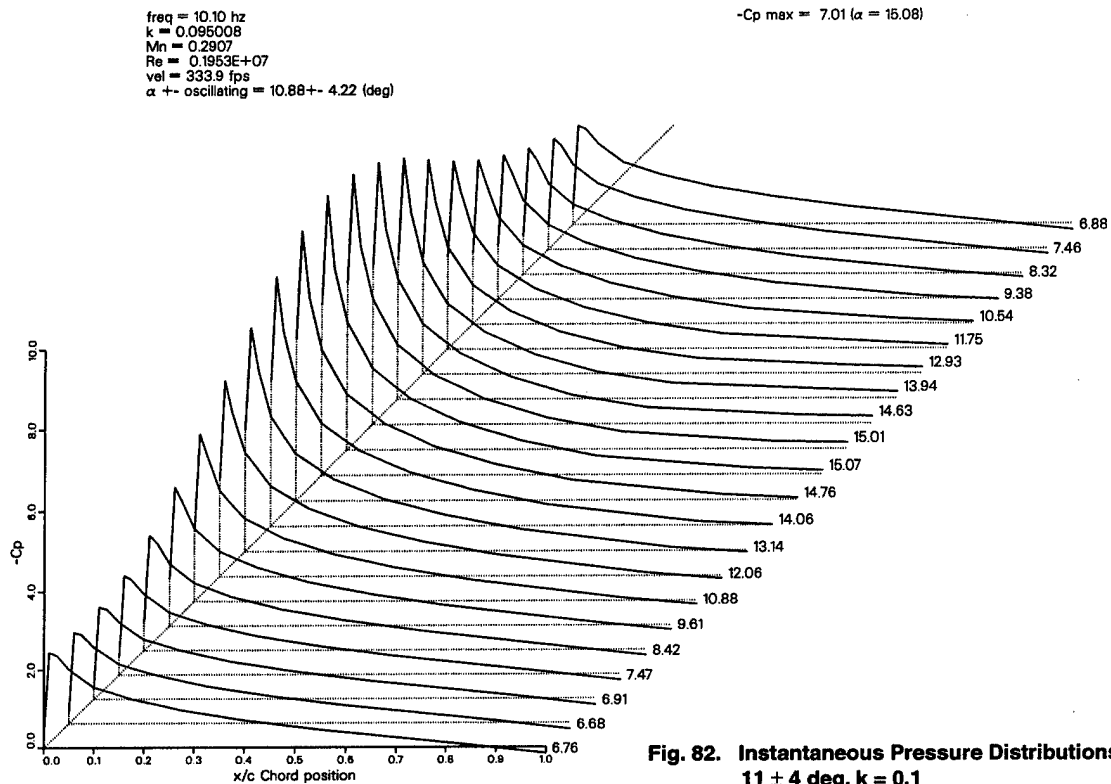
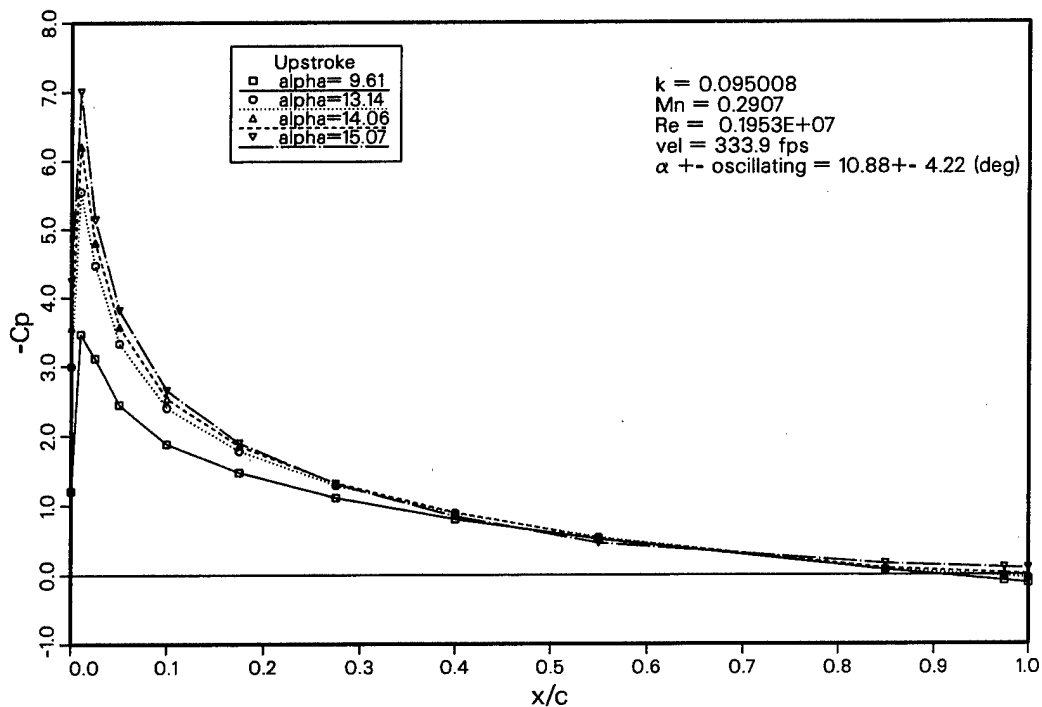


Fig. 81. Upper Surface Pressure vs. Chord Positions  
 $11 \pm 4$  deg,  $k = 0.04$

Upper Pressure vs. Chord Position  
Data Point : 2DPOT1.PM798, 50.0% Span



Upper Surface Pressure vs. Chord Position  
Data Point : 2DPOT1.PM798 , (50.0% Span)



Comparison of Lift Coefficient vs.  $\alpha$   
Data Points: 2DPOT1.R0797 and 2DQST1.R0885 (50.0 % Span)

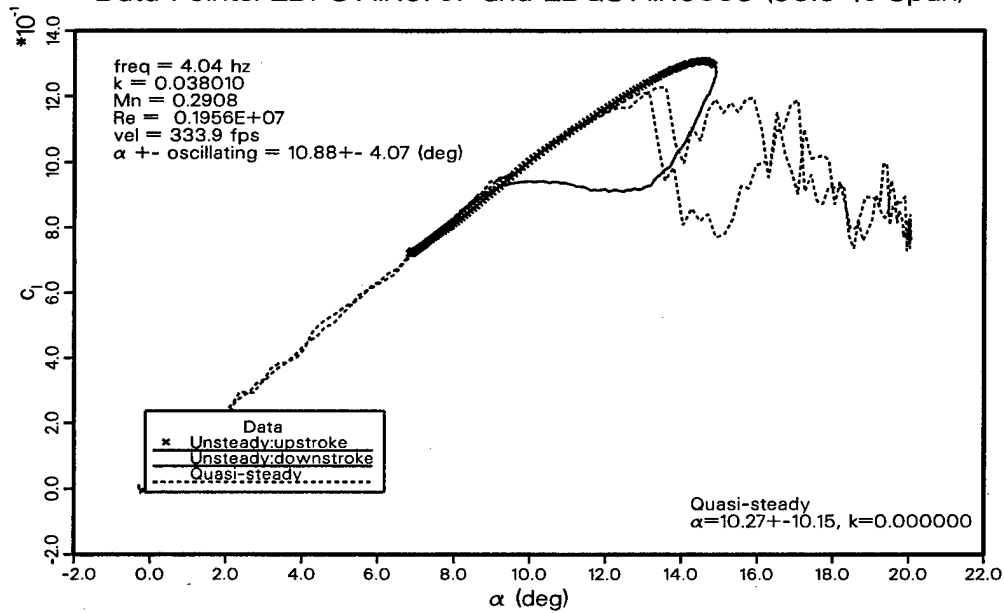


Fig. 84a

Comparison of Pitching Moment Coefficient vs.  $\alpha$   
Data Points: 2DPOT1.R0797 and 2DQST1.R0885 (50.0 % Span)

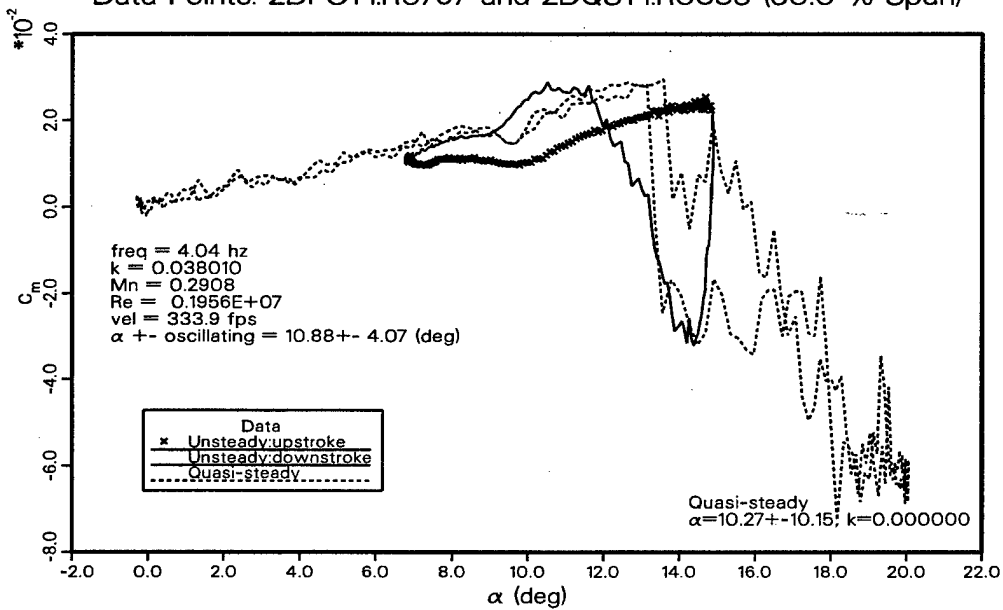


Fig. 84b

Fig. 84. Comparison of Lift and Pitch Moment vs. Angle  
 $11 \pm 4$  deg,  $k = 0.04$



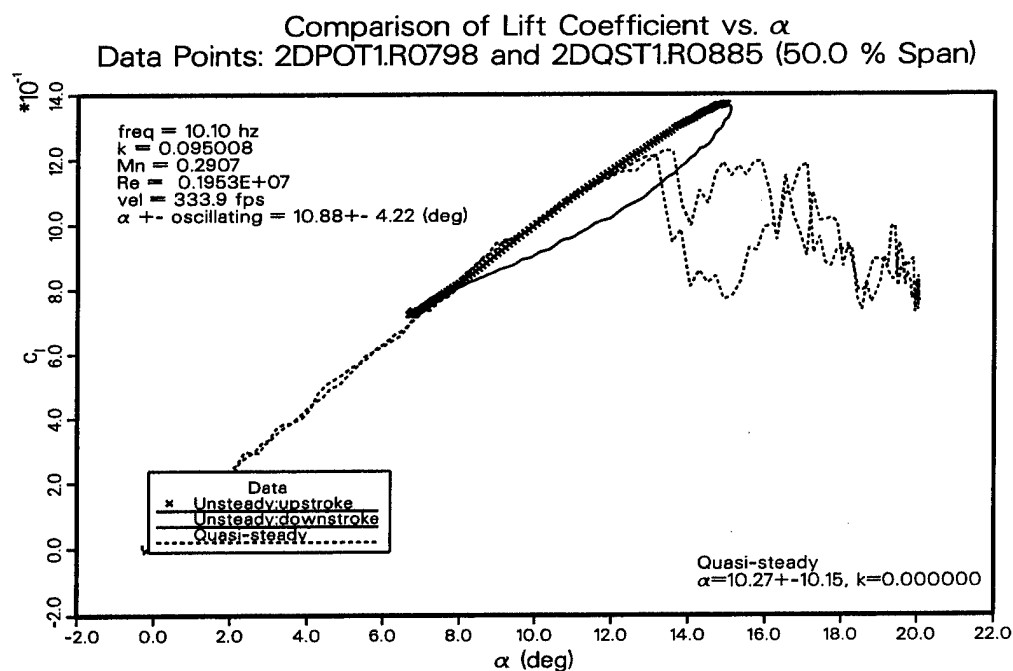


Fig. 85a

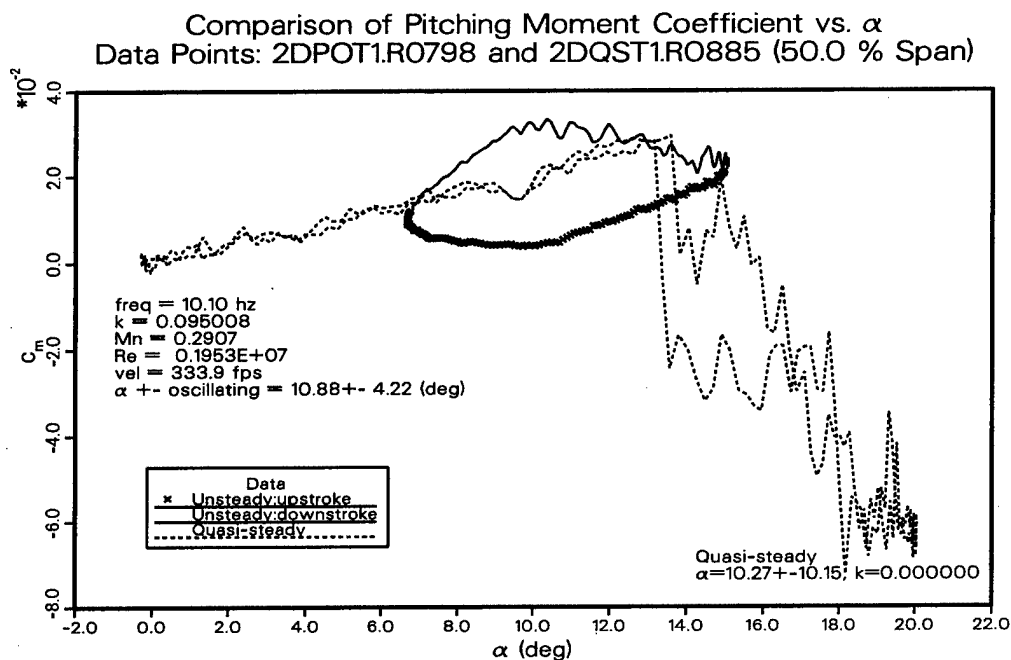


Fig. 85b

Fig. 85. Comparison of Lift and Pitching Moment vs. Angle  
 $11 \pm 4$  deg, k = 0.1

Upper Pressure vs. Chord Position  
Data Point : 2DPOT1.PM797, 50.0% Span

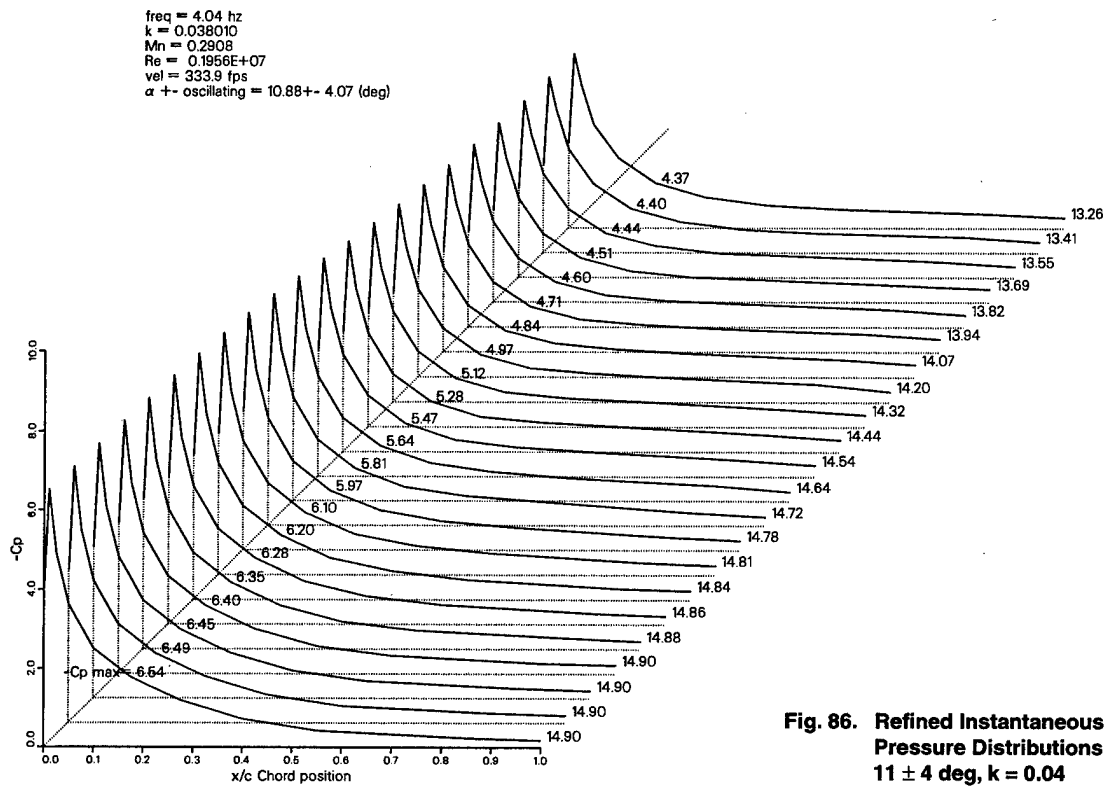
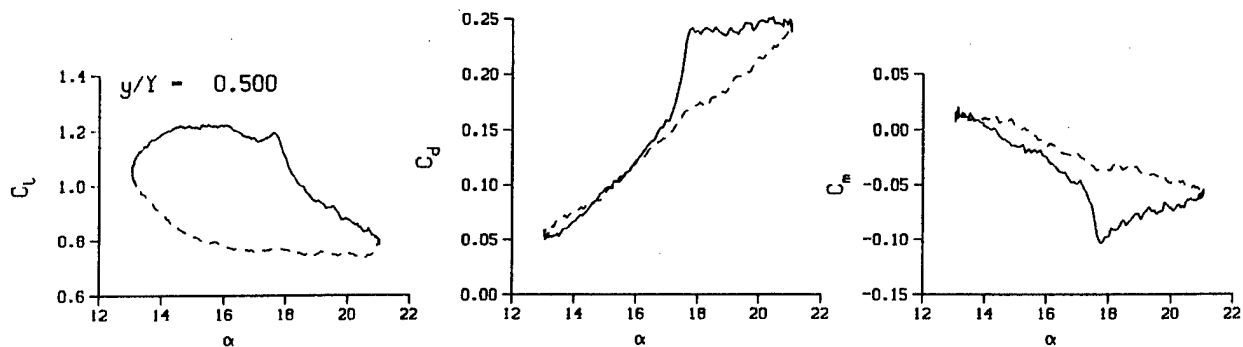


Fig. 86. Refined Instantaneous  
Pressure Distributions  
 $11 \pm 4$  deg,  $k = 0.04$

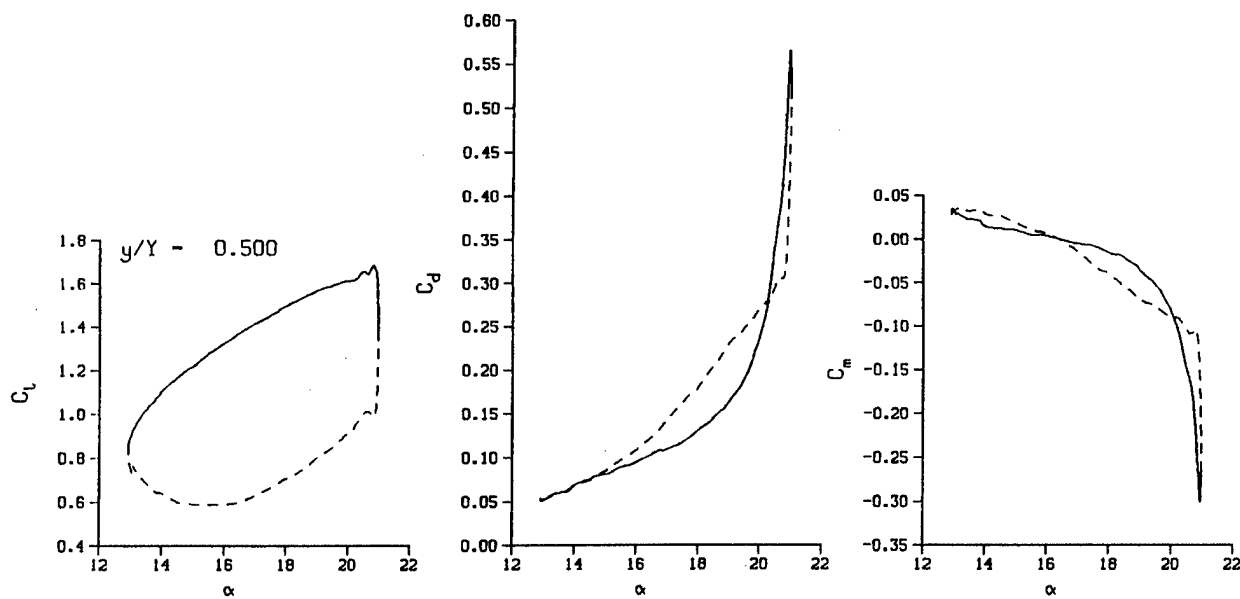


DataPointID: 2DPOT1.R0809

$\alpha = 17.05 \pm 4.03$  Deg.

$\nu = 0.038$

*note: different y-axis scale*



DataPointID: 2DPOT1.R0811

$\alpha = 17.04 \pm 4.27$  Deg.

$\nu = 0.134$

Fig. 87. Lift, drag, and pitching moment for  $17 \pm 2$  deg at different reduced frequencies (ref. 1)

Upper Pressure vs. Chord Position  
Data Point : 2DPOT1.PM809, 50.0% Span

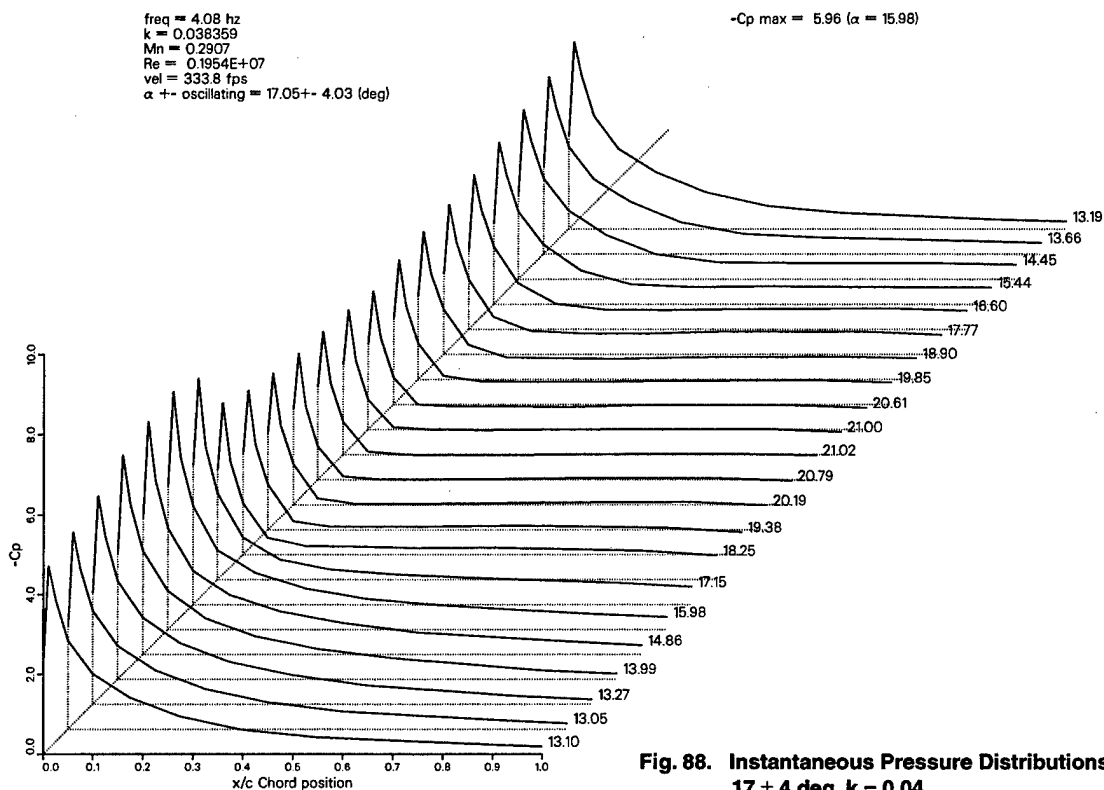


Fig. 88. Instantaneous Pressure Distributions  
 $17 \pm 4$  deg,  $k = 0.04$

Upper Surface Pressure vs. Chord Position  
Data Point : 2DPOT1.PM809 , (50.0% Span)

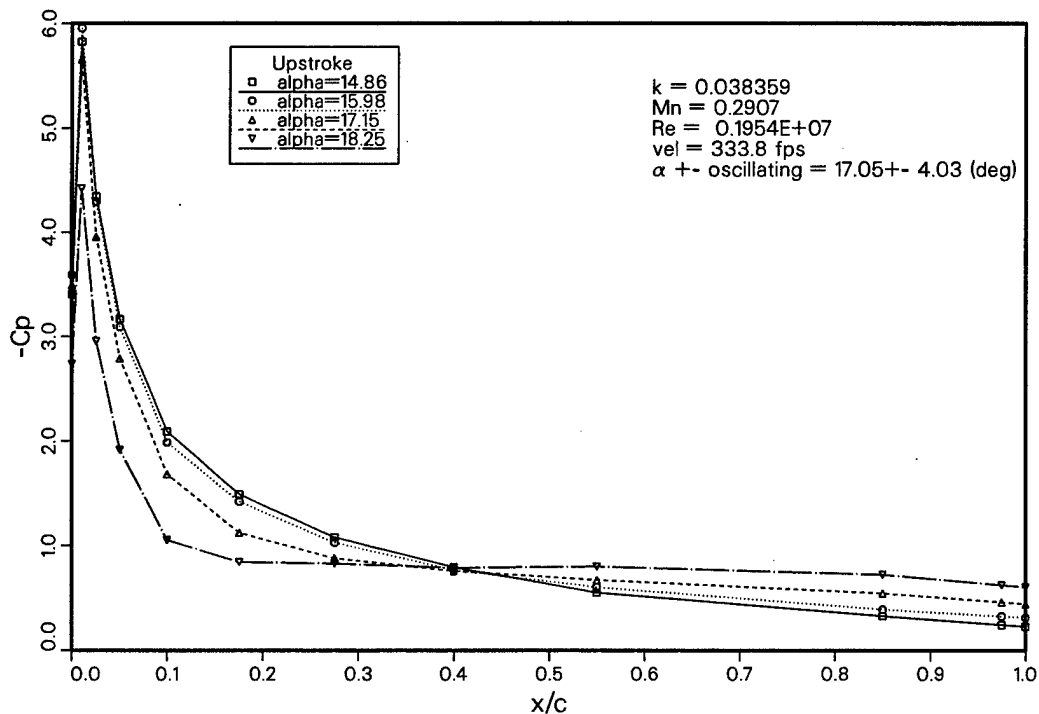


Fig. 89. Upper Surface Pressure vs. Chord Position  
 $17 \pm 4$  deg,  $k = 0.04$

Upper Surface Pressure vs. Chord Position  
Data Point : 2DPOT1.PM809 , (50.0% Span)

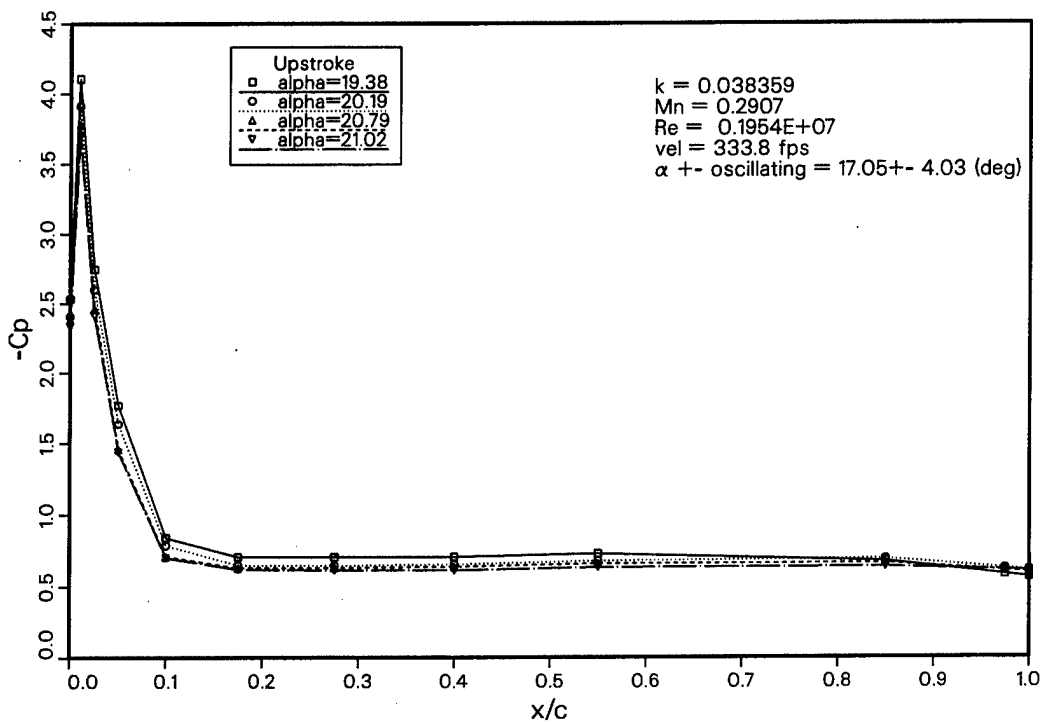


Fig. 90. Upper Surface Pressure vs. Chord Position  
 $17 \pm 4 \text{ deg}$ ,  $k = 0.04$  at different angles

Upper Surface Pressure vs. Chord Position  
Data Point : 2DPOT1.PM809 , (50.0% Span)

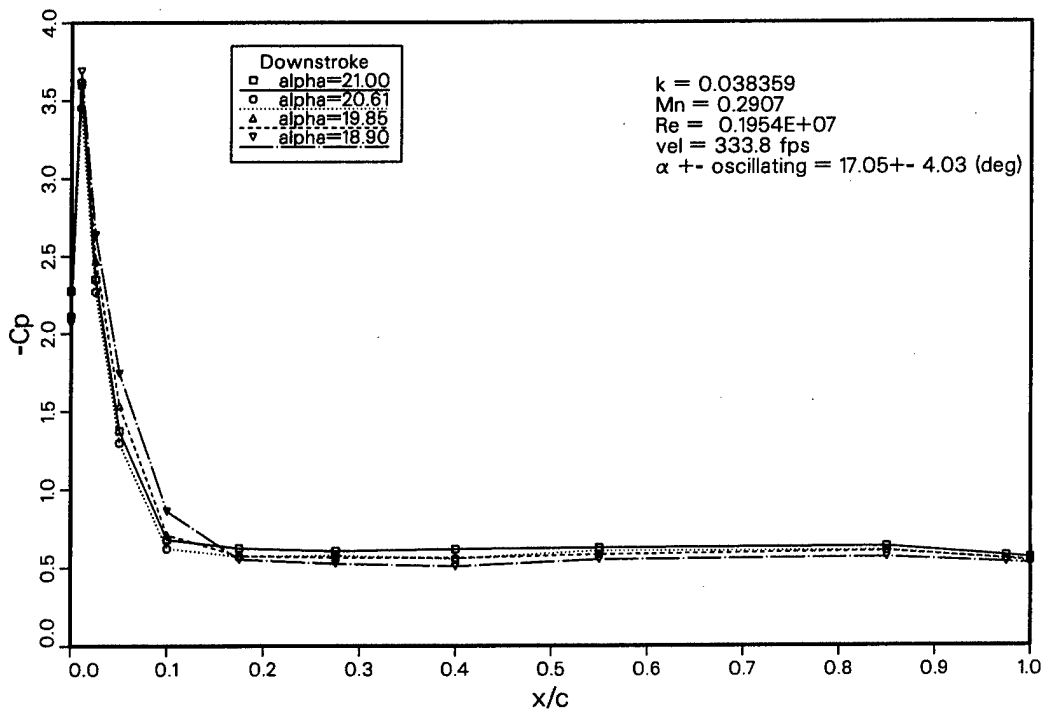
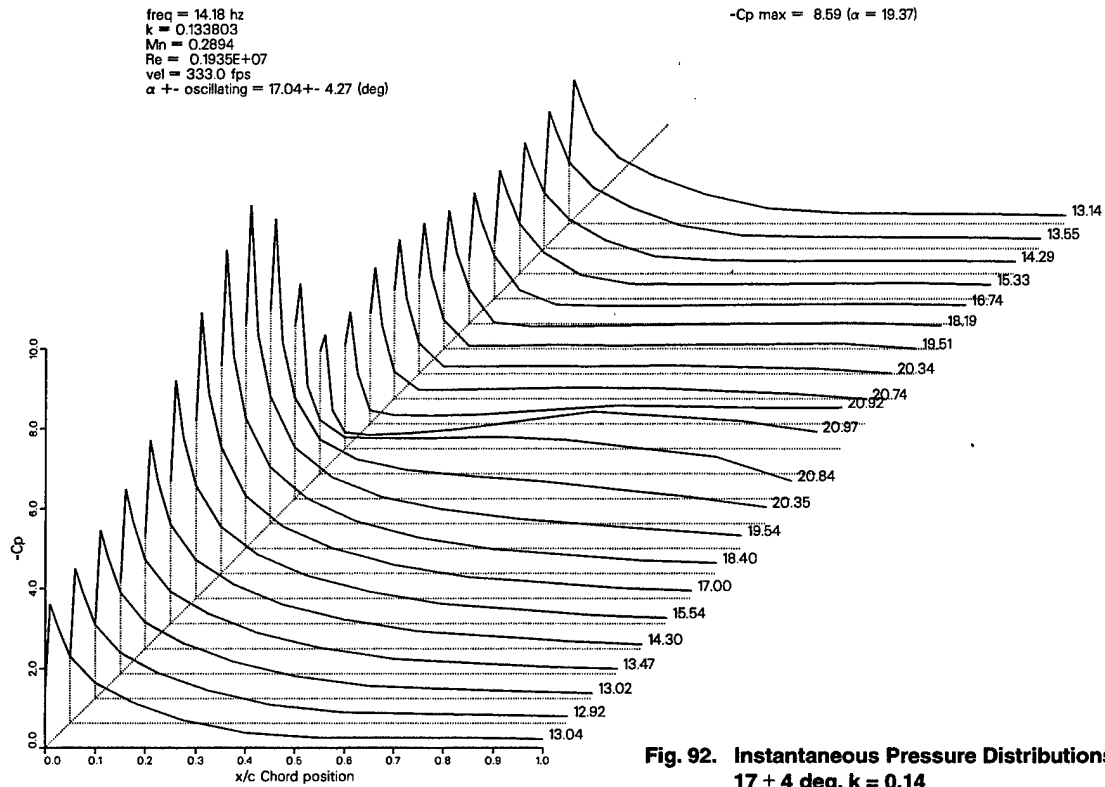
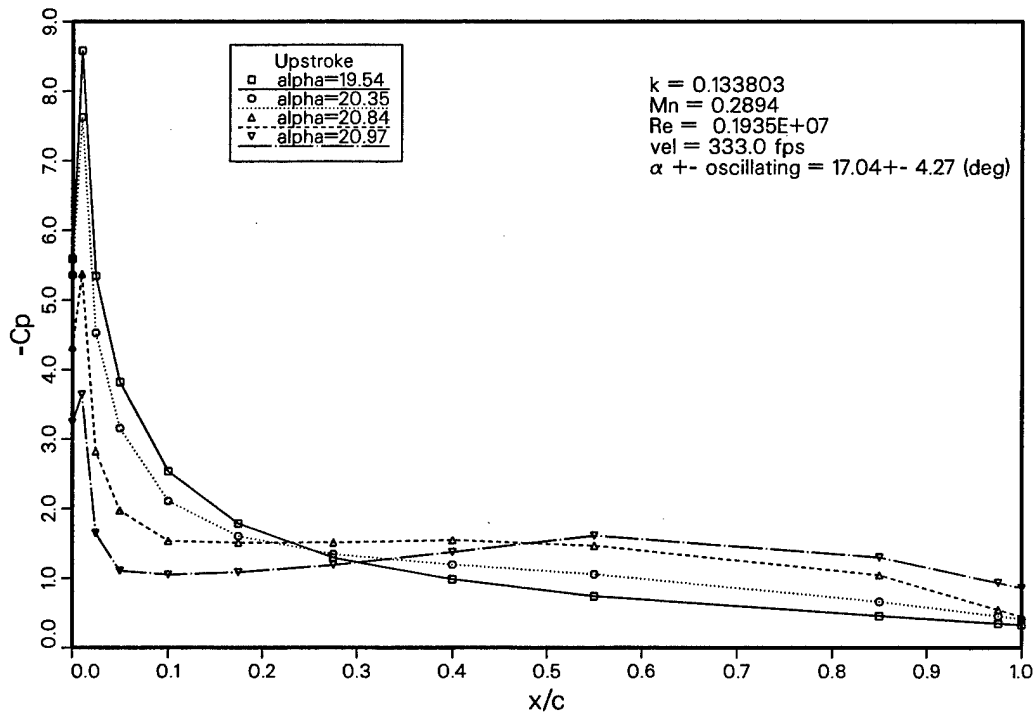


Fig. 91. Upper Surface Pressure vs. Chord Position  
 $17 \pm 4 \text{ deg}$ ,  $k = 0.04$  at different downstroke angles

Upper Pressure vs. Chord Position  
Data Point : 2DPOT1.PM811, 50.0% Span



Upper Surface Pressure vs. Chord Position  
Data Point : 2DPOT1.PM811 , (50.0% Span)



Comparison of Lift Coefficient vs.  $\alpha$   
Data Points: 2DPOT1.R0809 and 2DQST1.R0885 (50.0 % Span)

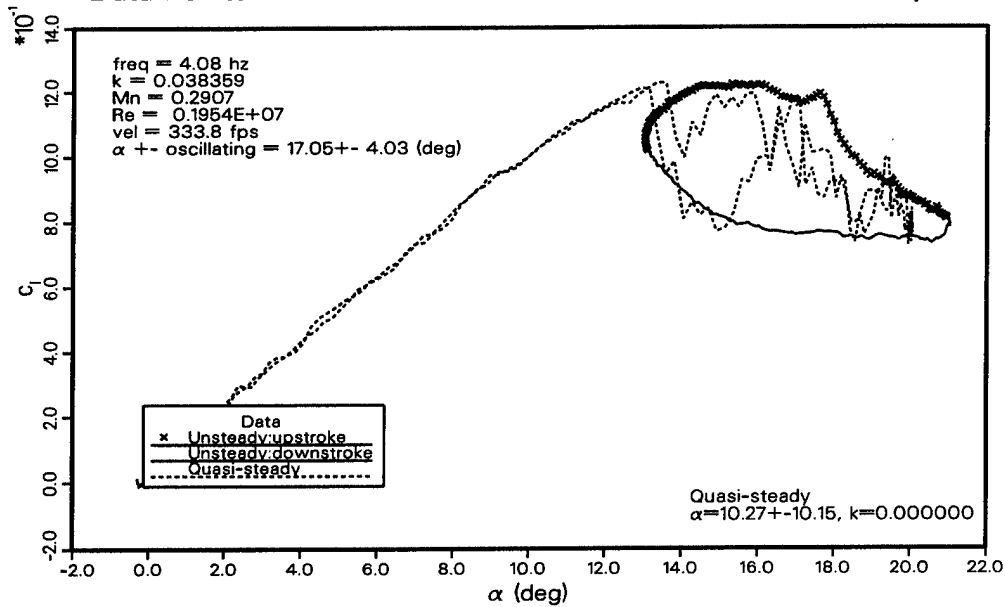


Fig. 94a

Comparison of Pitching Moment Coefficient vs.  $\alpha$   
Data Points: 2DPOT1.R0809 and 2DQST1.R0885 (50.0 % Span)

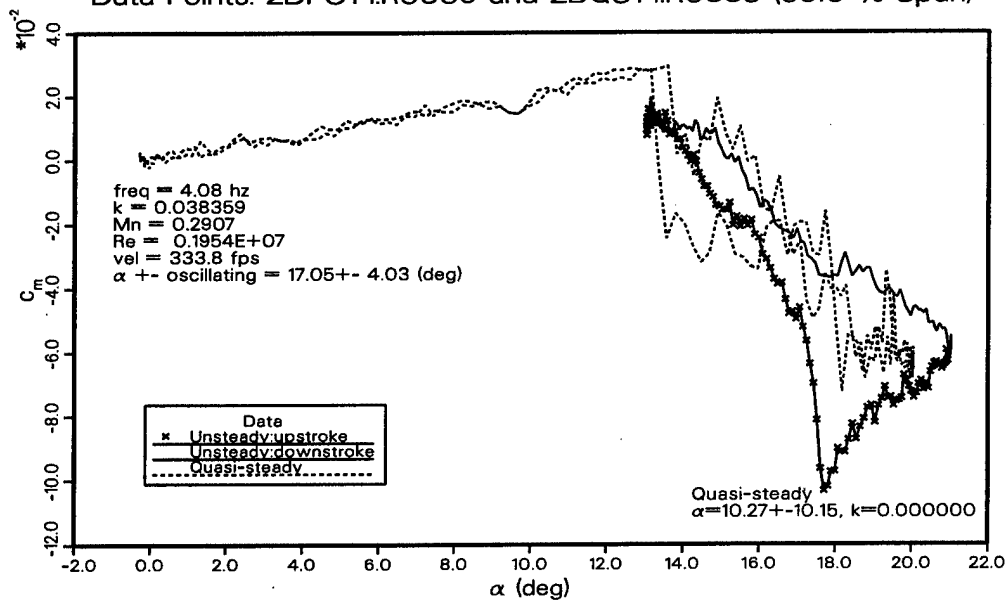


Fig. 94b

Fig. 94. Comparison of Lift and Pitching Moment vs. Angle  
 $17 \pm 4$  deg, k = 0.04

Comparison of Lift Coefficient vs.  $\alpha$   
Data Points: 2DPOT1.R0811 and 2DQST1.R0885 (50.0 % Span)

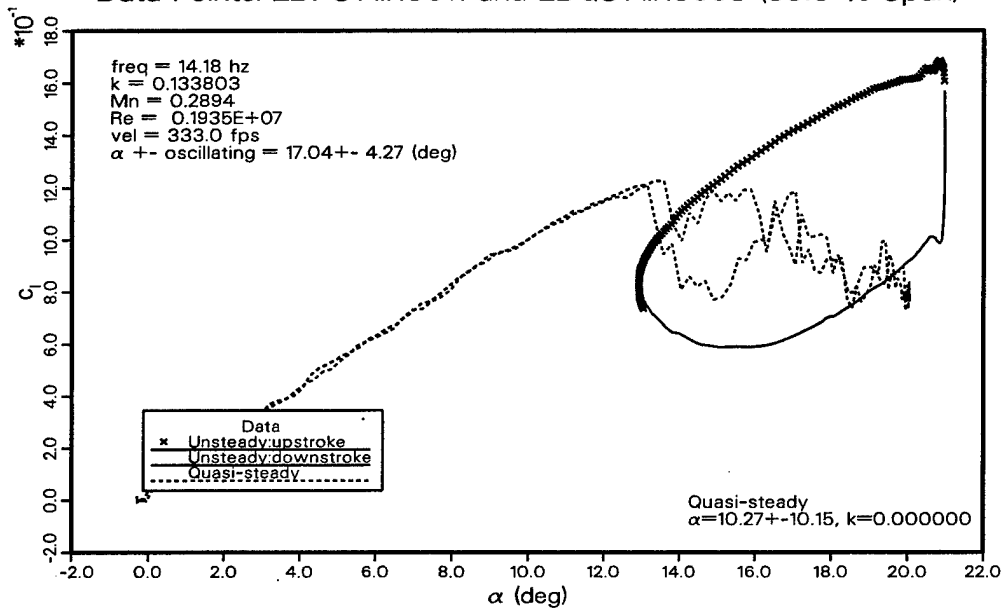


Fig. 95a

Comparison of Pitching Moment Coefficient vs.  $\alpha$   
Data Points: 2DPOT1.R0811 and 2DQST1.R0885 (50.0 % Span)

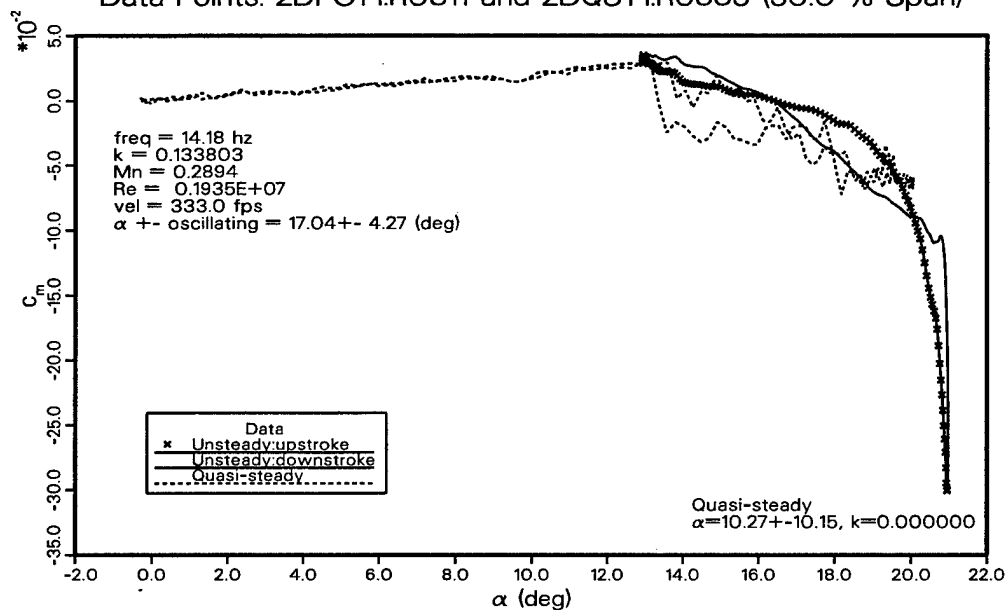
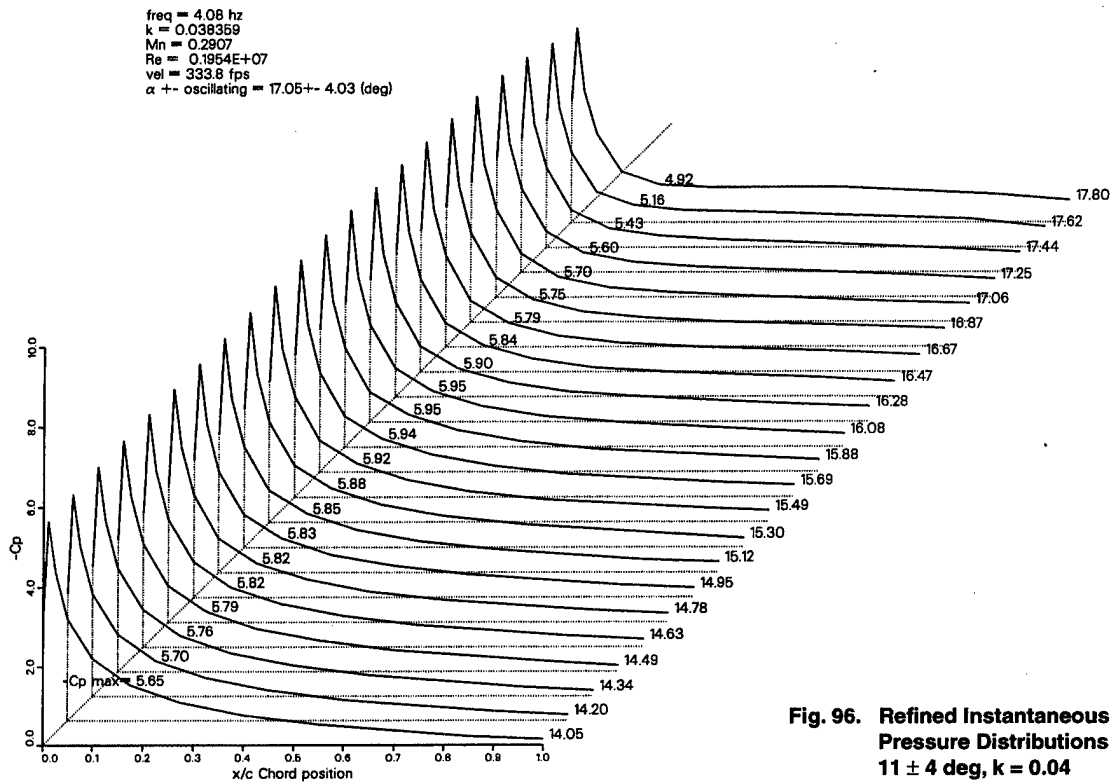


Fig. 95b

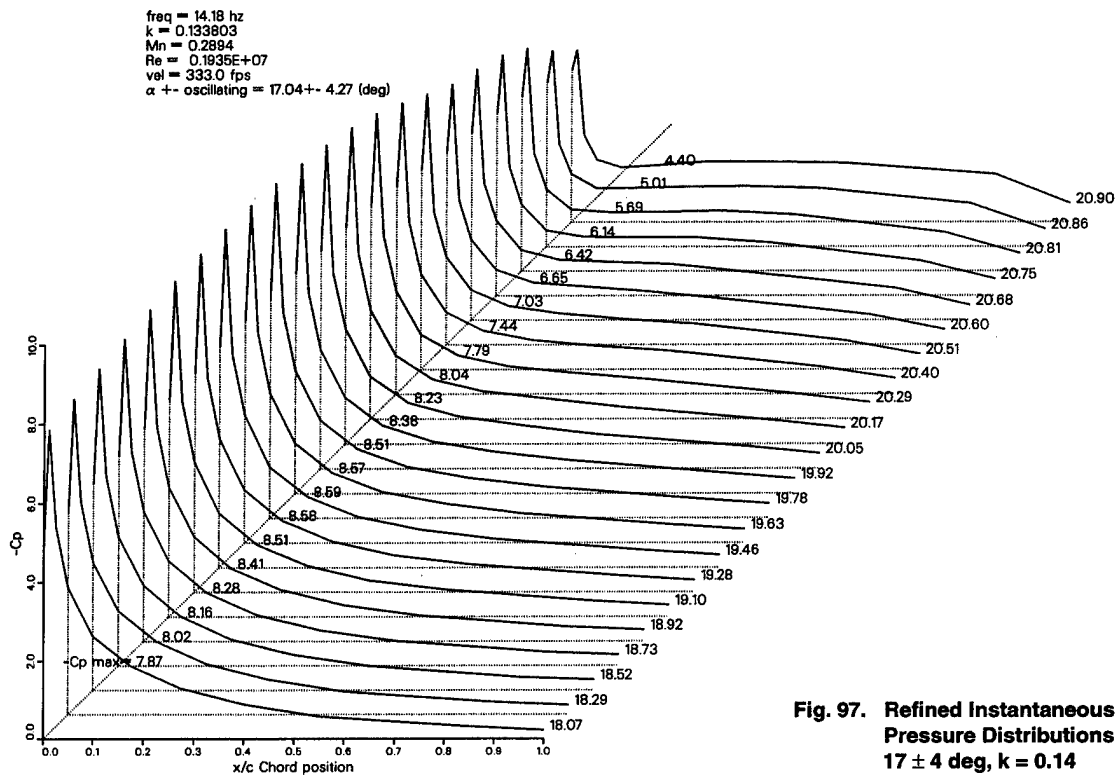
Fig. 95. Comparison of Lift and Pitching Moment vs. Angle  
 $17 \pm 4$  deg, k = 0.14



Upper Pressure vs. Chord Position  
Data Point : 2DPOT1.PM809, 50.0% Span



Upper Pressure vs. Chord Position  
Data Point : 2DPOT1.PM811, 50.0% Span



**REPORT DOCUMENTATION PAGE**Form Approved  
OMB No. 0704-0188

Public reporting burden for this collection of information is estimated to average 1 hour per response, including the time for reviewing instructions, searching existing data sources, gathering and maintaining the data needed, and completing and reviewing the collection of information. Send comments regarding this burden estimate or any other aspect of this collection of information, including suggestions for reducing this burden, to Washington Headquarters Services, Directorate for Information Operations and Reports, 1215 Jefferson Davis Highway, Suite 1204, Arlington, VA 22202-4302, and to the Office of Management and Budget, Paperwork Reduction Project (0704-0188), Washington, DC 20503.

<b>1. AGENCY USE ONLY (Leave blank)</b>		<b>2. REPORT DATE</b> December 2002	<b>3. REPORT TYPE AND DATES COVERED</b> Technical Memorandum	
<b>4. TITLE AND SUBTITLE</b> A Study of Dynamic Stall Vortex Development Using Two-Dimensional Data from the AFDD Oscillating Wing Experiment			<b>5. FUNDING NUMBERS</b>  712-10-12	
<b>6. AUTHOR(S)</b> Myung J. Rhee				
<b>7. PERFORMING ORGANIZATION NAME(S) AND ADDRESS(ES)</b> Ames Research Center, Moffett Field, CA 94035-1000 and Army/NASA Rotorcraft Division, Aeroflightdynamics Directorate (AMRDEC), U.S. Army Aviation and Missile Command, Ames Research Center, Moffett Field, CA 94035			<b>8. PERFORMING ORGANIZATION REPORT NUMBER</b>  A-0208717	
<b>9. SPONSORING/MONITORING AGENCY NAME(S) AND ADDRESS(ES)</b> National Aeronautics and Space Administration, Washington, DC 20546-0001 and U.S. Army Aviation and Missile Command, Redstone Arsenal, AL 35898-5000			<b>10. SPONSORING/MONITORING AGENCY REPORT NUMBER</b>  NASA/TM-2002-211857	
<b>11. SUPPLEMENTARY NOTES</b> Point of Contact: Mjung J. Rhee, Army/NASA Rotorcraft Division, Aeroflightdynamics Directorate, U.S. Army Aviation and Missile Command, Ames Research Center, MS 215-1, Moffett Field, CA 94035-1000 (650) 604-3646 mrhee@mail.arc.nasa.gov				
<b>12a. DISTRIBUTION/AVAILABILITY STATEMENT</b>  Unclassified — Unlimited Subject Category 02                      Distribution: Nonstandard Availability: NASA CASI (301) 621-0390			<b>12b. DISTRIBUTION CODE</b>	
<b>13. ABSTRACT (Maximum 200 words)</b>  The purpose of this study is to examine the previously unpublished instantaneous pressure data of the Aeroflightdynamics Directorate Two-Dimensional (2D) and Three-Dimensional (3D) Oscillating Wing Experiment to better understand the process of dynamic stall vortex development on the NACA 0015 airfoil. This report presents representative 2D instantaneous pressure data for the upper and lower surfaces of the airfoil at various chordwise locations obtained at specific angles of attack during upstroke and downstroke cycles. Furthermore, the report contains a complete set of plots of instantaneous pressure distributions for the upper surface for all the 2D data sets obtained in the experiment. First, the lift, drag and pitching moment data of various testing conditions are reviewed and analyzed to classify the data both with and without a boundary layer trip into "no stall," "moderate stall," and "deep stall" data. Next, instantaneous pressure distributions on the upper surface of the airfoil are examined for the study of vortex development. The lift and pitching moment data are analyzed to document the dynamic overshoot which delays the development of the stall on the airfoil. Next, the range of angles of attack are selected where the lift and pitching moment data shows significant changes from unsteady flow behavior during oscillation cycles. Furthermore, based on the unsteady flow characteristics found in each classification of dynamic stall, analysis is continued to identify the conditions where the reduced frequency clearly affects the unsteady flow behavior of the airfoil during the oscillation. This can result in a change of the dynamic stall classification of the airfoil response under various unsteady flow conditions. These conditions are discussed in detail in the comparative studies.				
<b>14. SUBJECT TERMS</b> 2D Oscillating airfoil, NACA 0015, Dynamic stall vortex development, Instantaneous pressure distributions, Unsteady flow characteristics			<b>15. NUMBER OF PAGES</b> 96	
			<b>16. PRICE CODE</b>	
<b>17. SECURITY CLASSIFICATION OF REPORT</b> Unclassified	<b>18. SECURITY CLASSIFICATION OF THIS PAGE</b> Unclassified	<b>19. SECURITY CLASSIFICATION OF ABSTRACT</b> Unclassified	<b>20. LIMITATION OF ABSTRACT</b>	